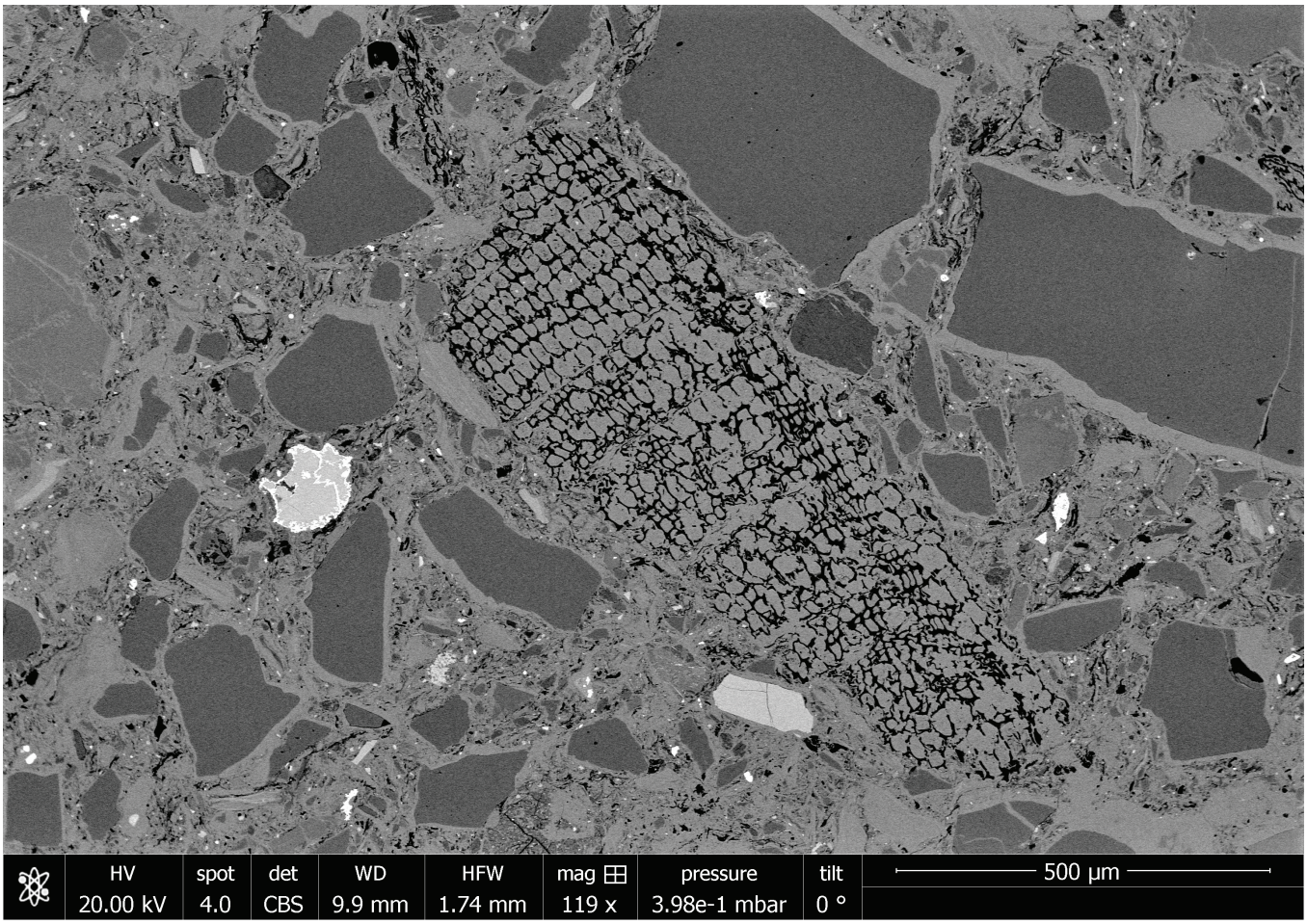
Stockholm University

Master Thesis

Degree Project in Geology 60 hp

Impactites from the Hiawatha crater, North-West Greenland

Jacob Gustafsson



Stockholm 2020

Department of Geological Sciences
Stockholm University
SE-106 91 Stockholm

Abstract

The recent discovery of the 31-km-wide Hiawatha impact crater has raised unanswered questions about its age, impactor and highly unusual organic carbon component. Previous research suggests a fractionated iron meteorite impactor, a probable maximum 3–2.4 Ma impact age and a possible Younger Dryas impact age. The first objective in this study has been to investigate a possible link between the Cape York meteorites and the Hiawatha impact crater by comparing the chromium isotopic signature in chromite from a Cape York meteorite with the chromium isotopic signature in potential chromite from the Hiawatha impactor. The second objective has been to investigate a possible Hiawatha signature in the Younger Dryas deposits from Baffin Bay. The third objective has been to study the organic carbon component in impactites derived from the Hiawatha impact crater.

Heavy mineral grains were separated from glaciofluvial sediment which contains Hiawatha impactite grains. Not a single chromite grain was found and the possible link to the Cape York meteorites could not be tested. The petrographic examination of Younger Dryas marine deposits resulted in absence of impact-related Hiawatha grains. A petrological investigation revealed that organic carbon was likely found in five of six variably shocked impactites derived from the Hiawatha impact crater. The character of the organic carbon varies between the samples and also within individual samples. Vitrinite reflectance measurements of the organic carbon in two impactites yielded low reflectance values compared to charcoalification experiments of wood. Organic particles with different reflectance in the same sample suggest that the particles had different impact histories prior to settling and becoming a rock. Diagnostic conifer cellular texture was found in at least one of the samples. The character of the organic particles in the impactites supports the suggestion in a previous study that the sources of the Hiawatha organic carbon component are unmetamorphosed surficial deposits containing dead conifer tree trunks and fine-grained layered clay and organic matter.

In this study it is concluded that the apparent absence of chromite in the examined glaciofluvial sediment sample corroborates the significance of previous research which suggests that the Hiawatha impactor was an iron meteorite. The apparent absence of impact related grains in the Younger Dryas deposits suggests that although a Younger Dryas age for the Hiawatha impact crater is less likely now, the possibility remains open. The organic carbon with diagnostic conifer cellular texture in the Hiawatha impactites corroborates the conclusion in a previous study that the Hiawatha impact-related organic carbon component stems from local, thermally degraded conifer trees with a probable age of ca. 3–2.4 Ma. It is also concluded that the relatively low reflectance values of the organic carbon in the Hiawatha impactites seem to be related to the short duration of the high-temperature excursion during the hypervelocity impact event.

Abbreviations in microphotographs

BSE = Backscattered electron
EPI = Epi-illumination (reflected light)
PPL =Plane polarized light
XPL = Crossed polarized light
UV = Ultra violet

Table of Contents

1. Introduction **1**
2. Geological background **3**
2.1 Impact structures in Greenland 3
2.2 Sample locations 3
2.3 The Cape York meteorites 5
2.4 Marine sediment from site 012 5
2.4.1 Core description and sediment age 5
2.4.2 Sediment lithology 6
3. Theoretical background **8**
3.1 Meteorite identification by Cr isotopes 8
3.2 Impactite formation 8
3.3 Types of impactites 9
3.4 Organic matter in impactites 10
4. Methods **11**
4.1 Heavy mineral identification 11
4.1.1 Wilfley table gravity separation 11
4.1.2 Frantz magnetic separation and heavy liquid separation 11
4.1.3 Hand picking, magnetic separation and mounting 11
4.1.4 Automated Quantitative Mineralogy 12
4.2 Marine sediment identification 12
4.2.1 Thin section preparation 12
4.2.2 Optical mineral identification 13
4.3 Carbon petrology 13
4.3.1 Thin section preparation 13
4.3.2 Petrographic microscopy 14
4.3.3 Scanning Electron Microscope - Energy Dispersive Spectroscopy 14
4.3.4 Vitrinite reflectance 14
5. Results **15**
5.1 Heavy mineral identification 15
5.2 Marine sediment identification 17
5.3 Carbon petrology of HW19 impactites 20
5.3.1 Weakly shocked impactites 22
5.3.2 Moderately shocked impactites 24
5.3.3 Highly shocked impactites 27

6. Discussion **30**
6.1 Heavy mineral identification 30
6.1.1 The apparent absence of chromite in HW21-2016 30
6.2 Marine sediment identification 31
6.2.1 The apparent absence of impactite grains in 012P 31
6.2.2 Ejecta distribution of the Hiawatha impact 31
6.3 Organic matter in Hiawatha impactites 32
6.3.1 Organic carbon variation 32
6.3.2 Reflectance measurements 36
6.3.3 Source of the organic carbon 39
7. Conclusions **41**
Acknowledgements **42**
References **43**
Appendix A. Macroscopic impactite data **47**
Appendix B. Microscopic impactite data **48**

1. Introduction

The newly discovered 31-km wide Hiawatha impact crater (HIC) is highly unusual in many ways. It is one of the 25 largest impact structures on Earth (Kjær et al., 2018; Impact Earth, 2020, https:// impact.uwo.ca/). Even though it is probably the youngest known large impact structure on Earth (Garde et al., 2020), there is yet no proven ejecta layer associated with the HIC. It is the northernmost known impact crater on Earth and covered by the Greenland Ice Sheet (GrIS), which has an anomalous ice stratigraphy right over the crater compared to most of the GrIS (Kjær et al., 2018). The impact crater is located ~183 km from the proposed 36,5 km-wide Paterson crater, which like Hiawatha was discovered recently and is covered by the GrIS (MacGregor et al., 2019). The HIC is located ~300 km from Cape York, around where some of the largest known meteorites on Earth, the Cape York meteorites (CYM), were found. The HIC has a highly unusual organic carbon component (Garde et al., 2020). All these circumstances have raised multiple questions of which the most important regards the age of the HIC.

Kjær et al (2018) reported the discovery of the impact crater and the quartz grains with shock-diagnostic planar deformation features (PDFs), which proved that Hiawatha is an impact crater. These grains were found in the sediment sample HW21-2016, which was deposited at the front of the Hiawatha Glacier just outside the crater rim. The sample contains a large variety of sand-sized impactite grains originating from the crater floor (Kjær et al., 2018). Elevated platinum (Pt) contents and anomalous platinum-group element elements (PGE) ratios in HW21-2016 point to a strongly fractionated Duchesne (type IVA) iron meteorite as the Hiawatha impactor (Kjær et al., 2018). This chemical signature differs slightly from the CYM, which belongs to the less fractioned type IIIAB iron meteorites (Esbensen et al., 1982).

The following paragraph is based in information in (Kjær et al., 2018). Ice-penetrating radar evidence of the stratigraphy of the ice sheet over the HIC shows that the Holocene ice layer (11.7 to 0 ka) is continuous and conformable across the crater, whereas deeper and older ice is debris-rich or heavily disturbed. The debris clearly originates from the crater floor, indicating active subglacial erosion. The lack of distinct last glacial period (LGP; ~115 to 11.7 ka ago) reflections from pre-Younger Dryas (YD; ~12.8 to 11.7 ka ago) ice layers c. 100 km around the HIC indicate that the surrounding ice flow has also been disturbed. Moreover, radargrams of the ice layers shows evidence of subglacial water storage and active basal melting within and beneath the ice, which indicates that the ice is currently responding to a heat source. Based on modern surface velocities (~10 to 30 m year−1) (figure 2D), it would only take a few millennia for deeper ice to flow across the crater, which excludes steady, uninterrupted ice flow from the ice sheet into the crater as a valid explanation for the ice stratigraphy over the crater. Kjær et al (2018) interpreted the anomalous ice stratigraphy to be caused by a transient that strongly affected ice flow there after most of the LGP ice was deposited. Three hypotheses for such a transient were suggested: (i) The retreat of Humboldt Glacier around 9 to 8 ka, which unblocked the Nares Strait, (ii) Water pooling subglacially within the pre-existing crater and a subsequent catastrophic jökulhaup outburst (and possibly repeatedly) through the rim breach of the crater, or (iii) A change in ice flow as a response to the hypervelocity impact that formed the crater – if it occurred when ice was present there. The latter hypothesis suggests that the HIC could have been formed in the YD.

Garde et al (2020) investigated pebble-sized lignite lumps and gravel-sized charcoal particles, collected in the outwash sediments in front of the Hiawatha Glacier, together with carbonaceous impactite grains from sample HW21-2016. It was shown that the lignite lumps

largely consist of *Pinus* or *Picea*, with greatly expanded cork cells and desiccation cracks which indicate rapid, heat-induced expansion and contraction. Vitrinite reflectance (%Ro) of the charcoal pieces (Ro ≤ 3.5%) from sample HW21-2016, indicated impact-induced incineration of surficial and/or originally shallowly buried plant material, whereas the lignite (Ro ~0.2%–0.5%), presumably from the same hypervelocity impact, indicated a distinct heating episode but not direct incineration. Garde et al (2020) described a possible scenario in where the particles with lower Ro values could have been protected by the GrIS with associated permafrost in the target rocks, during the hypervelocity impact. By identifying the wood fragments to genera level, Garde et al (2020) concluded that the age of the modified carbon from the Hiawatha impact is probably 3–2.4 Ma, and thus also the probable maximum age of the impact. This conclusion was based on the fact that conifer trees, such as *Pinus* and *Picea*, are presently extinct from North Greenland, but known from late Pliocene deposits in the Canadian Arctic Archipelago (Fyles et al., 1991) and early Pleistocene deposits at Kap København (figure 2A) (Funder et al., 2001) in eastern North Greenland.

Even though the first firm evidence, in the form of thermally degraded conifer trees, provided of a probable maximum age (ca. 3-2.4 Ma) of the HIC, it is yet undated. It is also unknown what caused the anomalous ice stratigraphy over the crater. One of the previously described possible interpretations in Kjær et al (2018) implies that the HIC could be as young as the beginning of the YD. The evidence for an iron meteorite impactor for the Hiawatha impact, together with the close proximity to the finding places of the CYM, suggest a possible connection to the CYM. In order to address these research questions, 40 glacially transported pebbles and boulders (sample ID prefix = HW19) were collected at the ice margin adjacent to the HIC in the summer of 2019. A preliminary petrographic examination of the HW19 samples revealed that the majority of these samples are impactites and a high proportion of these impactites contain definite or suspected organic carbon.

There are three objectives in this thesis. The first objective is to investigate the possible link between the CYM and the HIC. If the CYM are related to the Hiawatha impact and if the terrestrial age of the CYM can be determined, we would have an indirect age determination for the HIC. Integrated with this investigation a new line of research is trying to absolute date the atmospheric entry of the CYM swarm. The second objective is to investigate if the HIC can be identified in YD deposits from Baffin Bay. If Hiawatha-related grains can be found in YD deposits, we would have an indirect age determination for the HIC. The third objective is to contribute to an ongoing assessment of the origin and nature of the highly unusual carbon component in the HIC. By investigating the organic carbon component in the HIC, we can get a better understanding of how organic matter behaves during a hypervelocity impact. The specific objectives in this thesis are the following:

- Find chromite in the glaciofluvial sand the sample HW21-2016 and compare chromium (Cr) isotope ratios in the chromite with Cr isotope ratios in chromite from the CYM.
- Search for ejecta and/or other impactite grains in YD deposits from Baffin Bay.
- Identify organic carbon in the HW19 impactites and distinguish it from e.g. iron oxides or hydroxides.
- Measure the reflectance (%Ro) of the organic carbon in the HW19 impactites.

2. Geological background

2.1 Impact structures in Greenland

Greenland, the largest island on Earth, is almost entirely covered by ice. As of today, the HIC is the only confirmed impact crater in Greenland (Impact Earth, 2020, https:// impact.uwo.ca/). For comparison, there are 27 known impact craters located in Australia (figure 1). There are two other proposed impact structures on Greenland. Based upon multiple lines of evidence, Garde et al (2012), proposed that the 100 km scale Maniitsoq structure, in western Greenland, is the remnant of a giant c. 3 Ga hypervelocity impact. Based upon satellite and airborne geophysical data, MacGregor et al (2019), proposed an impact origin for a 36.5-km wide subglacial structure under ~2 km of ice in NW Greenland. The structure has an elevated circular rim as well as elevated central peaks, which could be the remnants of a central uplift. The minimum age of the ice overlying the structure is 79 ka (MacGregor et al., 2019).

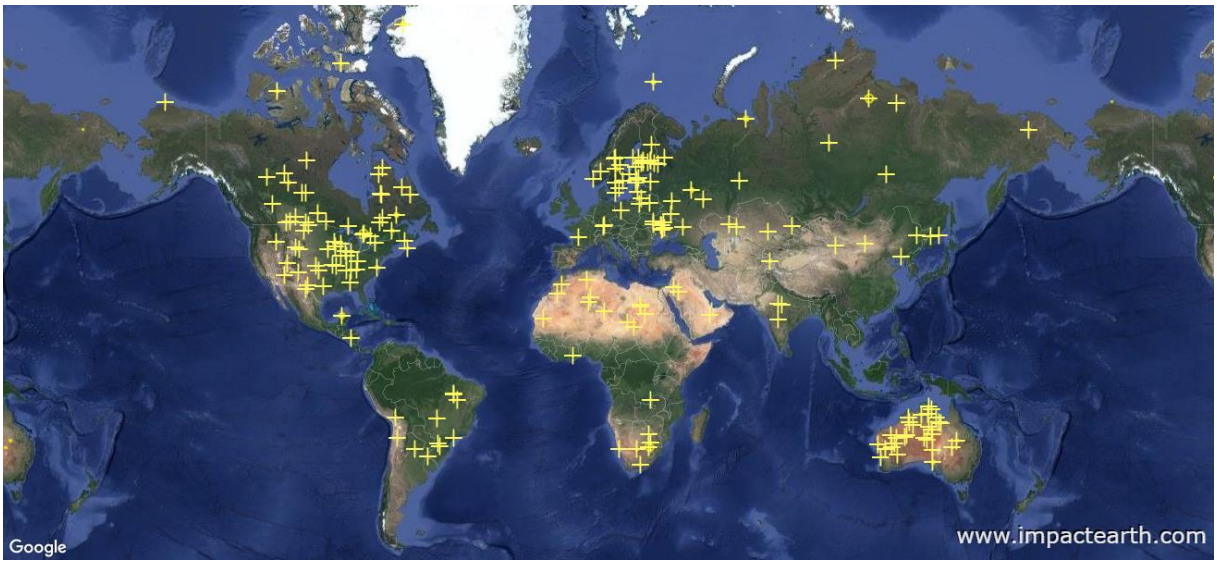


Figure 1. 200 craters are currently plotted on the map as yellow pins (Impact Earth, 2020, https:// impact.uwo.ca/).

2.2 Sample locations

The key localities for the investigated material in this thesis are showed in figure 2A and B. The HIC and the proposed Paterson crater are showed with red circles (figure 2A). The glacially transported pebbles and boulders (HW19) that were investigated in this thesis were sampled at the localities HW19-A, HW19-B and HW19-C (figure 2B). HW19-A is located in the foreland of the Hiawatha Glacier, which is protruding from the GrIS margin which is masking the HIC. HW19-B and HW19-C are located at the curvilinear margin of the GrIS. Figure 2B also shows the sample location of the glaciofluvial sand sample HW21-2016. This sample site is located at the front of the Hiawatha Glacier just outside the crater rim. HW21-2016 was deposited no earlier than the year of 2010 (Kjær et al, 2018). The bulk mineral assemblage and chemical composition of the sand sample HW21-2016 indicate sourcing from local paragneiss (Garde et al., 2020). Based upon erratic boulders of paragneiss deposited by the Hiawatha Glacier, the target rock of the Hiawatha impact is assumed to be comprised of the same paleoproterozoic granulite-grade paragneiss exposed in the ice-free foreland to the crater, Inglefield Land (Kjær et al, 2018). Locally, this bedrock includes sulfidic paragneiss with graphite flakes (Dawes, 2004). In figure 2C, the paragneiss is represented by the pink Precambrian rock unit. Inglefield

Land is part of the E–W-trending Inglefield mobile belt which forms a 1.985 to 1.740 Ga old crystalline shield. (Dawes, 2004). Most of the CYM have been found in the vicinity of the Cape York peninsula and Meteorite Island (figure 2A). The marine sediment that was investigated in this thesis was extracted from site 012 (figure 2A).

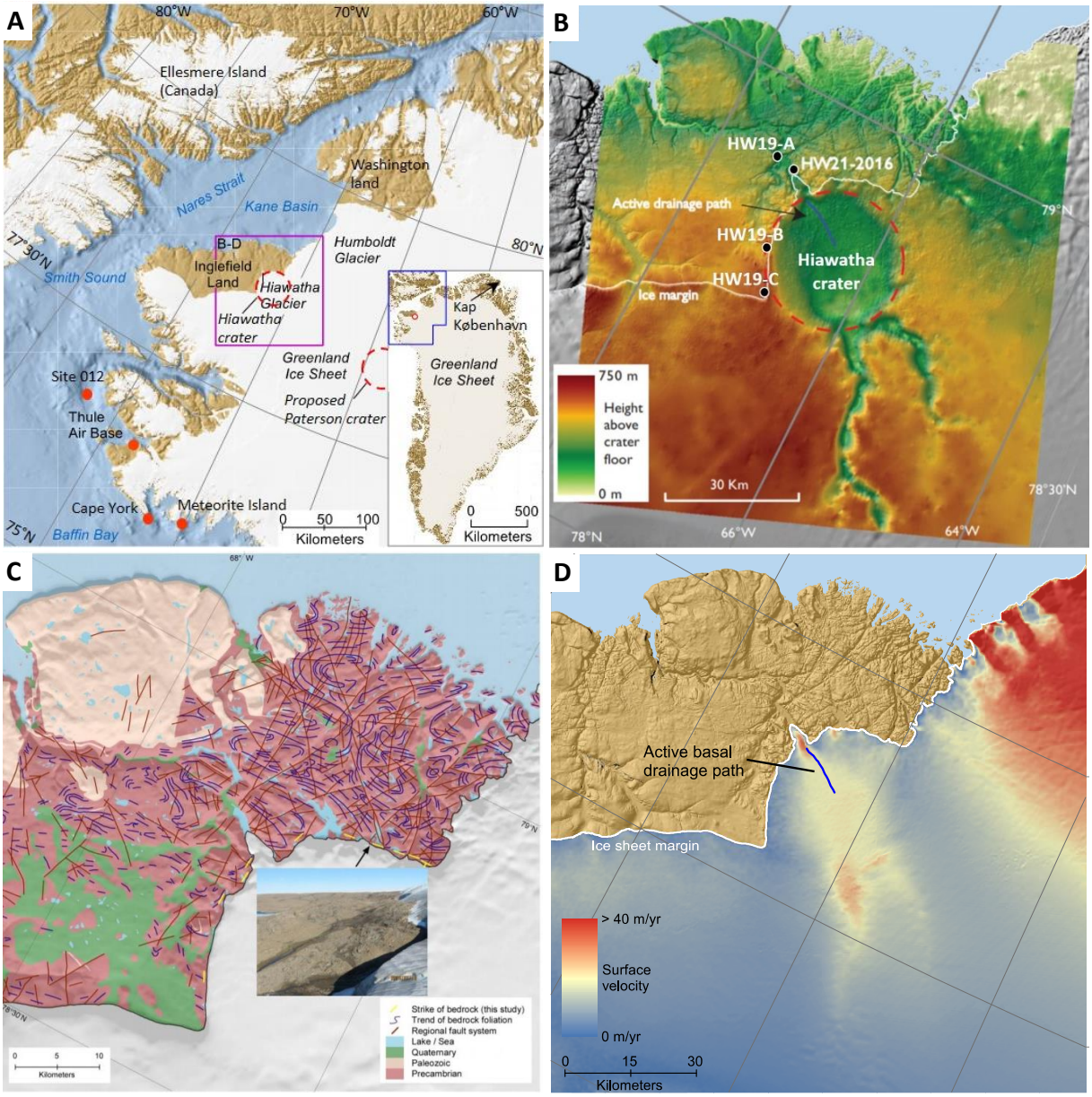


Figure 2. A) Regional view of northwest Greenland. Modified from Kjær et al (2018). **B)** Elevation map of the bedrock showing the circular depression of the crater and sample locations. The ice margin of the GrIS is marked with the white line. Modified from Kjær et al (2018); Garde et al (2020). **C)** Bedrock type and lineations across Inglefield Land adjacent to the crater. The photograph shows a narrow zone along the ice margin where moderately to steeply dipping and commonly brecciated brittle planar structures (yellow lines indicate their locations and their strike) are superimposed on the Palaeoproterozoic bedrock foliation. The structures are tangential to the mostly subglacial rim of the HIC and dips away from it suggesting that they could be the outer, overturned part of the crater rim (Kjær et al (2018). **D)** A 5-m ArcticDEM mosaic over eastern Inglefield Land. The ice surface velocity is colour coded. The blue line illustrates an active basal drainage path inferred from radargrams of the ice From Kjær et al (2018).

2.3 The Cape York meteorites

The CY iron meteorites are fragments from one of the largest known meteorite showers on Earth (Appelt et al., 2015). The meteorites are named after the Cape York peninsula (figure 2A), around where some of the meteorites were found. At least ten specimens of the CYM, ranging from 290 g to 31 tons in weight (Buchwald, 1985), have been discovered (Appelt et al., 2015). The second largest CY meteorite, Agpalililk (20 tons), was discovered in the summer of 1963, by Dr. Vagn Buchwald. The main part (~15 tons) of Agpalilik is presently exhibited at the courtyard of the Geological Museum in Copenhagen. Agpalilik was found on an ice-free slope ~500 m from the shore at an altitude of 75 meters (Buchwald, 1975). Other CYM have also been found relatively close to the shore and at considerable altitudes (table 1). The meteorites have partly been covered with gneiss boulders and without any impact pits (Appelt et al., 2015). Although the CYM are essentially undated, Buchwald (1985) argued that the main body of the CYM probably entered the Earth's atmosphere more than 2 ka, judging from the state of corrosion of the meteorites. Iron meteorites are divided into 13 subgroups based on their chemical composition. The CYM belong to the group IIIAB, which is the largest of 13 subgroups of iron meteorites. IIIAB contains about 300 known meteorites (Haack et al., 2006). Unlike all of the other iron meteorites that are known (Appelt et al., 2015), the CYM are chemically diverse on a meter-scale (Esbensen et al., 1982; 1982a).

Table 1. Data of some of the Cape York meteorites. From Buchwald (1975).

	Date of Find	Reference	Weight kg	Coordinates N – W	Altitude m	Distance to the Sea m	Locality
Ahnighito	1894	Peary 1898	30,880	76°4′–64°58′	24	100	Meteorite Island
Woman	1894	Peary 1898	3,000	76°9′–64°56′	30	500	Saveruluk
Dog	1894	Peary 1898	407	76°9′–64°56′	24	500	Saveruluk
Savik I	1913	Böggild 1927	3,402	76°8′–64°36′	270	1,000	Saveqarfik
Akpohon	1914	Hovey 1918	1.66	79°5′–76°30′	–	–	Ellesmere Land
Northumberland	1928	Buchwald & Munck 1965	0.29	77°20′–72°	–	–	Northumberland Island
Savik II	1961	Buchwald 1963	7.8	76°8′–64°35′	5	10	Saveqarfik
Agpalilik	1963	Buchwald 1963	20,140	76°9′–65°10′	75	500	Agpalilik

2.4 Marine sediment from site 012

2.4.1 Core description and sediment age

In August 1991, three cores were retrieved in a trough close to the Greenland coast (site 012 in figure 2A), at a water depth of 823 m during the CSS'Hudson' cruise 91–039 at 76148.30N, 71151.50W. Site 012 had been identified as a favorable locality on a previous cruise. The sedimentary record from site 012 was subsequently investigated by Knudsen et al (2008) in a multiproxy study of the palaeoceanographic and paleoclimatic changes in northernmost Baffin Bay since the deglaciation of the area at about 12 500 calendar years before present (cal. yr BP). Three cores were retrieved at site 012: the piston core 012P, the trigger weight core 012TWC and the box core 011BC. The sedimentary record from Site 012 were subdivided into eight time-intervals (12-1 to 12-8) based on major changes in environmental parameters (Knudsen et al., 2008). In this thesis, sediment from five different depth intervals from the piston core 012P were investigated: (i) 190-192 cm, (ii) 192-194 cm, (iii) 210-212 cm, (iv) 220-222 cm and (v) 230-232 cm. The ages in cal. yr BP (table 2) for these depth intervals, are based on calibrated accelerator mass spectrometry (AMS) ^{14}C age determinations (Knudsen et al., 2008; see their

tables 3 and 4 for AMS ^{14}C age determinations and an age model, respectively) performed at the Tandem Accelerator Laboratory in Uppsala, Sweden (Knudsen et al., 2008).

Table 2. Sediment intervals with ages in cal. yr BP. From Knudsen et al (2008).

Interval	Core	Top (cm)	Base (cm)	Top (Age, cal. yr BP)	Base (Age, cal. yr BP)
Core site 012					
12-8	011BC/012TWC	0	110	−41	3050
12-7	012TWC	110	151	3050	4790
12-6	012P	16	63	8200	9500
12-5	012P	63	128	9500	10 900
12-4	012P	128	145	10 900	11 300
12-3	012P	145	195	11 300	12 300
12-2	012P	195	205	12 300	12 500
12-1	012P	205	240	12 500	?

2.4.2 Sediment lithology

Deglaciation of the area took place at about 12 500 cal. Yr BP, but the maximum expansion of the Weichselian ice south of Smith Sound (figure 2A) is unknown (Knudsen et al., 2008). The diamicton in the bottom of core 012P (figure 3) is assumed to be of late LGP age, although a Saalian or an even older age has been discussed (Kelly et al., 1999).

Interval 12-1

The sediment in interval 12-1 (205-240 cm) is comprised of a diamicton (Knudsen et al., 2008). Blake et al (1996), suggested that the site was glaciated and that the sediments were deposited by glacial processes as a till. According to England et al (2006), the Nares Strait was filled by glaciers during the late LGP, and the basal diamicton at Site 012 might have been deposited during the deglaciation of the late LGP.

Interval 12-2

The sediment in interval 12-2 is comprised of laminated clay and silty clay without any microfossils and a negligible amount of organic carbon, probably indicating turbid waters and seasonally variable sedimentation from meltwater plumes during deglaciation (Knudsen et al., 2008)

Interval 12-3

The sediment in interval 12-3 is comprised of extremely fine laminated clay and silt-sized sediment in the lowermost laminated part of the interval. Foraminiferal assemblages appear within the laminated sediments at c. 12 300 cal. yr BP (Knudsen et al., 2008)

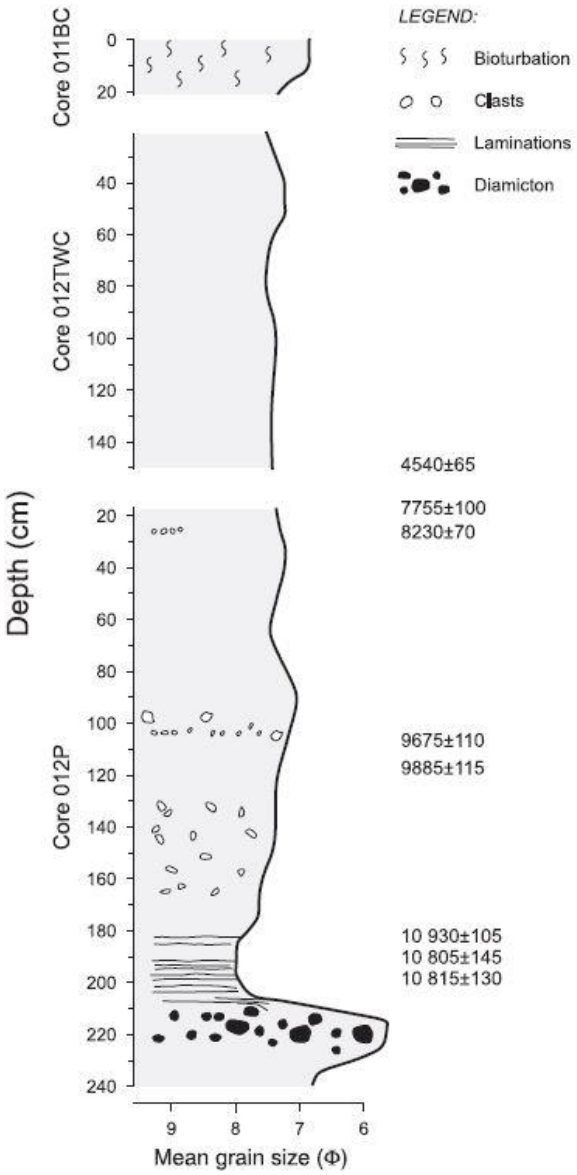


Figure 3. Lithological log and ^{14}C age determinations for the studied intervals of cores 012P, 012 TWC and 011BC (Site 012). The vertical scale shows actual core barrel depths. The column width is based on smoothed mean grain size with increasing grain size towards the right. From Knudsen et al (2008).

3. Theoretical background

3.1 Meteorite identification by Cr isotopes

Cr isotopes can be used to identify the meteorite type for an impact event (Koeberl et al., 2007). First, the $^{53}Cr/^{52}Cr$ ratio is measured in the rock sample. The ^{53}Cr value is the daughter product of the extinct radionuclide ^{53}Mn (half-life = 3.7 Ma; Lugmair and Shukolyukov, 1998). Secondly, the relative abundance of ^{53}Cr is measured as the deviation of the $^{53}Cr/^{52}Cr$ ratio in a sample relative to the standard terrestrial $^{53}Cr/^{52}Cr$ ratio (Koeberl et al., 2007). Such measurements are performed by high-precision thermal ionization mass spectrometry (TIMS) (Lugmair and Shukolyukov, 1998). All terrestrial ^{53}Mn was derived from the primordial solar nebula (Koeberl et al., 2007). Since the homogenization of the Earth was completed after all ^{53}Mn on the planet had decayed, terrestrial rocks are not expected to show any variation in the $^{53}Cr/^{52}Cr$ ratio. Most meteorite groups show a variable excess of ^{53}Cr relative to terrestrial samples (Koeberl et al., 2007).

3.2 Impactite formation

French (1998), defined impactites as, “all rocks affected by, or produced by, the shock waves and other processes generated by hypervelocity meteorite impact events” (p. 61). The pressures and associated shock metamorphism for a hypervelocity impact event are far beyond the range for normal geological processes (figure 4) (Stöffler et al., 2018). Under such extreme conditions shock waves will produce characteristic shock effects in minerals, such as mechanical deformation, phase transformation, decomposition and melting (Stöffler et al., 2018). The shock waves travel several km/s through rocks and affect their minerals with high and transient pressures, which results in shock-deformation effects of high stress, high strain rates (French, 1998). Along with the shock waves, energy is deposited in the minerals and therefore a particular shock pressure will generate a specific postshock temperature (figure 4). The postshock temperatures does not only increase along with pressure, but is also highly dependent on the target material. If the pressure and associated temperatures are high enough melting and vaporization can occur. What types of impactites are formed also depends on the target lithology, stratigraphy and the nature of the impactor and its impact angle (French, 1998). According to Stöffler et al (2018), the formation of impactites depends on the following conditions:

1. The size and gravity of the target
2. The relative impact velocities of the impactor and target
3. The relative sizes of the impactor and target
4. The possible presence of an atmosphere and water on the target
5. The physical properties of the impactor and target (e.g., their density and porosity)

A given impactor velocity will generate a variety of peak shock pressures and temperatures, depending on the porosity and shock impedance of a target. Shock impedance is defined as the product of shock wave velocity and the density of the mineral (Stöffler et al., 2018). Mechanical impedance determines how a shock wave reflects when it hits a boundary between materials with different densities and wave speeds (Ormö et al., 2013). At a given shock pressure, the shock temperature of highly porous rocks can be up to an order of magnitude higher (figure 4) than those of dense crystalline rocks (Stöffler et al., 2018). Compared to crystalline rocks, porous rocks have a higher capability to absorb the shock wave energy by the numerous grain

interfaces and pore spaces (French, 1998). No consensus has been reached so far, with respect to the onset or nature of specific shock effects in carbonate target rock (Stöffler et al., 2018).

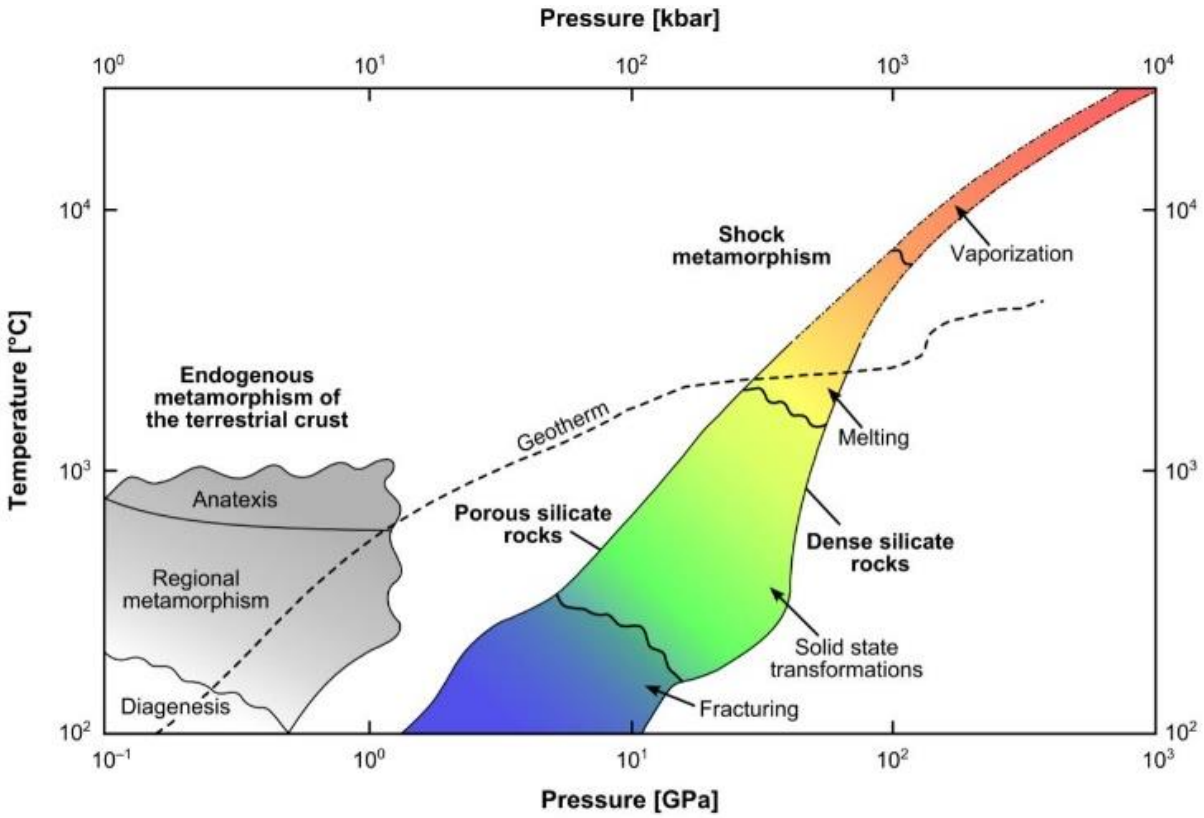


Figure 4. Pressure–temperature fields for shock metamorphism of silicate rocks in comparison with endogenous metamorphism of the terrestrial crust. From Stöffler et al (2018).

3.3 Types of impactites

The following section is based upon French (1998). A variety of impactites are formed during an impact event. The sketch in figure 5 shows the basic distinction of impactites. Parautochthonous rocks are beneath the crater floor and the allochthonous rocks are either crater-fill rocks or ejecta which is deposited outside of the crater. The parautochthonous rocks are subjected to relatively low shock pressures. Shock pressures for parautochthonous rocks may be up to 25-30 GPa in the center of the impact structure and may be less than 2 GPa at the rim. The shock pressures also decrease with depth and hence most of the parautochtonous rocks are subjected to less than 2 GPa. The shock effects for these impactites are mostly fracturing, brecciation and the formation of shatter cones. The allochtonous rocks comprises both the rocks that fill the crater after its excavation and also ejected material beyond the crater rim. These rocks are mainly subjected to relatively high shock pressures. The allochtonous rocks that fill the crater are called crater-fill breccias and are generally a complex mixture of impact melts, highly shocked, excavated and reposited rocks and also unshocked rocks from the crater rim and walls. Excavated rocks may be subjected to relatively high shock pressures of about 5 GPa to >100 GPa. More than 90% of the ejected material beyond the crater rim is deposited within five crater radii. This material is called proximal ejecta. Material that has been ejected beyond five crater radii is called distal ejecta. Distal ejecta tends to display a high level of shock effects. Smaller ejecta particles (typically ≤1 mm) can be distributed by atmospheric transport to

regional or global distances. Ejecta deposits may contain shocked rock and mineral fragments, distinctive chemical and isotopic signatures and glassy objects such as tektites (French, 1998).

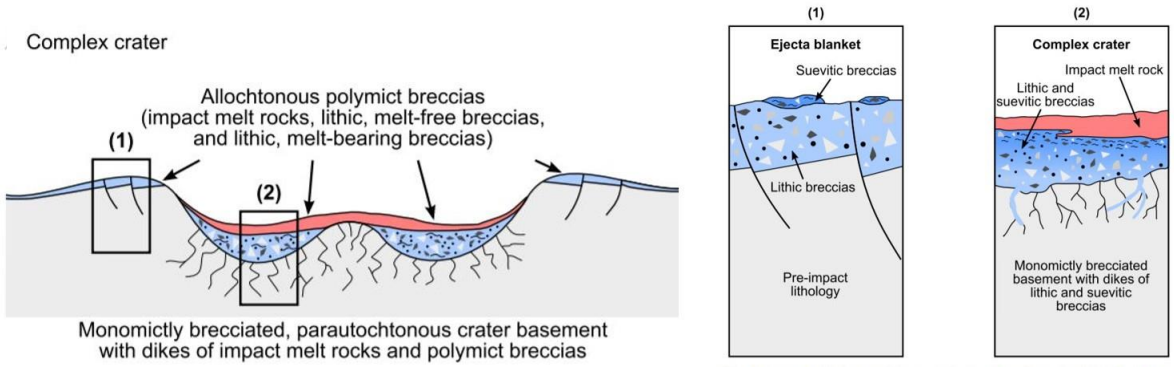


Figure 5. Cross section of a complex crater and the typical locations for proximal impactites. A complex crater is characterized by a centrally uplifted region, a generally flat floor and extensive inward collapse around the rim (French, 1998). On Earth, the transition between smaller bowl-shaped simple craters and complex craters occurs at a diameter of about 4 km in massive crystalline rocks and at about 2 km in sediments (French, 1998). Lithic breccias are melt-free impact breccias. Suevitic breccias are melt-bearing impact breccias Stöffler et al (2018). Modified from Stöffler et al (2018).

3.4 Organic matter in impactites

Organic matter is an uncommon component in impact structures and occurs as recycled carbon from target rocks (Garde et al., 2020). Organic carbon in ejecta derived from sedimentary target rocks, has been investigated from the ca. 23 Ma Haughton crater in Canada (Parnell et al., 2007), as well as from the ca. 15 Ma Ries crater in Germany (Osinski, 2003). Charcoal particles in a drill core from the 66 Ma Chicxulub crater in Mexico, were investigated by Gulick et al (2019).

In some studies, the source of the carbon has been identified and used to constrain the maximum age of the impacts. Gilmour et al (2003) and Parnell and Lindgren (2006), argued that dispersed graphitic carbon in the ca. 500 Ma Gardnos crater in Norway stems from Cambrian Alum Shale. Howard et al (2013) described preserved biomarkers from vegetation in impact glasses, which were linked to the proposed ca. 0.8 Ma Darwin crater, Tasmania. Losiak et al (2016) investigated locally derived charcoal in the small ca. 3.2 ka Kaali craters, Estonia. As previously described, Garde et al (2020) investigated thermally degraded organic material which yielded a probable maximum age for the Hiawatha impact of ca. 2.4-3 Ma.

Organic matter has also been found in impact glass unlinked to any known impact craters. Shultz et al (2014), investigated plant matter encapsulated within impact glasses found in different layers of the Pampean strata of Argentina. The impact glasses were produced by separate bolide impacts into the loessoid sediments between 9.2 Ma and 6 ka (Shultz et al., 2014). Moore et al (2020), described a 12.8 ka YD boundary layer at Abu Hureyra in Syria, which contains melt glass most likely from an airburst event, possibly accompanied by ground impacts by fragments of an impactor. Approximately 40% of the melt glass contains carbon-infused, siliceous plant imprints formed at a minimum of 1200°–1300°C (Moore et al., 2020).

4. Methods

4.1 Heavy mineral identification

4.1.1 Wilfley table gravity separation

Heavy mineral grains from the sand-sized (<600µm) glaciofluvial sample HW21-2016, were concentrated through a Wilfley table (Holman-Wilfley Ltd) gravity separation. Prior to the gravity separations the weight of HW21-2016 was 295 grams. The front tilt of the Wilfley table (figure 6A) was set to 7.5 degrees and the side tilt of the table to 1.6 degrees. The heaviest mineral grains in both sand samples were concentrated into three different fractions, which are called the “head”, the “tail” and the “extra tail”. Figure 6B shows the heaviest mineral grains remaining towards the end of the gravity separation. Finally, all sand that is left on the table is a thin line with the heaviest mineral grains from the uppermost groove. The lowermost half of this thin line is the tail fraction and the uppermost half is the “head" fraction.

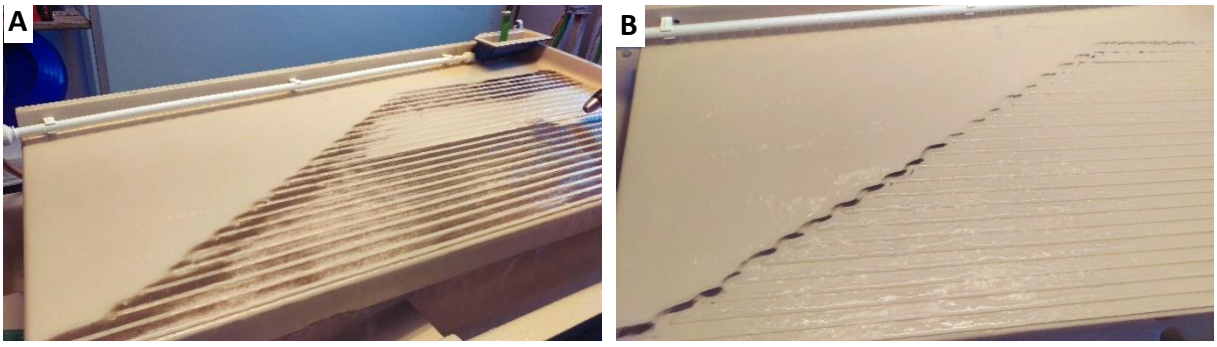


Figure 6. **A)** Wilfley table separation of one of the sand samples. The table is tilted in two directions **B)** Only the heaviest sand is left towards the end of the Wilfley table separation.

4.1.2 Frantz magnetic separation and heavy liquid separation

Another subsample of HW21-2016 was separated with a Frantz isodynamic magnetic separator and with heavy liquids by Geotrack International Ltd in Australia. The heavy liquid separation was conducted at the separation specific gravities (SG) of 2.95 and 3.3. The subsample of HW21-2016 was separated into four fractions:

1) Vertical Frantz magnetics – grains removed before the heavy liquid separation
2) Horizontal Frantz magnetics – magnetic grains removed from the >2.95 SG heavy mineral fraction
3) Apatite fraction – non magnetic 2.95 – 3.3 SG grains
4) Zircon fraction – non magnetic > 3.3 SG grains

4.1.3 Hand picking, magnetic separation and mounting

Three separates, the HW21-2016 “head” fraction, the HW21-2016 horizontal Frantz magnetics and the HW21-2016 zircon fraction, were selected for identification and placed in petri dishes filled with ethanol. In the HW21-2016 “head” fraction and the HW21-2016 horizontal Frantz magnetics, ferromagnetic grains were separated from weaker magnetic grains by a handheld magnet and a stronger neodymium magnet (figure 7A). In addition, grains were placed along the edge of a medium-sized petri dish which was moved around in a circular motion, so that the heavier grains were concentrated closer to the edge of the petri dish. A total of 123 grains were handpicked from the petri dishes with tweezers and pipettes under a stereomicroscope (Wild Heerbrugg). The selection was mainly based on the color, luster and shape of the grains. Finally, the selected grains were mounted on epoxy glue, which together with epoxy resin and a hardener were made into a grain mount (figure 7B). In preparation for the subsequent micro-

analysis with Automated Quantitative Mineralogy (AQM), the grain mount was polished with sand papers. The grains were placed with their flattest surface on top of the epoxy glue to minimize the mass loss by polishing.

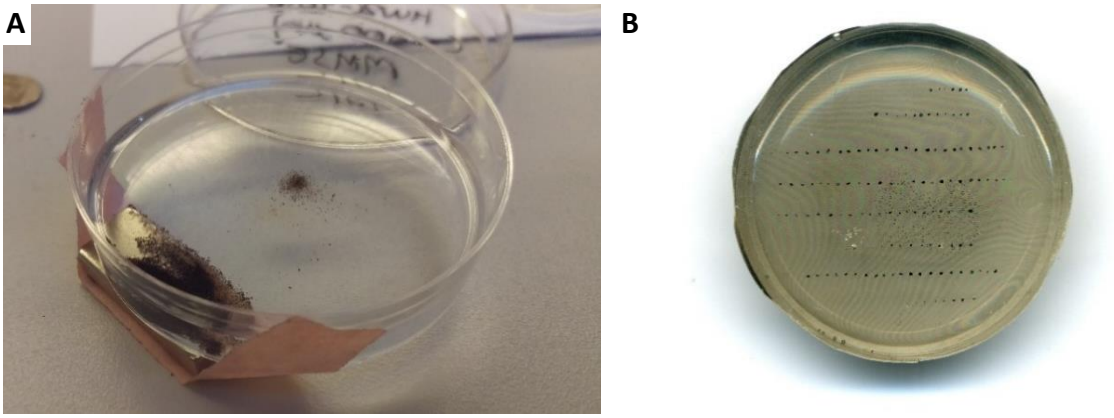


Figure 7. A) Magnetic grains separated from nonmagnetic grains with a neodymium magnet. **B)** The final polished grain mount with 123 grains in eight rows.

4.1.4 Automated Quantitative Mineralogy

AQM is an integrated system with an energy dispersive spectrometry (EDX) detector mounted to a SEM integrated with software. The AQM system was developed in the 1980s to analyze the mineralogy, chemistry, and microstructures of mineral ores, fly ashes, and sediments (Keulen et al, 2020). The previously described polished grain mount was carbon coated and analyzed by AQM at the Geological Survey of Denmark and Greenland's (GEUS) in Copenhagen. This AQM system includes a ZEISS SIGMA 300VP SEM equipped with a BSE detector and two Bruker XFlash 6j30 EDX detectors, with 129 eV energy resolution and with the ZEISS Mineralogic automated quantitative mineralogy software platform. The ZEISS Mineralogic software has integrated matrix corrections and full quantification of energy dispersive spectrometry data and is therefore able to give detailed chemical information on each pixel in the AQM mineral maps (Keulen et al, 2020). In this study AQM was applied for mineral maps and BSE images of the grains in the grain mount.

4.2 Marine sediment identification

4.2.1 Thin section preparation

The mineral identification was performed on lithogenous marine sediment from the marine piston core 91-039-012P. A total of 389 sand grains (figure 8A) were handpicked with a tweezer under a stereomicroscope of the model Olympus SZ40. The grains were sorted into sub-groups based upon their core depth. Impactite grains from the sample HW19 AB3 2019, which was collected in the foreland of the Hiawatha Glacier, were used as reference grains. Figure 8B shows some of the grains during the manufacturing of one of three grains mounts.

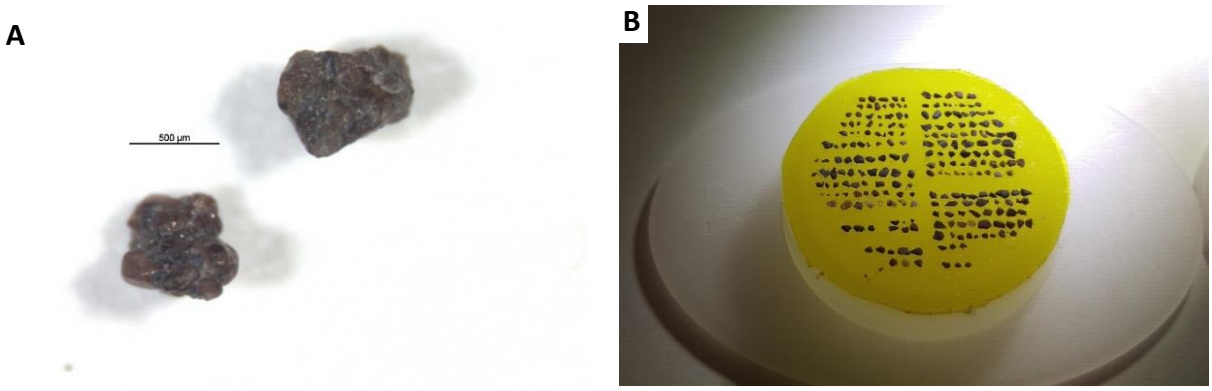


Figure 8. A). Two of the 389 selected sand grains. **B)** Marine grains placed on top of yellow glue.

4.2.2 Optical mineral identification

The three grain mounts were sent to Precision Petrographics Ltd. in Canada, where three polished thin sections (figure 9) were made. The thin sections were examined with petrographic microscopes (Leica DMLP and Leica LEITZ DMRXP) with reflected and transmitted light illumination. Both plane polarized and crossed polarized light were used. Some of the grains were analyzed in the same SEM-EDS session as the previously described HW19-thin sections.

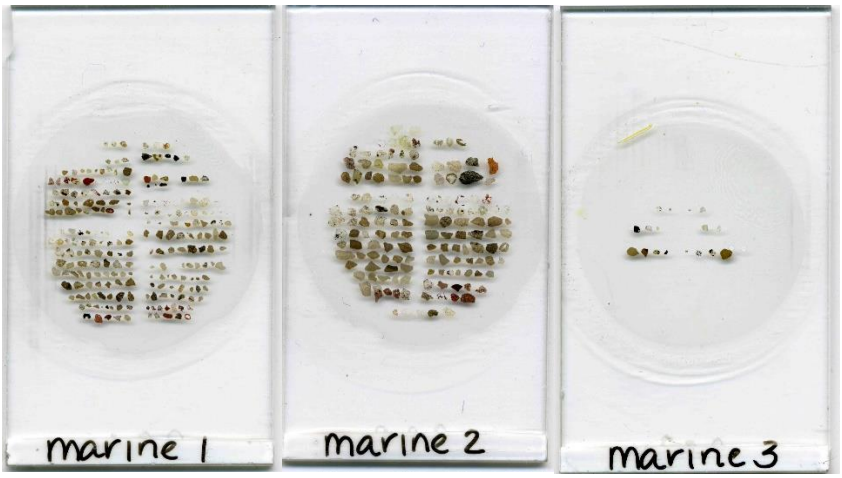


Figure 9. Three polished thin sections with the selected grains from the marine piston core 91-039-012P.

4.3 Carbon petrology

4.3.1 Thin section preparation

A total of 72 rock chips were cut from the 40 previously described rock HW19-samples (sampling locations in figure 2B) at the University of Copenhagen as the first step of thin section preparation. In figures 10A and B, rock samples HW19-39 and HW19-32 are shown. The rock chips were subsequently sent to Precision Petrographics Ltd, Canada, where 72 thin sections were manufactured. The thin sections were polished in order to allow observations in reflected light and non-destructive scanning electron microscope imaging and chemical analysis. 15 thin sections from as many rock chips (appendix A1) were selected for this study.

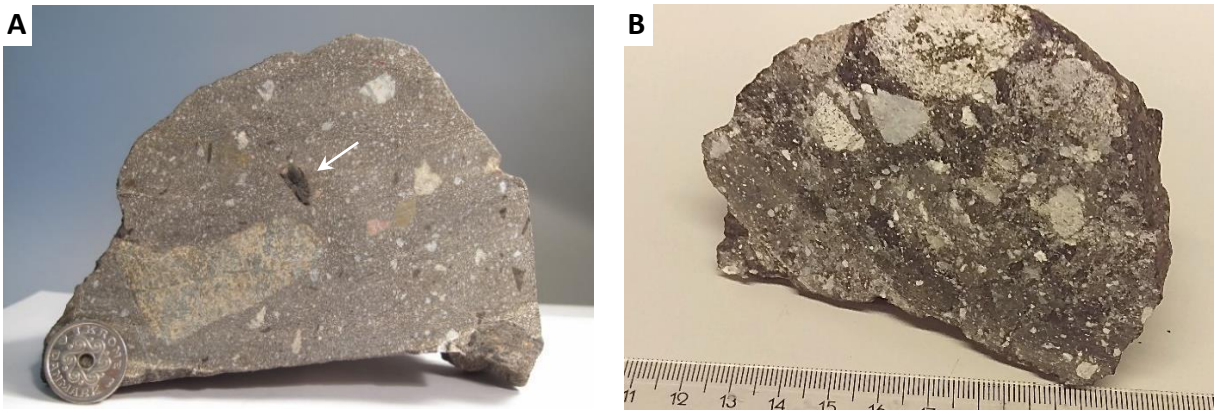


Figure 10. **A)** Cross section of sample HW19-39. Arrow shows black piece of organic carbon. The diameter of coin is 2.25 cm. **B**) Cross section of sample HW19-32. Ruler (cm) for scale.

4.3.2 Petrographic microscopy

The thin sections were studied by petrographic microscopy, which was the main tool for mineral identification and establishing textural relationships. The main petrographic microscopes used in this study were a Leica DMLP and a Leica LEITZ DMRXP. The samples were examined in reflected and transmitted light. Both plane polarized and crossed polarized light were used. Out of the 15 thin sections, six were selected for further analyses with scanning electron microscopy and vitrinite reflectance.

4.3.3 Scanning Electron Microscope - Energy Dispersive Spectroscopy

Six thin sections were analyzed with a FEI Quanta 650 FEG Scanning Electron Microscope (SEM) at the Swedish Museum of Natural History in Stockholm, Sweden. The SEM was equipped with Energy-Dispersive Spectroscopy (EDS), which was used in order to obtain element concentrations from a point or the average from an area of the thin sections. Two different EDS detectors were used – an Oxford $Xmax^N$ 80mm^2 SDD and an Oxford X $Xmax^N$ 50mm^2 SDD. The accelerating voltage of the electron beam was set to 20 kV at a working distance of 10 mm. The SEM was operated in low vacuum mode (40 pascal), in where a micro atmosphere of water vapor functions as an electrically conductive medium, instead of using a traditional coating of carbon or gold. Copper tape or graphite tape were attached to the edges of the thin sections for enhanced conductivity. Carbon coating was avoided because carbon was an analytical target. Backscattered electron (BSE) imaging was used to reveal microstructures and mineral textures at both low and high magnification. The BSE detector shows the variations in mean atomic weight of the sample surface. The software AZtec (Oxford Instruments) was used for data reduction. Scanned close-ups of the thin sections were printed out in grayscale on A4 paper sheets and used as orientation maps during the SEM-EDS sessions.

4.3.4 Vitrinite reflectance

Six thin sections were analyzed quantitively with vitrinite reflectance (VR) at the Lithospheric Organic Carbon Laboratory (L.O.C.) laboratory in Aarhus University, Denmark. VR data is typically presented in units of reflectance (%Ro), which is the measured percentage of reflected light from a sample immersed in oil (Burnham and Sweeney, 1989). In this study, carbon petrology was carried out using a Zeiss Imager M2m AXIO microscope, which was equipped with 50x oil immersion and 63x water immersion objectives and the Diskus-Fossil program (Hilgers Technisches Buero,Konigswinter, Germany). Random reflectance measurements (%Ro) were conducted under oil immersion using the ×50 objective on assumed carbonaceous matter in incident white light and the microscope system was calibrated against a KB N-LASF 1.32%Ro standard.

5. Results

5.1 Heavy mineral identification

Out of the 123 grains from the HW21-2016 sample that were identified by AQM, six grains were from the Wilfley table separated heavy mineral "head" fraction, 11 grains were from the horizontal Franz magnetic fraction (>2.95 SG) and 106 grains were from the non-magnetic zircon fraction (> 3.3 SG). Not as single grain was identified as chromite. In table 3, the bulk mineral assemblage and chemical composition are shown for all grains from the "head" fraction (row 1), for all grains from the horizontal Franz magnetic fraction (row 2) and for 26 grains from the zircon fraction (row 3).

The mineral map in figure 11 and the raw data for row1 in table 3, reveal that ilmenite and Fe-oxide are the main mineral components of the grains in the "head" fraction. Most of these grains also have a minor rutile component. The grains are dark-coloured, opaque and have a dull or submetallic luster. The shapes of these grains are mainly equant. The two grains with a high proportion of iron oxide are more tabular (figure 11).

In table 3, the 11 grains in row 2 are from the horizontal Franz magnetic fraction. The main mineral component in eight of the grains is ilmenite. These grains also have minor proportions of iron oxide and rutile. The main mineral component in the three remaining grains is iron oxide, pyroxene and rutile, respectively. The grains in row 2 are dark-coloured, opaque and have a dull or submetallic luster. The shapes of these grains are either equant, tabular or irregular.

The main mineral component in the remaining 106 grains is rutile. The raw data for the 26 grains in row 3 (table 3) is also representative for the remaining grains from the non-magnetic zircon fraction. Mineral maps and raw data revealed that these grains have a relatively high proportion of an unclassified mineral component. This is also the case for the rest of the grains from the zircon fraction. The AQM data showed that this unclassified component has a relatively high proportion of element vanadium (between 3.32 to 4.05%). For instance, the proportion of vanadium in the unclassified component of the grains in row 3, is 4,05% (table 3). The majority of the selected grains from the zircon fraction are dark-coloured and opaque under a stereomicroscope. A minor proportion of the grains are dark brown-coloured and slightly translucent. The selected grains from the zircon fraction can be divided into two groups with respect to luster. One group has a duller luster and the other group has a more adamantine to submetallic luster. The most common grain shapes are equant or tabular.

Table 3. AQM data for three of the eight rows of grains in the grain mount (figure 7B) with selected grains from the HW21-2016 sample. Row 1 data are from the "head" fraction. Row 2 data are from the horizontal Franz magnetic fraction. Row 3 data are from the zircon fraction.

Row	Mineral	Area %	Weight %	Average Composition %
Row 1	Ilmenite	53,46	81,60	Fe 39,32; Ti 36,84; O 23,84;
	Titanite	0,27	0,30	O 34,22; Ti 28,46; Ca 23,32; Si 14;
	Rutile	4,26	6,09	Ti 62,43; O 37,57;
	Biotite	0,01	0,01	O 33,19; Fe 29,15; Si 19,94; Al 10,2; K 7,52;
	Fe-Oxide	37,74	12,00	Fe 64,21; O 23,2; Ti 12,47; Si 0,11; S 0;
	Unclassified	4,27	-	Ti 37,27; O 30,26; Fe 20,1; Ca 5,41; Si 4,11; V 1,23; Al 0,92; Mg 0,6; Na 0,05; Pb 0,02; As 0,01;
Row 2	Fe-Oxide	6,94	1,73	Fe 59,4; O 26,23; Ti 14,33; Si 0,03;
	Chamosite	0,47	0,35	O 36,34; Fe 27,85; Si 21,75; Al 7,62; Mg 6,12; K 0,32;
	Amphibole	0,39	0,30	O 44,87; Si 21,47; Fe 12,69; Ca 7,75; Al 6,73; Mg 6,49;
	Clinochlore	0,01	0,00	O 41,21; Si 21,2; Fe 20,33; Mg 9,12; Al 8,15;
	Pyroxene	13,44	11,02	O 31,87; Si 21,73; Fe 21,41; Ca 11,15; Al 6,96; Mg 5,93; Na 0,95; Zn 0,01; K 0,01;
	Biotite	4,79	3,57	O 36,18; Si 23,96; Fe 23,08; Al 7,72; Mg 6,56; K 2,52;
	Titanite	0,01	0,01	O 34,17; Ti 30,73; Ca 22,79; Si 12,31;
	Ilmenite	64,00	76,33	Ti 38,58; Fe 37,51; O 23,92;
	Rutile	5,99	6,69	Ti 62; O 38;
	Unclassified	3,96	-	Ti 39,99; O 34,03; Fe 21,64; Si 1,33; V 1,25; Ca 0,73; Al 0,56; Mg 0,3; Na 0,06; K 0,04; Mn 0,03; Zn 0,01; Ba 0,01;
Row 3	Rutile	78,92	99,96	Ti 68,81; O 31,19;
	Biotite	0,01	0,01	O 51,09; Si 17,2; Al 15,15; K 7,3; Fe 5,86; Mg 3,41;
	Kaolinite	0,01	0,01	O 51,96; Al 25,17; Si 22,87;
	Ilmenite	0,02	0,03	Ti 40,57; Fe 31,31; O 28,12;
	Unclassified	21,04	-	Ti 80,29; O 15,15; V 4,05; Fe 0,13; Si 0,08; Al 0,07; Zr 0,06; Nb 0,04; Mg 0,04; Na 0,03; P 0,01; Ni 0,01; Y 0,01; S 0,01;

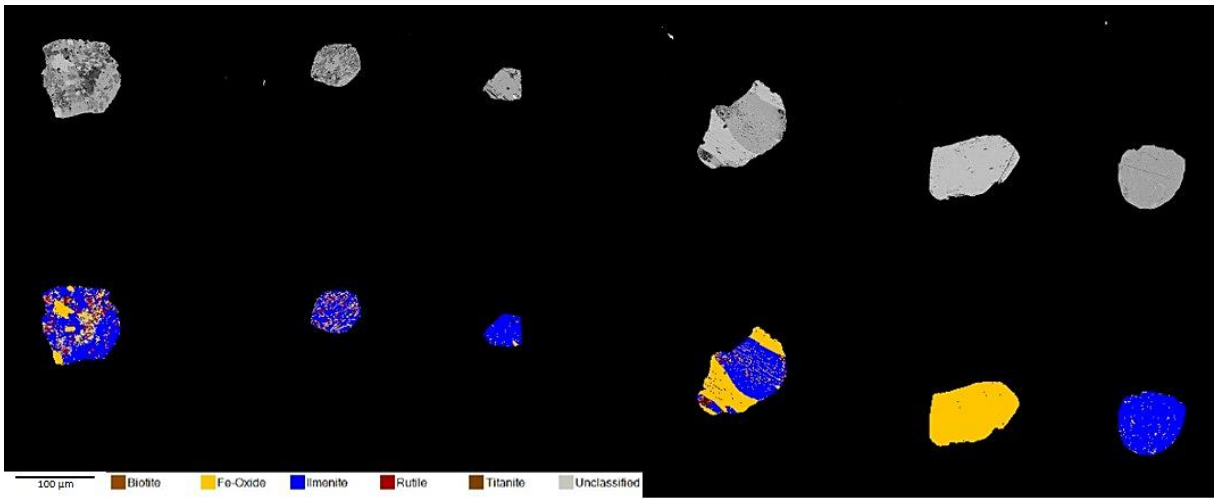


Figure 11. The upper row shows BSE images of the six grains from the Wilfley table separated "head" fraction (Row 1 in table 3). The bottom row is a mineral map of the same grains.

5.2 Marine sediment identification

A total of 389 marine sand-sized grains were selected under a stereomicroscope for subsequent petrographic examination. The strategy was to search for ejecta or impactite grains, such as impact glass, microbreccia or quartz with planar deformation features (PDFs). Not a single grain in any of the five depth intervals contain any known shock metamorphic evidence. The only grain which was found to contain glass is the volcanic grain in figure 13C. In a few grains, linear features were found in quartz and feldspars. These linear features are not considered to be PDFs, but rather inclusion trails, rutile growth or cleavage planes. Some unclassified grains were found in the 230-232 cm and 210-212 cm samples.

Core depth 230-232 cm (older than 12 500 cal. yr BP)

Table 4 shows a general description of the 230-232 cm sample under a stereomicroscope, before any grains were examined under a petrographic microscope. The grains that were considered to be of the most interest was dark-coloured grains with inclusions and polymineralic crystalline grains.

Table 4. Types of grains and their relative quantity in the 230-232 cm sample.

Relative quantity	Types of grains
Abundant	• Monocrystalline quartz grains. • Composite grains of mica and quartz. • Dark-coloured, rounded grains with inclusions. Some of these grains are relatively soft.
Moderately abundant	• Sedimentary composite grains of felsic composition. These grains are easily broken apart and held together by a fine-grained cement. • Felsic polymineralic crystalline grains. • Mafic polymineralic crystalline grains
Rare	• Dark-coloured monocrystalline grains with submetallic luster. • Other grains.

The subsequent petrographic examination revealed that most of the examined dark-coloured grains are fine-grained sedimentary grains. The mafic polymineralic crystalline grains are mainly classified as volcanic grains. The felsic polymineralic crystalline grains were unclassified. Figures 12A and B show a grain or probable volcanic origin with brown-coloured matrix and mineral fragments with unordered orientations. Some of the fragments are probable mica fragments. Figures 12C-D shows two unclassified grains. Minerals within the matrix have concave boundaries. In figure 12C a deformed mineral fragment is showed. Not a single grain in this sample showed any evidence for shock metamorphism.

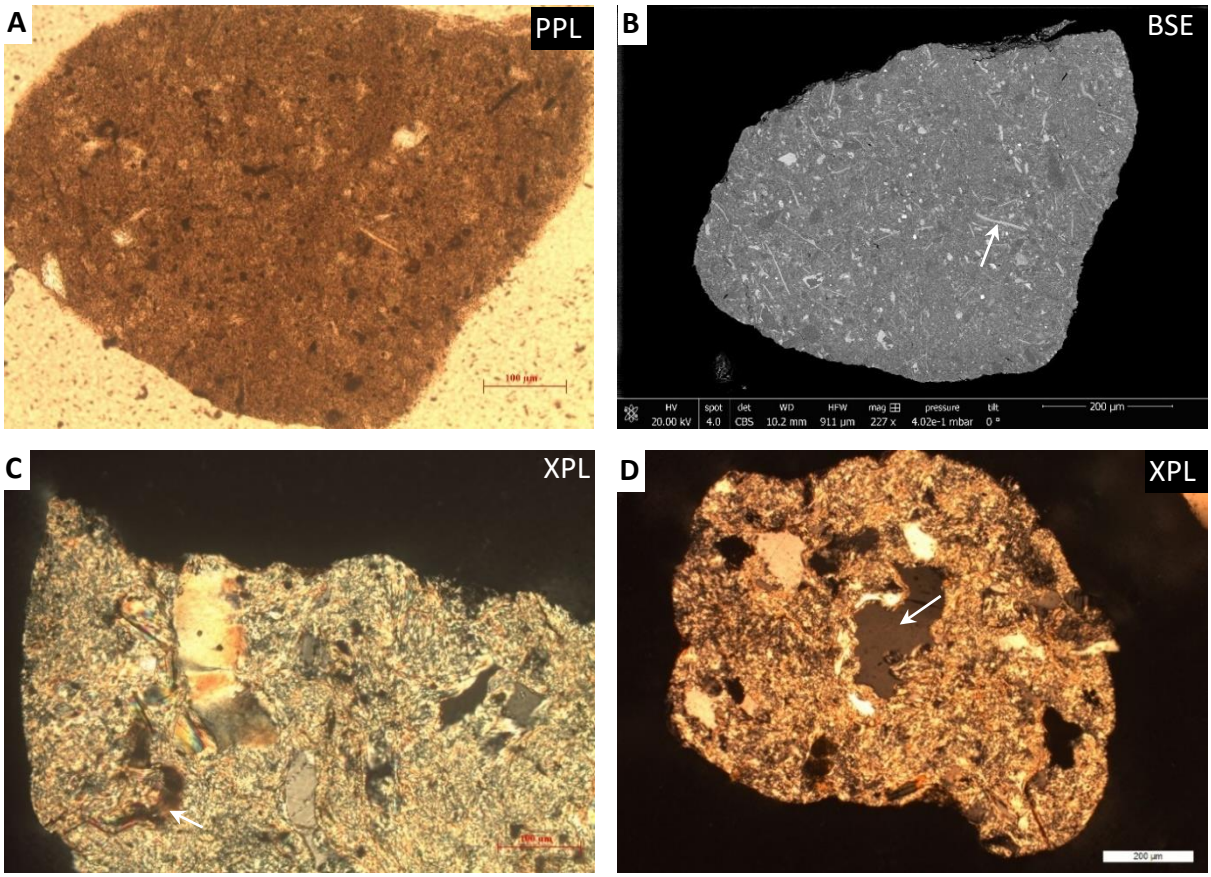


Figure 12. A) Grain with brown-coloured matrix of probable volcanic origin. **B)** BSE image of the same grains as in A) Arrow show slightly bent probable mica. **C)** Unclassified grain. Arrow shows a deformed mineral, probably mica. **D)** Unclassified grain. Arrow shows a mineral with concave boundaries.

Core depth 220-222 cm (older than 12 500 cal. yr BP)

Preliminary microscopy revealed that the grain types in the 220-222 cm sample are mostly similar to the grain types in the 230-232 cm sample (table 4). In general, the grains in the 220-222 cm sample are slightly larger compared to the grains in the 230-232 cm sample. The main difference is that the mafic polymineralic crystalline grains are more common in the 220-220 cm sample.

The subsequent petrographic examination revealed that not a single grain in this sample showed any evidence for shock metamorphism. The relatively common mafic polymineralic crystalline grains are classified as volcanic grains.

Core depth 210-212 cm (older than 12 500 cal. yr BP)

Preliminary microscopy revealed that the grain types in the 210-212 cm sample are generally similar to the grain types in the 230-232 cm sample (table 4). As for the 220-222 cm sample, the average grain size is slightly larger compared to the grains in the 230-232 cm sample and the mafic polymineralic crystalline grains are more abundant.

The petrographic examination revealed that the mafic polymineralic crystalline grains are volcanic grains with lathwork texture. One of these grains is shown in figures 13A and B. It has a typical volcanic lathwork texture with plagioclase laths together with pyroxene. Figure 13B shows cleavage in two of the adjacent pyroxene crystals. Another volcanic grain with plagioclase laths, pyroxene and zoned secondary chlorite is shown in figures 13C and D. In figure 13E, an unclassified grain is shown. The bright rectangular crystals are plagioclase. The

material in the thin grayish stripe at the upper right grain boundary in figure 13E is quartz. The large opaque mineral has a unknown chemical composition. Its high reflectance in reflected light indicate an oxide or sulfide. Another unclassified grain is shown in figure 13F. It contains biotite fragments with opaque Fe-oxide boundaries. The biotite fragments are surrounded by chlorite. Not a single grain in this sample showed any evidence for shock metamorphism.

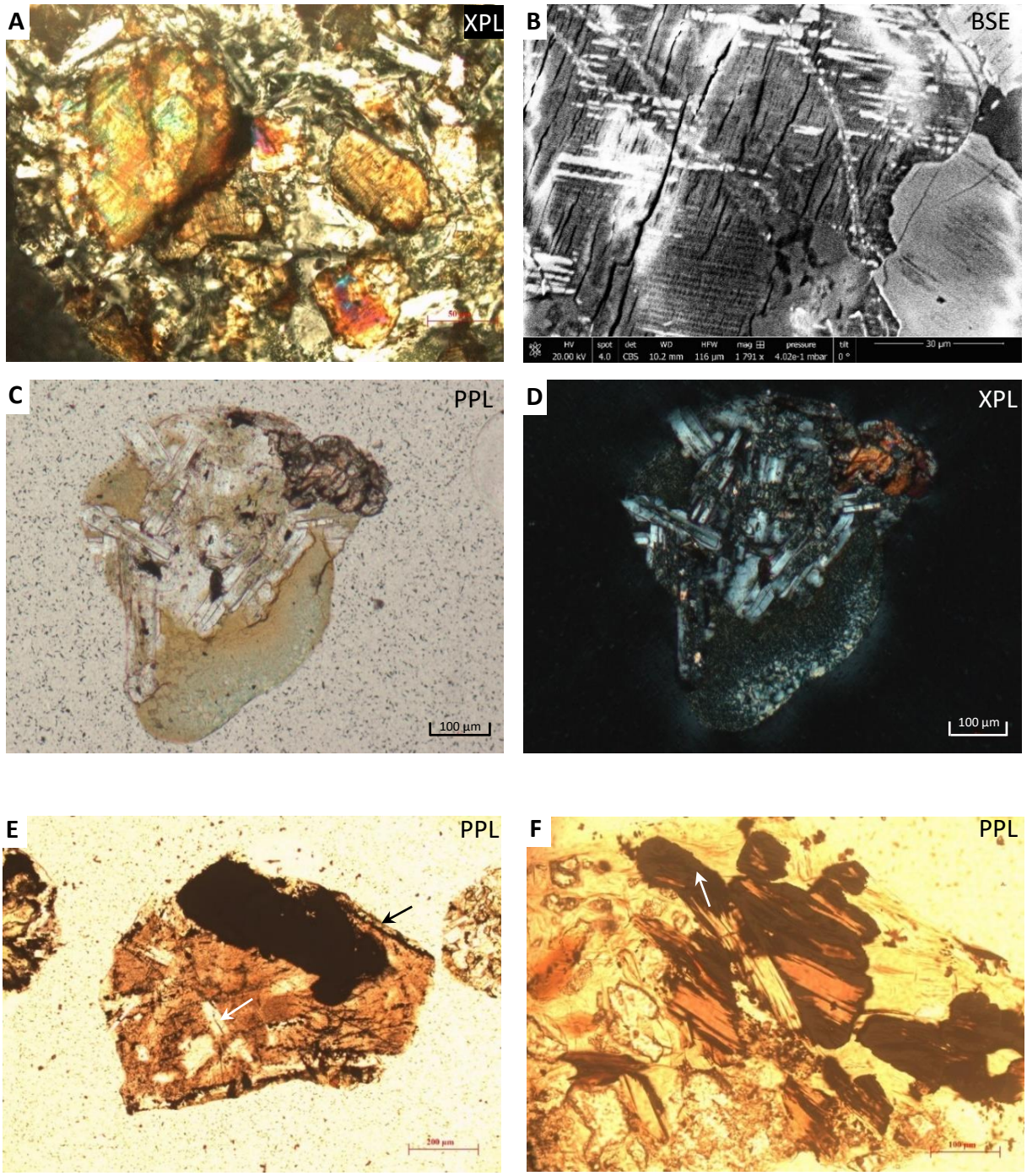


Figure 13. A) Volcanic grain with lathwork texture. **B)** Same grains as in A). Pyroxene with cleavage**. C)** Volcanic glass in zeolite. Plane polarized light **D)** Same grains as in C) in crossed polarized light. **E)** Unclassified grain. White arrow shows plagioclase. Black arrow shows quartz. **F)** Unclassified grain. White arrow shows Fe-rich biotite boundaries.

Core depth 192-194 cm (younger than 12 300 cal. yr BP)
Preliminary microscopy revealed that the average grains size of the 192-194 cm sample is smaller compared to the average grains size for the latter three intervals and the proportion of quartz grains are significantly higher. No volcanic grains were found in this sample. A high proportion of fine-grained consolidated sedimentary grains were found. Such grains were not observed in the three previously described samples. The subsequent petrographic examination of selected grains from this sample showed that none of these grains are impact related.

Core depth 190-192 cm (younger than 12 300 cal. yr BP)
Preliminary microscopy revealed that the grain types in the 190-192 cm sample are mostly similar to the grain types in the 190-192 cm sample. The main difference is that the proportion of fine-grained consolidated sedimentary grains are higher in the 190-192 cm sample than in the 192-194 cm sample. The petrographic examination of the selected grains from this sample showed that none of these grains are impact related.

5.3 Carbon petrology of HW19 impactites

After a preliminary petrographic examination of 15 thin sections, six of these were selected for further examination based upon: (i) assumed organic carbon content, and (ii) degree of shock metamorphism. The six samples (figure 14) were subdivided into three categories based upon their estimated level of shock metamorphism: (1) weakly shocked, (2) moderately shocked, and (3) strongly shocked. Based upon the proposed shock classification systems for felsic and mafic rocks in Stöffler et al (2018), all six samples have diagnostic evidence for shock metamorphism. It is however important to point out that shock-metamorphic features which provide definite evidence for meteorite impact origin (French, 1998), such as PDFs, were found in three of the samples (table 5). The other three thin section have diagnostic evidence for shock metamorphism but not evidence which can be considered to be diagnostic in a definite sense according to (French, 1998). It is also important to point out that one of the samples, HW19-39d, contains a high proportion of carbonate. As previously described, the degree of shock metamorphism at a given shock pressure, depends primarily on the mineralogical composition and the porosity of a rock or sediment sample. Furthermore, no consensus has been reached so far regarding the onset or even nature of specific shock effects in carbonates (Stöffler et al., 2018). HW19-39d is classified as moderately shocked based upon evidence for melted carbonate. SEM-EDS measurements on assumed carbonaceous material, showed that five of the six samples clearly contain carbonaceous material. Table 5 summarizes the analyses that were performed and the subdivisions of the samples. In figure 14, the selected samples are sorted by their level of shock metamorphism which increases from the top row towards the bottom row.

Table 5. Sample summary. *Vitrinite reflectance (%Ro).

Sample	Microscopy	SEM-EDS	VR*	Shock level	Diagnostic?	Carbonaceous
HW19-02a	Yes	Yes	Yes	High	PDFs in Qz	Yes
HW19-07a	Yes	Yes	Yes	Low	Brecciation	Yes
HW19-23a	Yes	Yes	Yes	Moderate	PDFs in Qz	Yes
HW19-32a	Yes	Yes	Yes	High	PDFs in Qz	Yes
HW19-39d	Yes	Yes	Yes	Moderate	Melted $CaCO_3$	Yes
HW19-40a	Yes	Yes	Yes	Low	Brecciation	No

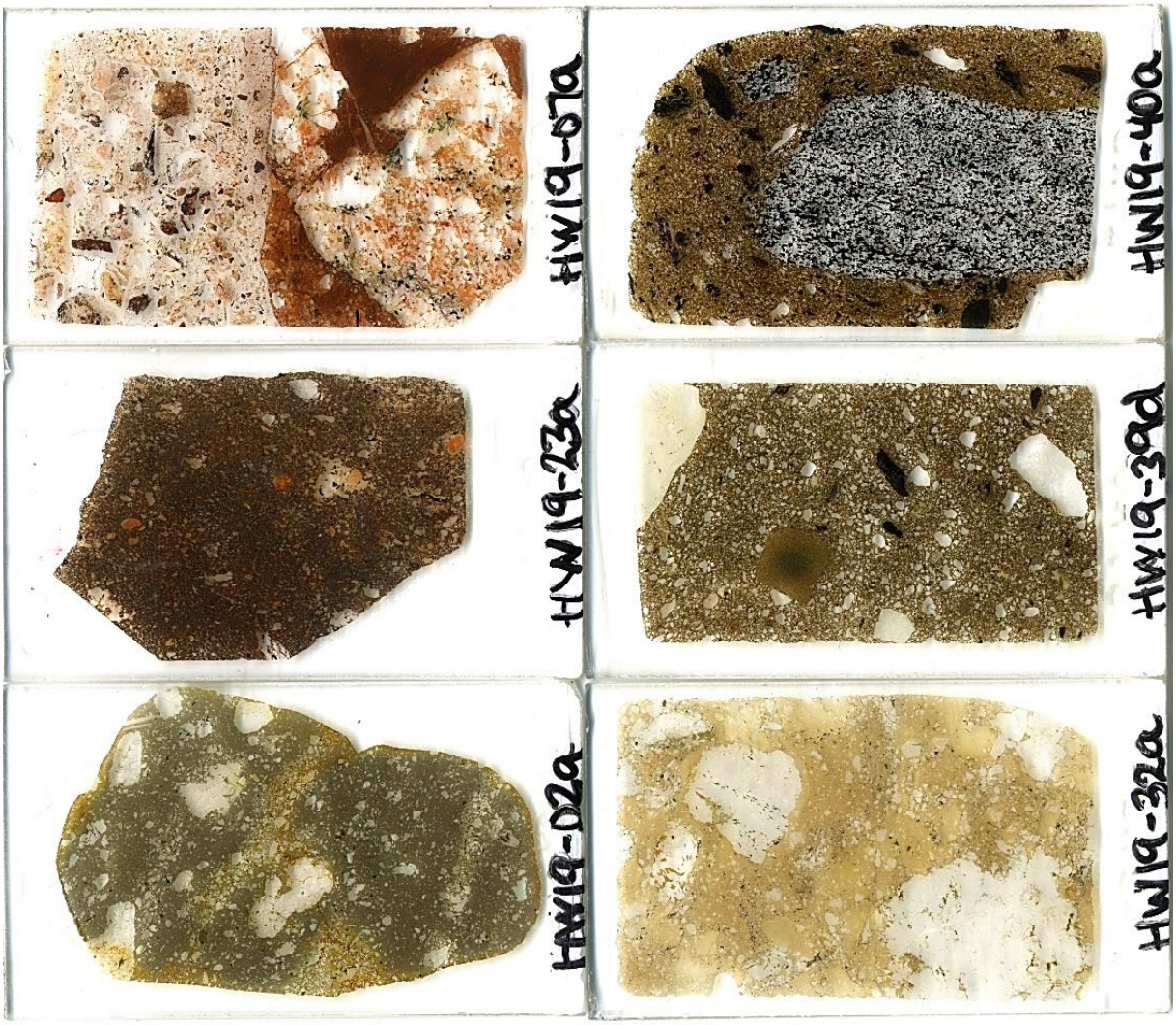


Figure 14. Overview images of the six selected HW19 samples. The samples on the top row are classified as weakly shocked impactites, the samples in the middle row are classified as moderately shocked impactites and the samples in the bottom row are classified as highly shocked impactites.

5.3.1 Weakly shocked impactites

HW19-07a – impactite lithology

Sample HW19-07a is classified as a microbreccia which contains brecciated silicate rock fragments of varying sizes. In the central part of the sample overview image (figure 14), relatively large rock fragments are cut by a relatively large, fine-grained and maroon-coloured vein, which consists of fine-grained albite and Fe-oxide. Relatively small brecciated rock and mineral fragments are located in the vein adjacent to its margin to larger rock fragments. For instance, figure 15A shows a relatively large opaque mineral fragment, with varying Fe- and Ti content (shown by SEM-EDS analysis) located adjacent to silicate rock fragments. The main evidence for shock metamorphism is the brecciated silicate rock fragments and the fine-grained maroon-coloured vein, which contains tiny minerals fragments of similar chemical composition as adjacent silicate rock fragments. The sample also contain hydrothermally deposited Fe-oxide (figure 15B) and secondary chlorite, which indicate that the rock has experienced post-shock hydrothermal alteration.

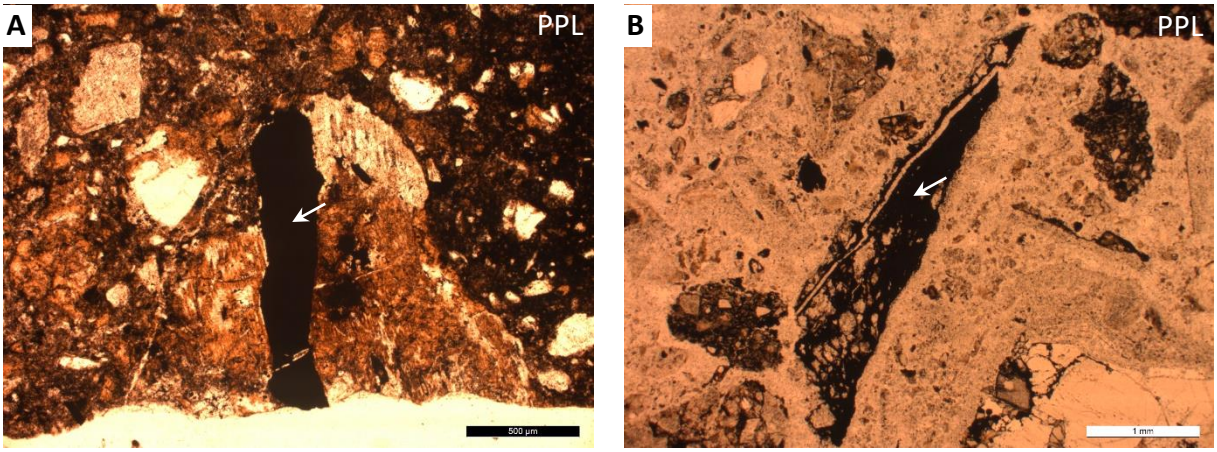


Figure 15. A) A relatively large opaque mineral fragment adjacent to silicate rock fragments. **B)** Arrow shows hydrothermally deposited Fe-oxide in a microbreccia.

HW19-07a – carbonaceous matter

In sample HW19-07a opaque matter was examined by SEM-EDS, which revealed that most of the measured material was Fe-oxide and only a small proportion was carbonaceous. Vitrinite reflectance measurements were performed on opaque fragments, which were shown to be Fe-rich minerals by SEM-EDS measurements. Figure 16 A-C show that carbon was detected in what appears to be microfractures within quartz. Spectrum 585 and 586 revealed carbon adjacent to biotite in a microfracture. The bright minerals are Fe-oxide. Carbon was also detected associated with Fe-oxide along the cleavage planes of albitic felspar (appendix B1). EDS spectum 542 shows that this material is Fe oxide associated with carbon. In general, there seems to be a minute amount of dispersed carbon in HW19-07a.

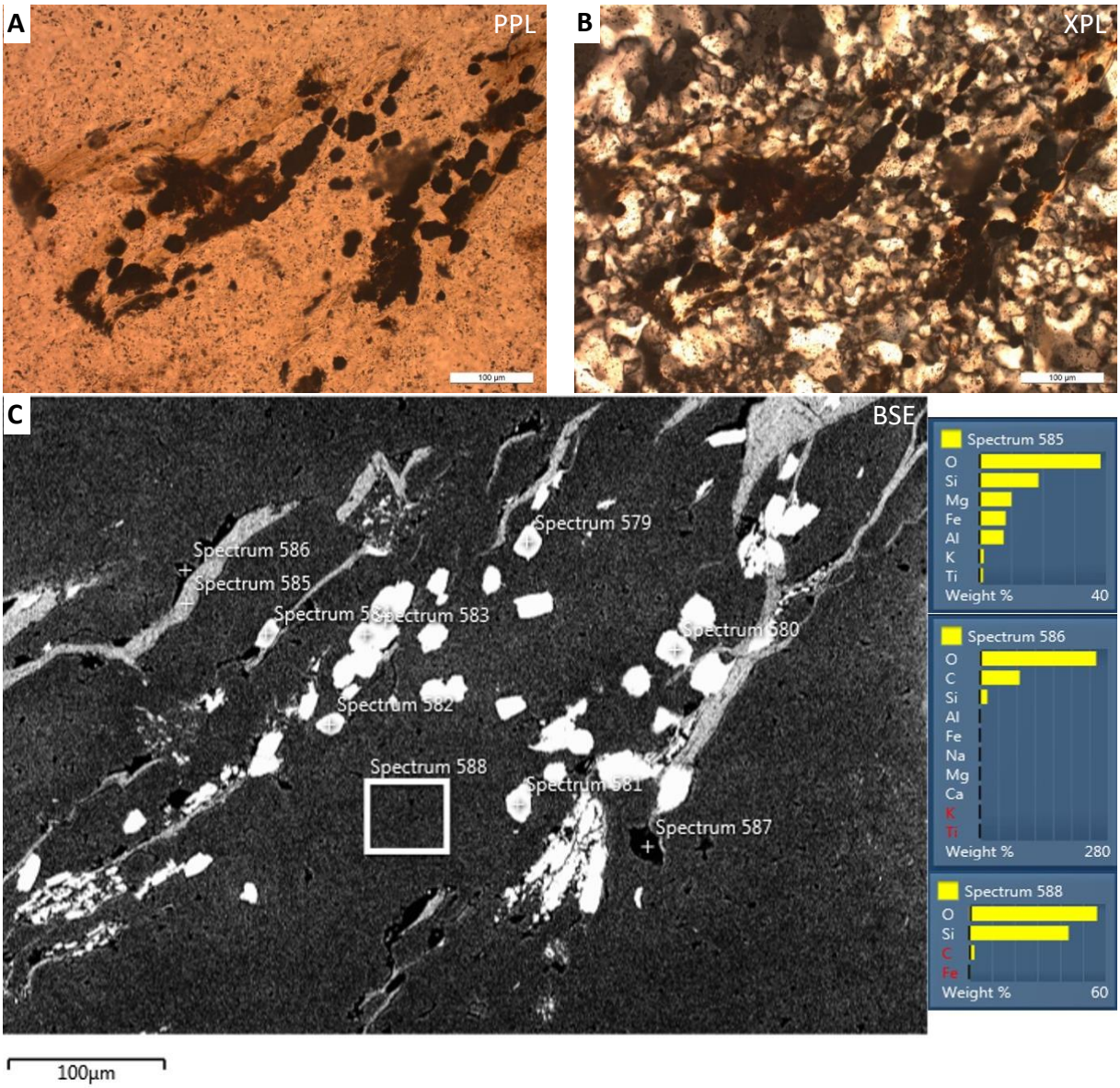


Figure 16. Carbonaceous material adjacent to biotite and Fe-oxide in what appear to be microfractures within quartz **A)** Plane polarized light **B)** Crossed polarized light **C).** Backscattered electron image and SEM-EDS spectra.

HW19-40a –impactite lithology

Sample HW19-40a is classified as microbreccia which contains relatively large semi-layered fragments and tiny quartz fragments in a phyllosilicate-rich matrix. The semi-layered fragments are either comprised of Fe-oxide and phyllosilicate or iron oxides and quartz. These fragments seem to be replacements rather than rock fragments, probably due to post-impact hydrothermal activity (A. Garde, personal communication). The main evidence for shock metamorphism is brecciated angular fragments of quartz, which testifies to mineral fracturing.

HW19-40a – opaque matter

In sample HW19-40a all opaque matter which was suspected to be carbonaceous were shown by reflected light microscopy and SEM-EDS analysis to be Fe-oxide. One such examples is shown in figure 17A and B. HW19-40a is therefore classified as non-carbonaceous.

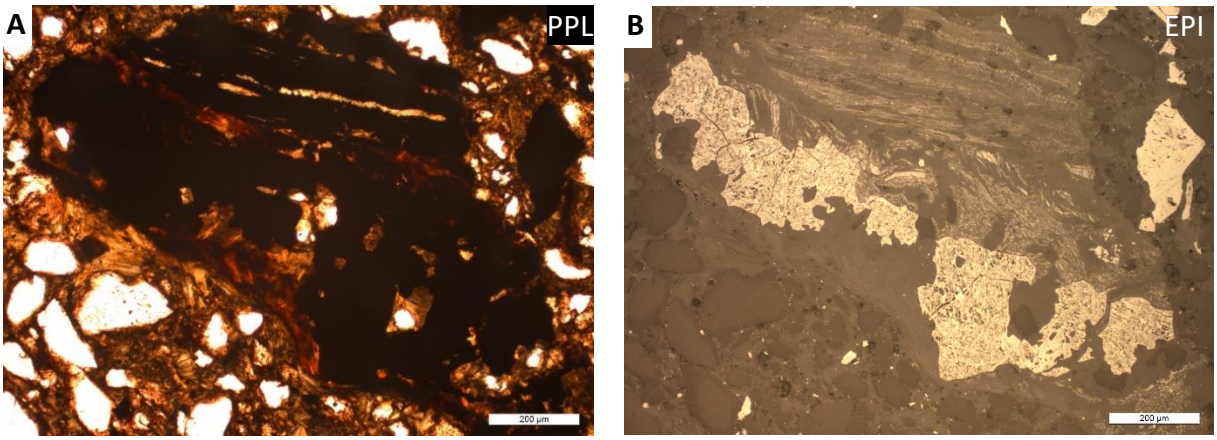


Figure 17. Opaque Fe-rich fragment surrounded by a phyllosilicate-rich matrix and brecciated quartz fragments. **A)** In plane polarized light **B)** In reflected light.

5.3.2 Moderately shocked impactites

HW19-23a – impactite lithology

Sample HW19-23a is classified as a microbreccia with abundant angular silicate fragments of varying sizes in a Fe-rich brown-coloured matrix. A finely dispersed Fe-rich opaque material is abundant in between silicate fragments in the fine-grained matrix. This material exhibits high reflectance and melt grain textures. The main evidences for shock metamorphism are quartz fragments with PDFs and ballen quartz (figure 18 A and B). Ballen quartz may be related to the impact-produced formation of fused silica glass or diaplectic quartz glass (French and Koeberl, 2010).

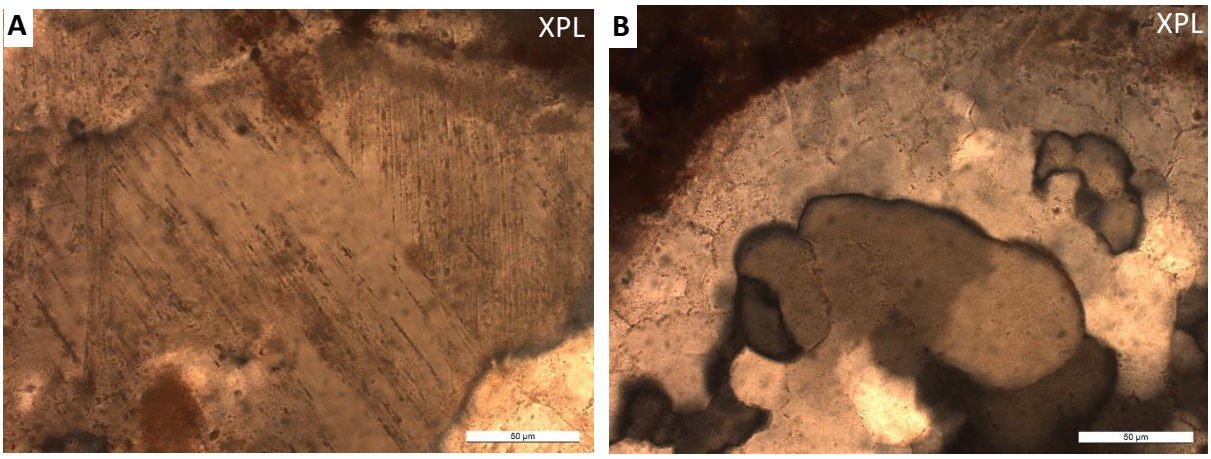


Figure 18. A) Likely two sets of crossing PDFs in quartz. **B**) Likely ballen quartz.

HW19-23a – carbonaceous matter

Sample HW19-23a, contains only a small carbon component. In figure 19A, spectrum 51 shows that carbon was detected in a particle which has a biotite-like chemistry excluding the carbon. In figure 19B and C a similar particle is shown. Figure 19C shows that the particles exhibit relatively low reflectance. These types of particles have a similar apperance as the partice in figure 19A and are quite abundant in the sample. Vitrinite reflectance measurements were performed on opaque fragments in sample HW19-23a, which were shown to be Fe-rich minerals by SEM-EDS measurements. Spectrum 52 might be from a sample hole.

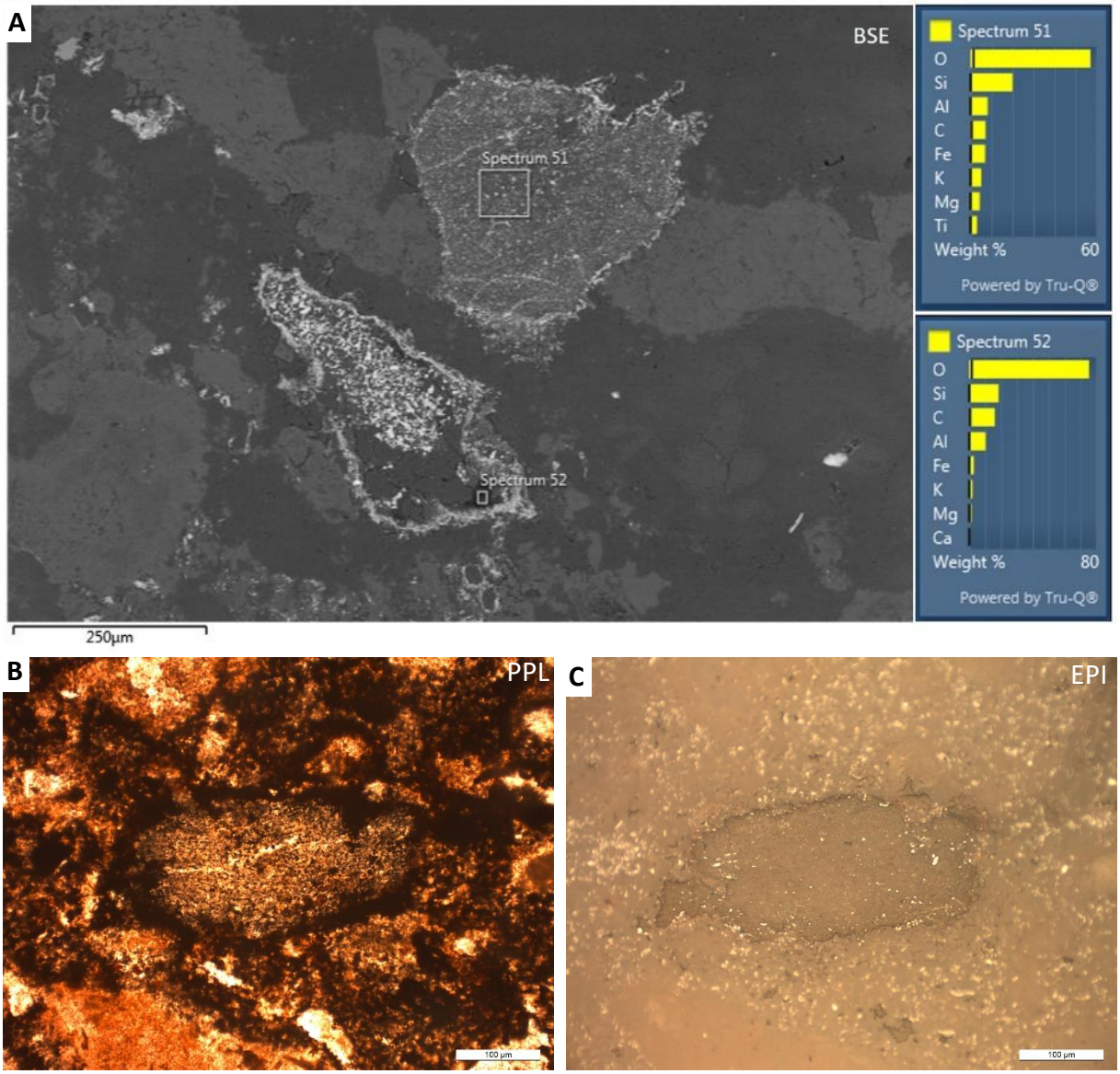


Figure 19. A) Backscattered electron image and SEM-EDS spectra of carbonaceous fragments. **B)** Possible carbonaceous fragment. **C)** The same fragments as in B) in crossed polarized light.

HW19-39d - impactite lithology

Sample HW19-39d is classified as a polymict microbreccia comprised of mainly carbonate- and silicate fragments together with a high proportion of organic carbon particles in a Ca-rich (EDS spectrum 265, appendix B2) matrix. The matrix is brown-coloured and contains tiny brecciated fragments. Besides the brecciation, the main proof of shock metamorphism in the sample are kinked biotite (figure 20A) and melt-texture in carbonate clasts (figure 20B). Another thin section from the same rock sample, HW19-39a, contains a carbonate-melt clast with carbonate-filled vesicles (A. Garde, personal communication). Notably, the overview image (figure 14) of the sample shows a crude NW-SE trending layering of the mineral fragments.

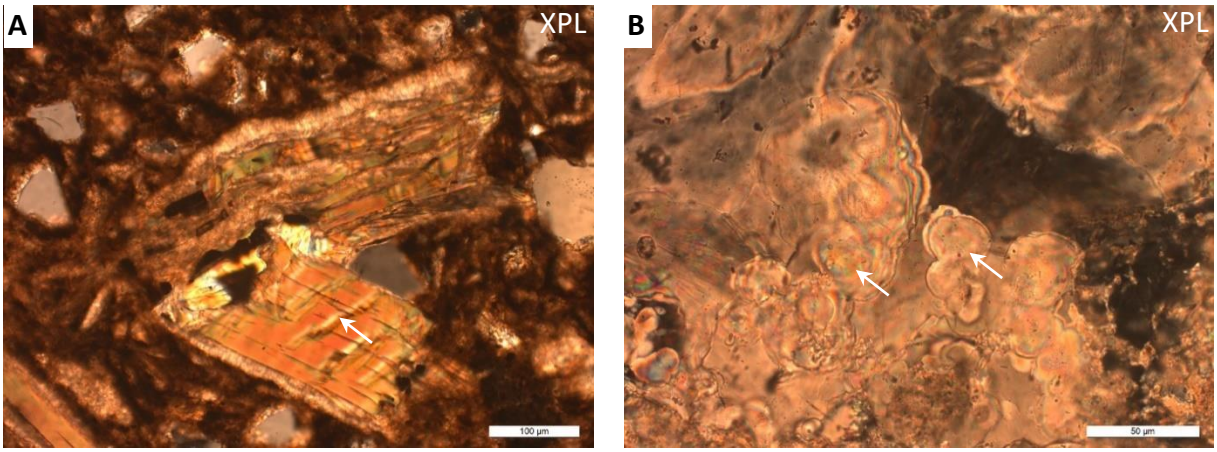


Figure 20. A) Kink bands in a biotite fragment surrounded by brown-coloured matrix and tiny mineral fragments. **B)** Melt-texture in a carbonate fragment.

HW19-39d - Carbonaceous matter

Sample HW19-39d contains a high proportion of carbonaceous particles. Some of these particles have cellular textures. A relatively large carbonaceous particle in the sample exhibit even-sized and blocky cellular texture figure 21A). Figure 21B shows a transverse cross-sectioned organic carbon piece with cellular texture. The formed cells are variably filled with the matrix material, which is why the voids in the cell centres have different sizes. SEM-EDS-measurements of carbonaceous matter from sample HW19-39d is shown in appendix B2.

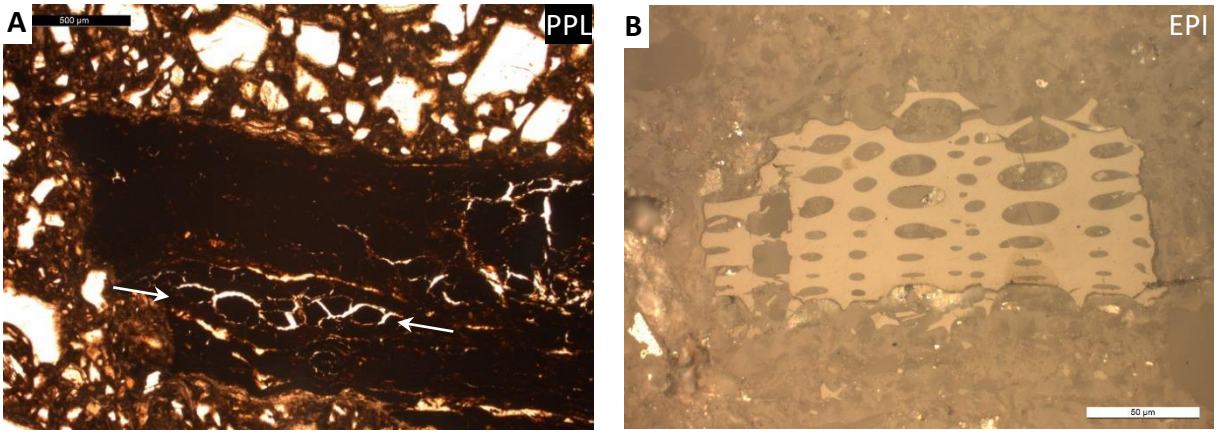


Figure 21. A) Relatively large particle with cellular texture shown by white arrows **B)** Organic carbon piece with regular rows of former cells.

Vitrinite reflectance measurements of carbonaceous particles in sample HW19-39d revealed two populations with respect to Ro values. The largest population has Ro values between ~0.3 to 1% (figure 22A). The histogram shows that the majority of the 76 measurements have Ro values < 0.5 %. Two of these measurements are shown in figure 22C. The second population, which has Ro values between 1 and 2%, is smaller and accounts for almost 20 % of the measurement in the histogram in figure 22A. Almost 50 % of the measured Ro values for this population is between ~1.5 to 2%. The reflectance measurements in figure 22B were solely performed on the particle in figure 22D.

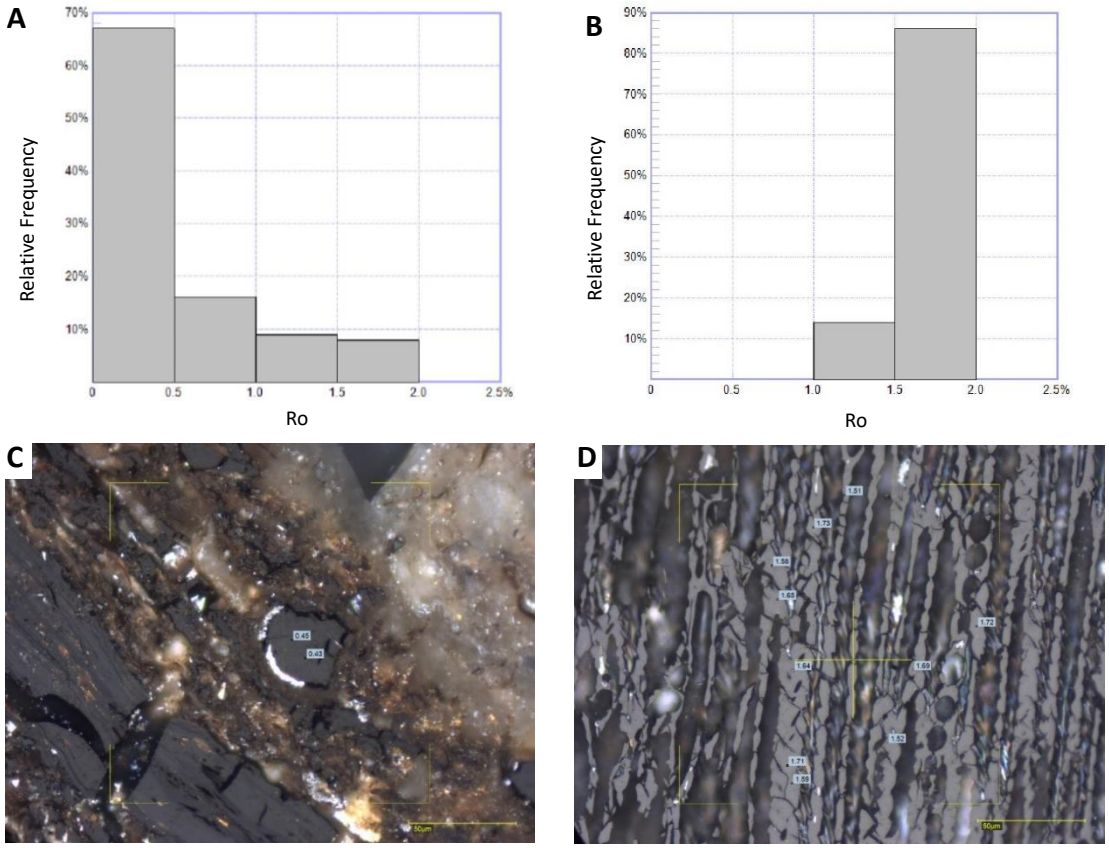


Figure 22. A) Histogram of 76 vitrinite reflectance measurements on multiple particles. **B)** Histogram of 21 vitrinite reflectance measurements on the same organic carbon particle. **C)** Two measurements with Ro < 0.5%. **D)** 10 measurements of a single organic carbon particle. The measurements in B) are from the same particle.

5.3.3 Highly shocked impactites

HW19-02a – impactite lithology

Sample HW19-02a is classified as a microbreccia. The brown-coloured matrix is semi-crystalline and contains prismatic pyroxene microlites (Spectrum 464, appendix B3). At some places the brown matrix exhibits flow-texture adjacent to mineral fragments (figure 23A). A high proportion of the quartz fragment are shocked, ”toasted” quartz (figure 23B). At least one granular zircon was found in another thin section, HW19-02b, which is from the same sample (A. Garde, personal communication).

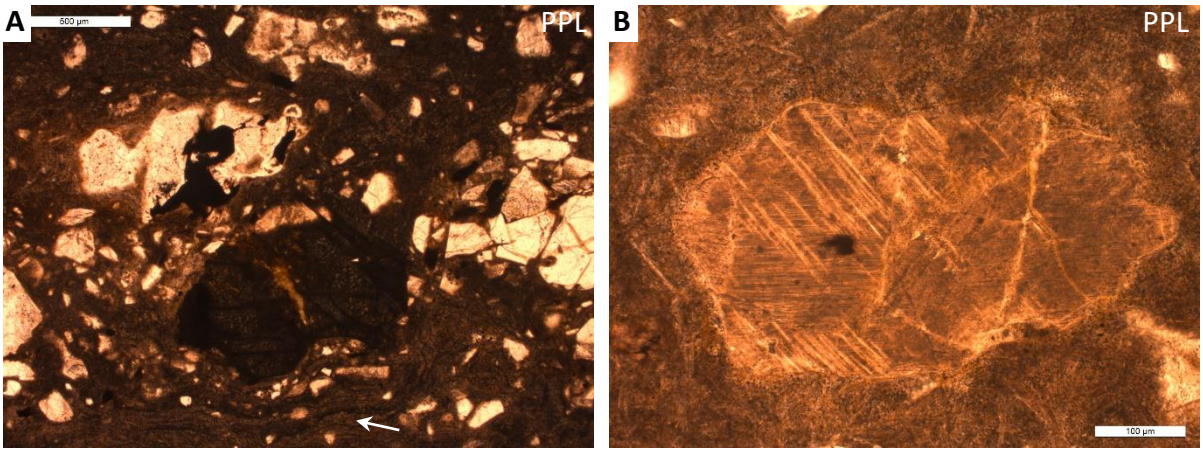


Figure 23. A) Flow-texture in the brown-coloured matrix below the relatively large dark-coloured mineral fragment in the bottom centre of the image **B)** Shocked, ”toasted”, quartz with at least one set of PDFs.

HW19-02a - carbonaceous matter

Different types of carbonaceous matter were found in sample HW19-02a. Amorphous matter along the boundary of a quartz fragment was confirmed to be carbonaceous (spectra 466 and 467, appendix B3). Elongate carbonaceous particles (figure 24 A and spectrum 377 in appendix B4) were found which have darker boundaries than their interior. There interior seems to have an indistinct layer-texture. Carbon was also detected in fractured particles. Figures 24B shows one of these particles which was confirmed to be carbonaceous (appendix B5). Another fractured carbonaceous particle (appendix B6) is associated with sphalerite-like and titanite-like minerals. Multiple curved and tapering fractures run along the length of the particle. In sample HW19-02a, vitrinite reflectance measurements were performed on opaque fragments, which were shown to be Fe-rich minerals by SEM-EDS measurements.

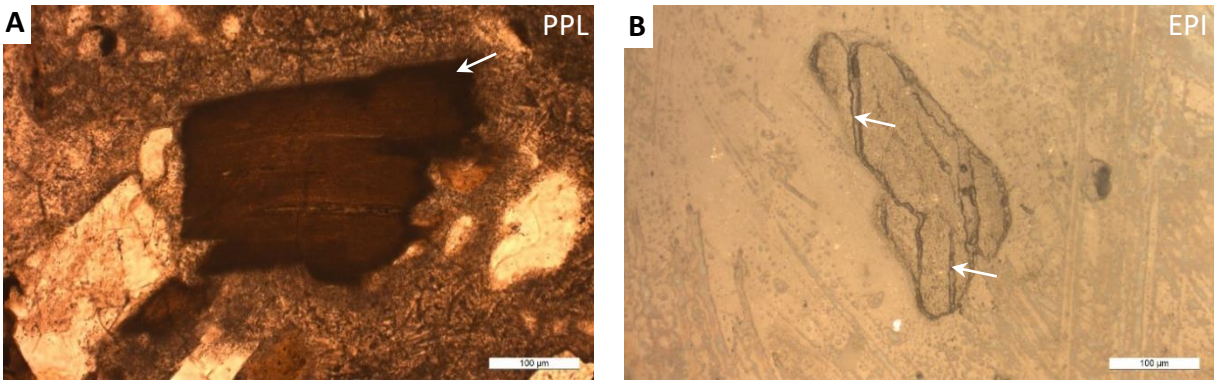


Figure 24. A) Arrow shows darker boundaries. **B)** Arrows show fractures.

HW19-32a – impactite lithology

Sample HW19-32a is classified as a microbreccia with zones of fresh glass with turbulent flow-texture. The matrix is composed of two distinct areas of light- and dark yellow/brown shock-melted glass phases whit sharp boundaries to one another. Blebs of one glass phase commonly occur in the other. SEM-EDS measurements confirmed that the glasses have different chemistry. The brighter glass has a higher Fe-content than the darker melt phase, which is more Si-rich. The brighter glass exhibit abundant quench fractures. The sample contains a wide range of fragments including partly melted rock fragments, fractured silicate fragments, opaque mineral fragments and carbonaceous particles. Silicate mineral- and rock fragments have disintegrated and wavy grain boundaries. Figure 25A shows a shocked, ”toasted” quartz fragment. Figure 25B shows a zircon with a granular texture which was found in the sample.

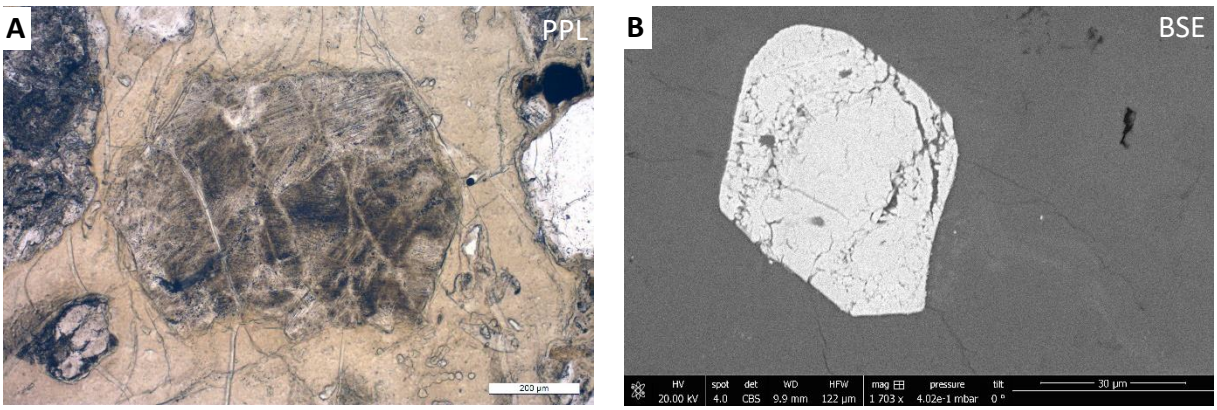


Figure 25. A) Shocked,” toasted” quartz grain surrounded by shock-melted glass. The PDFs have two distinct orientations and at least one more (ESE-WNW) **B)** Granular zircon.

HW19-32a - carbonaceous matter

Sample HW19-32a contains multiple types of carbonaceous particles. Two particles with blocky texture exhibit tiny and narrow fractures, which are radiating inwards a short distance from the outer particle boundary, towards its centre (figure 26A and D). EDS spectra of the latter two particles are shown in appendix B7 and B8. A carbonaceous particle with possible cellular texture (figure 26B) appears to have relatively high reflectance, but not as high Ro as for example iron oxides. Multiple vesicles containing a mix of material were found in the sample. The vesicles have distinct walls and contain carbonaceous material (appendix B9) together with tiny mineral fragments. The carbonaceous matter in sample HW19-32a was confirmed by SEM-EDS measurements.

Seven vitrinite reflectance measurements were performed on three particles (figure 26C). One of these particles was analyzed with SEM-EDS. Spectra 133 and 134 in appendix B7 shows that the measured particle is carbonaceous. Figure 26D shows that it has the highest Ro values (2.54 % to 2.88 %) closer to its boundaries, whereas it has lower Ro in its centre (2.25 %) The other two particles, which showed higher Ro values where not found during SEM-EDS analysis. It is possible that these two particles might be minerals and not organic material.

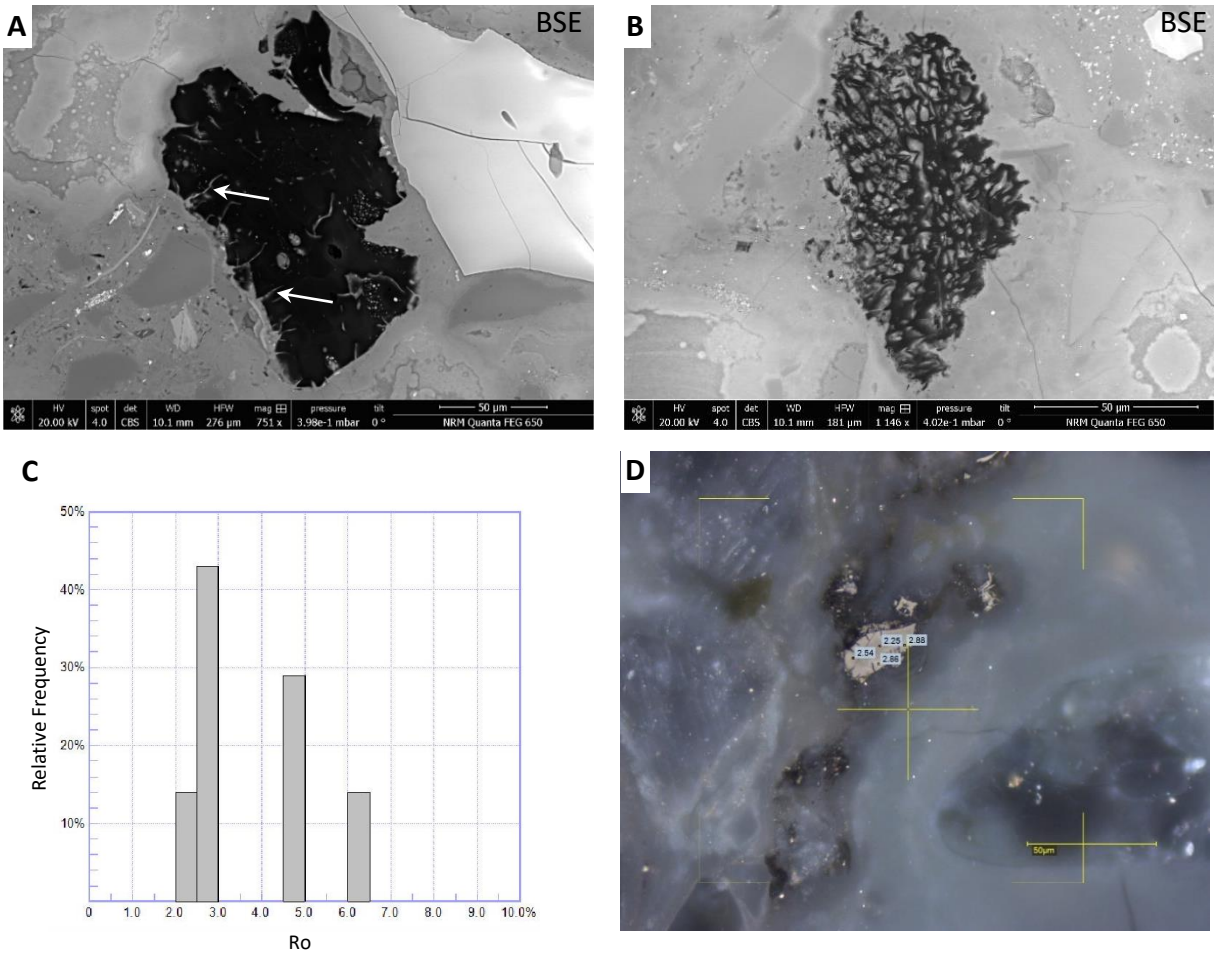


Figure 26. A) Organic carbon particle with blocky texture. Arrows show narrow fractures. **B)** Organic carbon particles with possible cellular texture and relatively high reflectance. **C)** Histogram of Ro measurements in sample HW19-32a. **D)** Four Ro measurements of an organic particle.

6. Discussion

In this chapter the author discusses the main results in the following order: 1) heavy mineral identification, 2) marine sediment identification and 3) HW19 impactites

6.1 Heavy mineral identification

6.1.1 The apparent absence of chromite in HW21-2016

Although no chromite or any composite grains with chromite were found in this study, it is known that there is a Cr anomaly in the HW21-2016 sand. Kjær et al (2018), reported a 25–30 ppm higher Cr content in HW21-2016, compared to reference samples unaffected by the hypervelocity impact and likely derived from the local Inglefield Land mobile belt rocks. Kjær et al (2018) argued that the Cr-anomaly was unlikely to stem from Cr-rich terrestrial target rocks since the only known terrestrial source that contains high enough platinum-group elements (PGE) concentrations for it to be eroded and diluted to produce the concentrations observed in HW21-2016, are rare sulfide-rich chromitite rocks, such as the Platreef deposit of the Bushveld Complex. Furthermore, Kjær et al (2018) argued that sulfide-rich chromitite rocks would naturally produce abundant detrital Mg-rich and Ti-poor chromite grains. Such grains were neither observed by Kjær et al (2018) nor in this study. Although no chromite was found in this study, the Cr and siderophile anomalies in the HW21-2016 sand are now very unlikely to stem from a hidden terrestrial chromitite deposit.

The apparent absence of chromite in the HW21-2016 subsample in this study corroborates the significance of the PGE spectra in Kjær et al (2018), which points to a strongly fractionated Duchesne (type IVA) iron meteorite. However, according to Kjær et al (2018), the Cr concentrations of any type of iron meteorite are too low to produce the additional 25–30 ppm Cr anomaly in the HW21-2016 sediment. Therefore, Kjær et al (2018) argued that it may reflect a Cr-rich component in addition to iron in the impactor, such as a pallasite component. Moreover, Kjær et al (2018), noted that significantly higher PGE concentrations in the subsample HW21-2016(1)B, compared to the other HW21-2016 subsamples used in their study, points to a heterogeneous nature of the siderophile-rich component in the sediment.

With the absence of chromite in the heavy mineral identification performed in this study, it was not possible to test whether the Cape York meteorites and the HIC possess a pre-terrestrial affinity. However, the absence of chromite in all tested subsamples of HW21-2016, corroborates the significance of the metal signal in Kjær et al (2018), which points to a fractioned iron meteorite Hiawatha impactor. Hence, the investigation of a possible link between the Hiawatha impactor and the Cape York is more significant now, than it was before the heavy mineral identification in this study. Since no chromite was found in this investigation, the research question remains open and is recommended to be investigated more in the future.

6.2 Marine sediment identification

6.2.1 The apparent absence of impactite grains in 012P

Not a single grain with diagnostic evidence for shock metamorphism was found in the marine sediment. Some of the grains could be hydrothermally altered. Such grains might come from the impact but it is unlikely and would be difficult to prove. The only grain which contains glass of the examined grains is classified as a volcanic zeolite (A. Garde, personal communication). The apparent absence of impactite grains in marine core 012P suggests two possibilities: either the samples are barren with respect to impactite grains, or potential impactite grains were not found with the available analytical methods.

With the apparent absence of impactite grains in the marine sediment, the probability of the HIC being coeval with the YD seems to be small. However, site 012 is located SW of the HIC (figure 2A). Given that the majority of Earth-crossing asteroids move in or near the ecliptic plane, together with the strong curvature of the Earth at the location of the HIC (78.72°N), the most probable scenario would be a northward-directed oblique impact. Such an impact would have sent most of the ejecta northwards (Shuvalov, 2011). Thus, the probability of finding ejecta from the Hiawatha impact in the marine core 012P, might not be so high under any circumstance. If the impact crater is as young as from the YD, it might be possible that impactites would have been transported to site 012 as ice-rafted debris. However, the glaciofluvial sediment sample HW21-2016 is very diluted by other non-impactite material. Hence, it is reasonable to assume that if Hiawatha impactite grains are present in the marine core 012P, these grains would also be very diluted by other material in the marine sediment.

6.2.2 Ejecta distribution of the Hiawatha impact

Although the HW19-impactites could potentially have been glacially transported from loose material to the sites HW19-A-C (figure 2B), there is yet no proven ejecta layer associated with the HIC. If the impact crater is geologically old, then an ejecta layer might be difficult to find. Assuming that the crater is coeval with the YD, the lack of ejecta south of the crater in Greenland ice cores and in the marine core 012P, could be explained by a northward-directed low-angle impact. In such a possible scenario, as previously were described (in 6.2.1), the highest probability of finding potential YD ejecta would most likely be north of the impact crater, possibly in marine sediment or in ice sheets in the Canadian Arctic.

In the possible scenario that the Hiawatha impact occurred on a relatively large ice sheet similar to the present-day GrIS, the fraction of non-ice ejecta would be smaller compared to an impact on ice-free land, the ejecta angle would be steeper and the flowback of material back into the crater more would be more extensive (Senft and Stewart, 2008). Furthermore, if permafrost was present in the target of the Hiawatha impact, the ejecta velocity would be lower. The reason why ice sheets and buried ice layers have such influence is shock impedance and the strength mismatch between layers of icy and rocky materials (Senft and Stewart, 2008). Moreover, if a high proportion of the ejecta landed on a similar continental ice sheet as the present-day GrIS under present-day conditions, the ejecta would probably have been transported to the ice margin within ~10 ka (Kjær et al., 2018).

In summary, the apparent absence of ejecta or impactites in the marine core 012P does not preclude that ejecta or impactite grains from the Hiawatha impact can be found in marine sediment or other sedimentary deposits from the YD. Further investigation of possible marine- and ice core records from around this time period is recommended north of the crater.

6.3 Organic matter in Hiawatha impactites

6.3.1 Organic carbon variation

Table 6 contains a sample summary of the organic carbon variation in the six investigated samples relative to their degree of shock metamorphism. This investigation has identified five distinct groups of organic carbon in the Hiawatha impactites:

1. Amorphous carbonaceous matter
2. Transformed carbonaceous particles
3. Blocky organic carbon particles
4. Organic carbon particles with cellular texture
5. Carbonaceous vesicles

Table 6. Organic carbon variation relative to shock level. *Approximate shock pressure **Estimated post-shock temperature. ***Converted from 2000 K in Osinski and Spray (2001). Qz = quartz.

Sample	Shock level	Shock metamorphic effects	Shock pressure*	Post-shock temperature**	Carbon group
HW19-02a	High	"Toasted" Qz* and granular zircon	35-50 GPa[a]	>1670 °C[b]	1 and 2
HW19-07a	Low	Rock fracturing, brecciation	2–6 GPa[c]	<100 °C[c]	1
HW19-23a	Moderate	PDFs in Qz and "ballen Qz"	>35 GPa[d]	>1200 °C[e]	2
HW19-32a	High	Melt-glass and granular zircon	>60 GPa[c]	>1670 °C[b]	3, 4 and 5
HW19-39d	Moderate	Kinked biotite and melted carbonate	10–25 GPa[f]	>1727 °C***[f]	3 and 4
HW19-40a	Low	Rock fracturing, brecciation	2–6 GPa[c]	<100 °C[a]	-

[a] Wittmann et al (2006), [b] Cavosie et al (2016), [c] French (1998), [d] Stöffler and Langenhorst (1994), [e] Short (1970) and [f] Osinski and Spray (2001).

1. Amorphous carbonaceous matter

In two of the six samples, amorphous carbonaceous matter was identified. In figure 27A amorphous brown-coloured carbonaceous material are shown at the boundary of a quartz fragment in sample HW19-02a. The shock metamorphic evidence in HW19-02a testifies to a high post-shock temperature (table 6). The semi-crystalline matrix in HW19-02a contains tiny pyroxene crystals (appendix B3), which indicate shock-melting and subsequent cooling slow enough for the pyroxenes to crystallize. Carbonaceous matter in the target might have been incorporated into the shock-melt during the impact event and subsequently modified into an amorphous structure during the cooling of the shock-melt. In the two weakly shocked samples, assumed organic carbon that experienced the impact was only detected in HW19-07a. The minute amount of amorphous carbonaceous matter detected in HW19-07a is associated with microfractures (figure 27B), microbreccia clasts and cleavage planes in feldspar. Parnell and Lindgren (2006) proposed that amorphous carbon, found within microfractures in lithic breccia and suevite from the Gardnos impact crater in Norway, could have been entrained during post-impact hydrothermal activity. Furthermore, Parnell and Lindgren (2006), argued that since microfracture through quartz heal rapidly (Brantley, 1992), the hydrothermal activity mostly likely took place immediately post-impact. Evidence for hydrothermal activity in HW19-07, together with carbon associated with Fe-rich matter in microfractures, suggest a similar scenario. It is also important to note that carbon with associated chlorine peaks were detected at other places in HW19-07a. Although, no chlorine peaks were detected in the carbon in figure 27B, artificial carbon from epoxy resin cannot be ruled out.

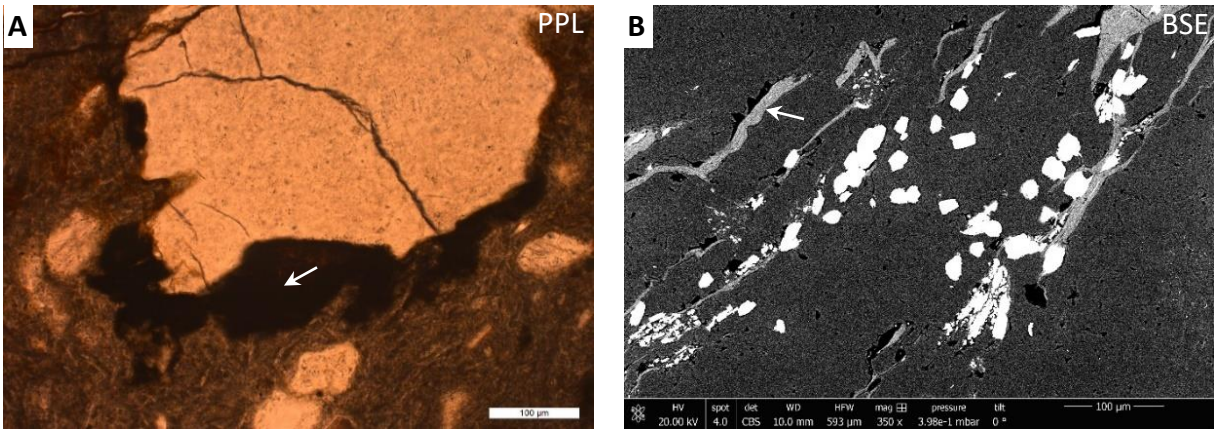


Figure 27. A) Sample HW19-02a. Amorphous carbonaceous matter along the boundary of a fractured quartz fragment **B)** Sample HW19-07a. Microfractures in quartz containing amorphous carbonaceous matter and biotite.

2. Transformed carbonaceous particles

This group comprises particles with varying elemental compositions and relatively low apparent carbon contents, shown by SEM-EDS analysis. Such particles are most abundant in HW19-02a (figure 28A). Similar particles were also found in HW19-23a (figure 19A-C). Some of these particles in HW19-02a exhibit shrinkage textures such as branching cracks (shown by arrows in appendices C5 and C6). Garde et al (2020) described branching and tapering systems of shrinkage cracks in lignite/charcoal and proposed that they were caused by impact-induced rapid loss of volatile components by heating. The same scenario is interpreted for the transformed carbonaceous particles in HW19-02a and HW19-23a. The particle in figure 28A could be a shocked mixture of fine-grained clay and organic matter which stems from an unmetamorphosed surficial deposit (A. Garde, personal communication). As was previously described, the tiny pyroxene crystals in the semi-crystalline matrix in HW19-02a indicate shock-melting and subsequent cooling slow enough for the pyroxenes to crystallize. The wood-like particles (figure 28B) could be plant matter that got incorporated into the shock-melt, possibly from unmetamorphosed surficial deposits of organic matter.

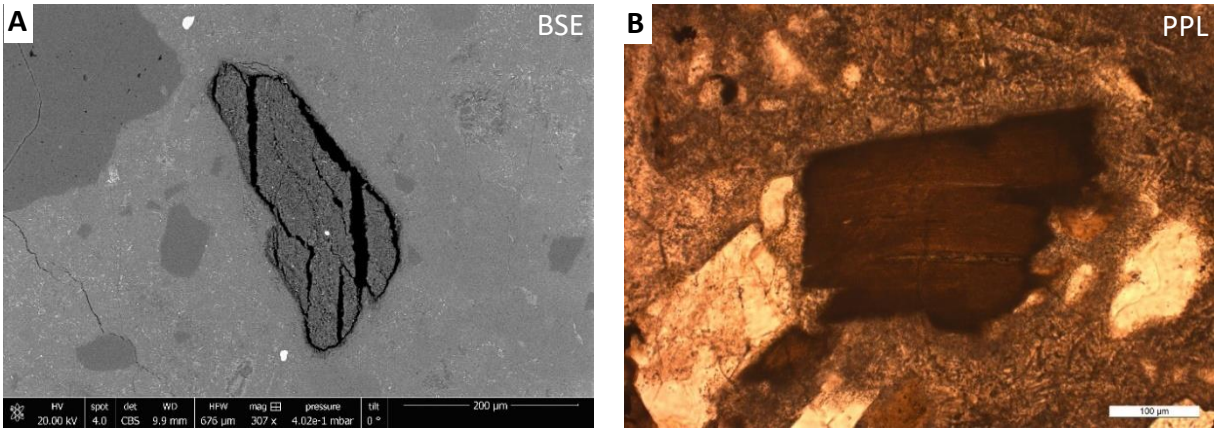


Figure 28. A) Sample HW19-02a. Carbonaceous particle with epoxy-filled shrinkage fractures. **B)** Sample HW19-02a. Wood-like particle.

3. Blocky organic carbon particles

Blocky organic particles were found in HW19-32A and HW-39D and are defined as particles with a blocky texture and a high carbon content shown by SEM-EDS measurements. In HW19-32A, blocky and elongate carbon-rich particles (figure 29A) were found adjacent to shock-

melted glass. Despite the estimated high post-shock temperatures (table 6) for this sample, these particles are well-preserved. C-H-O compounds in these particles were likely volatilized during the impact event. The preservation of these particles in HW19-32a could be explained by a very short duration of the high temperature excursion. The shock-melted glass in HW19-32a shows signs of rapid cooling, such as quench fractures. In HW19-39D, a high proportion of blocky organic particles (figure 29B) have low Ro values and exhibit a segmented texture with branching cracks. As for the previously described transformed carbonaceous particles, these cracks are interpreted as evidence of shrinking due to loss of volatile components by heating.

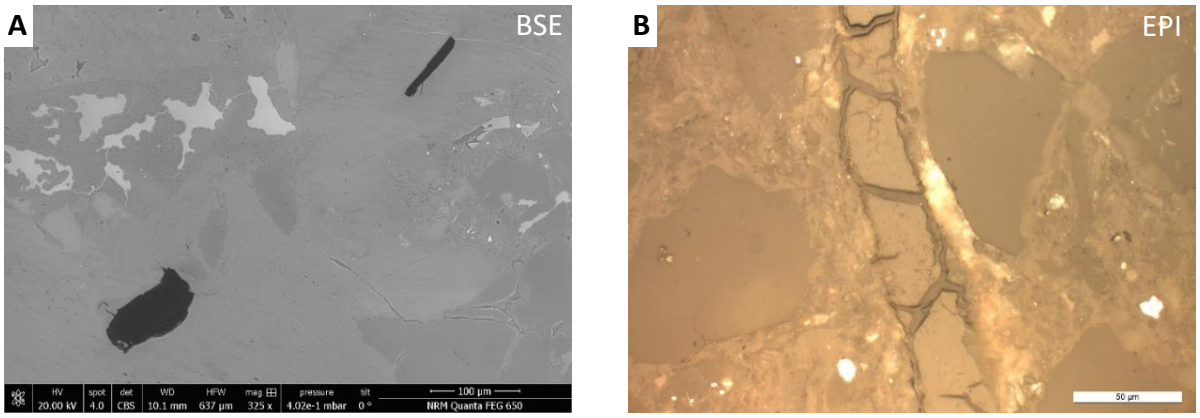


Figure 29. A) Sample HW19-32a. Two blocky elongate organic particles. In BSE images dark colour indicates material with low atomic number in the periodical system. **B)** Sample HW19-39d. Blocky segmented organic particle (centre of the image) with branching cracks.

4. Organic carbon particles with cellular texture

Organic particles with cellular texture were found in HW19-32a and HW-39d and are defined as particles with cellular texture and a high carbon content shown by SEM-EDS measurements. In HW19-32a one organic particle with possible cellular texture (figure 30A) was found. This particle appears to have been deformed possibly by rapid loss of volatile components by heating. At some places the particle has roughly parallel rows of former cells. As for the previously described blocky particles, the preservation of this particle can be explained by the very short duration of the high temperature excursion. The surrounding matrix was melted, but probably cooled relatively quickly. Organic particles with cellular structure are more abundant in HW19-39d. Figure 30 B shows an organic carbon particle with roughly parallel rows of cell walls. Some rows are more regular and with cell spots which have been replaced by the Ca-rich matrix material. At some places the remains of the cell walls seem to have been expanded (figure 30 B). Garde et al (2020) interpreted expanded cell walls in Hiawatha lignite as results of heating with sudden release of volatiles.

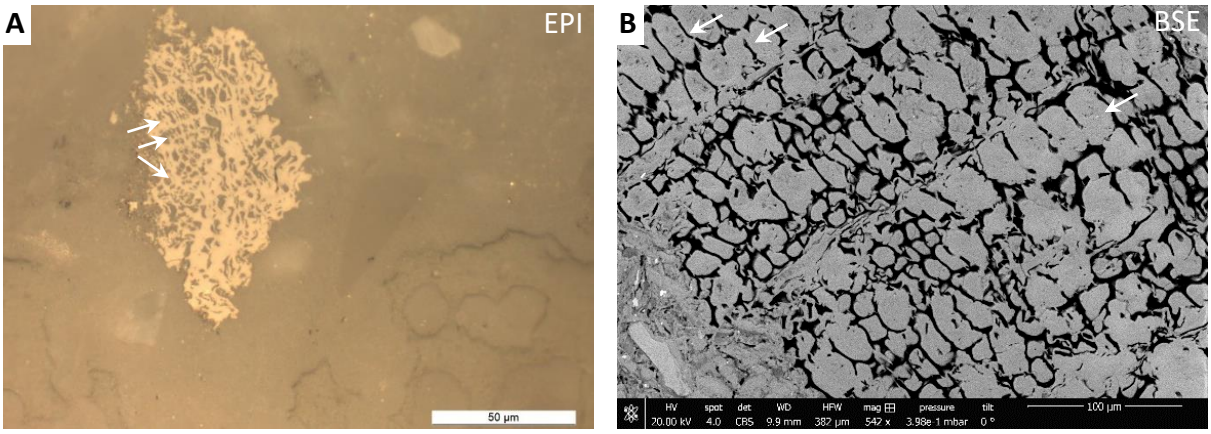


Figure 30. A) Sample HW19-32a. Organic particle with possible cell-wall texture. Arrows show indistinct deformed rows of former cells which are now filled with other matter. **B)** Sample HW19-39d. Organic particle with cell-wall texture. Cellular voids are filled with the Ca-rich matrix. Arrow shows regular rows of box-shaped former cells.

5. Carbonaceous vesicles

Multiple spherical and elliptical vesicles which have a relatively high carbon content are present in HW19-32a. Two different interpretations are suggested for these vesicles: 1) The carbonaceous matter could be derived from epoxy from the sample preparation. However, the few SEM-EDS measurements (appendix B9) of the carbonaceous matter did not show any chlorine peaks. 2) The vesicles could be devolatilization vesicles formed from organic matter which was trapped and degassed inside shocked-melted glass during the rapid heat-excursion. As an analogue for such a scenario, Howard et al (2013) described immiscible bubbles in impact glass linked to the 1.2-km-diameter Darwin crater in western Tasmania. The organic material that formed these bubbles experienced rapid heating and possibly degassing into spherical gas-melt froths, rich in volatiles and hydrocarbons (Howard et al., 2013). Examples of the vesicles in HW19-32a, are shown in figure 31A and B. In figure 31B, multiple vesicles are shown at the boundary between shock-melted glass and a fine-grained matrix. This sequence of vesicles probably represents a snapshot of different phases of the vesicles during the rapid temperature excursion and rapid subsequent cooling.

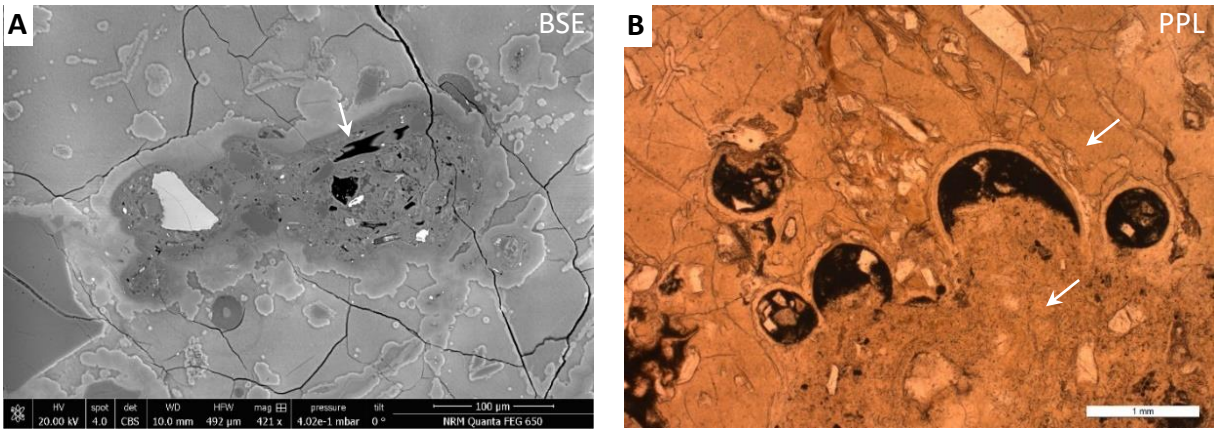


Figure 31. A) Sample HW19-32a. Vesicle containing carbonaceous matter and tiny mineral fragments. Arrow shows carbonaceous matter. **B)** Sample HW19-32a. Multiple carbonaceous vesicles. The carbonaceous material is dark-coloured. Upper arrow shows shock-melted glass. Lower arrow shows fine-grained matrix.

6.3.2 Reflectance measurements

In the samples HW19-32a and HW19-39d, it was shown by SEM-EDS analysis that some of the Ro measurements were indeed performed on organic carbon. In the other four HW19 samples it was shown by SEM-EDS that the Ro measurements were performed on other matter. In HW19-32a, five measurements of a confirmed organic carbon particle resulted in Ro = 2.25–2.88%. Two other possible carbonaceous particles in HW19-32a showed Ro = 4.60-6.11%. However, these two particles were not found during the SEM-EDS sessions, and thus it is unclear whether these particles are carbonaceous – and unlikely, as these are among the highest measurements obtained. The particle with Ro = 2.25-2.88 % (superimposed in figure 32B), shows inward concentric shrinkage cracks and lower Ro at its centre than at its rim. In figure 32A, a similar but larger organic carbon particle is shown, which notably shows higher reflectance in an almost separated part of its rim. The organic carbon particles in figure 32B, show that the reflectance of individual particles within the same sample is variable.

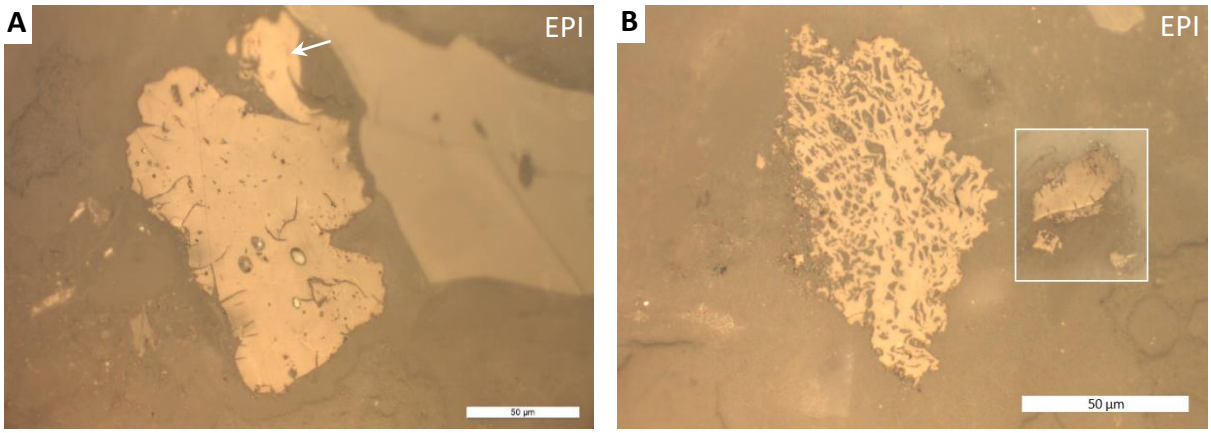


Figure 32. Organic carbon particles in sample HW19-32a **A)** The white arrow points to a section with higher Ro **B)** The previously described (in chapter 5.3.3) carbonaceous particle with possible conifer cellular texture, exhibits higher reflectance than the Ro-measured particle (Ro = 2.25–2.88%) under reflected light (same microscopical settings used for both microphotographs). The Ro-measured particle has been superimposed in a white square.

In HW19-39d, 97 Ro measurements of multiple carbonaceous particles, showed Ro values of 0.32%-1.93%. Two main populations of organic carbon were found, one with low Ro values of mainly 0.3%-0.5% and a second population with Ro values of ~1-2%. The population with lower reflectance is more abundant and comprised of more blocky carbon pieces, commonly with shrinkage cracks. The population with higher Ro commonly exhibits cellular textures. Figure 33A shows examples of particles from both populations adjacent to one another. In figure 33B, a microphotograph in ultraviolet light (UV) shows an organic particle from the population with low Ro values. Blue fluorescence is visible in cracks and voids in the carbon particle. The cracks and voids are presumably epoxy-filled, which yield blue fluorescence. There are no particles or parts consisting of organic C-H-O compounds, which would yield green fluorescence. This indicates that the organic compounds were C-H-O compounds were volatilized the during the impact event and only native carbon remained.

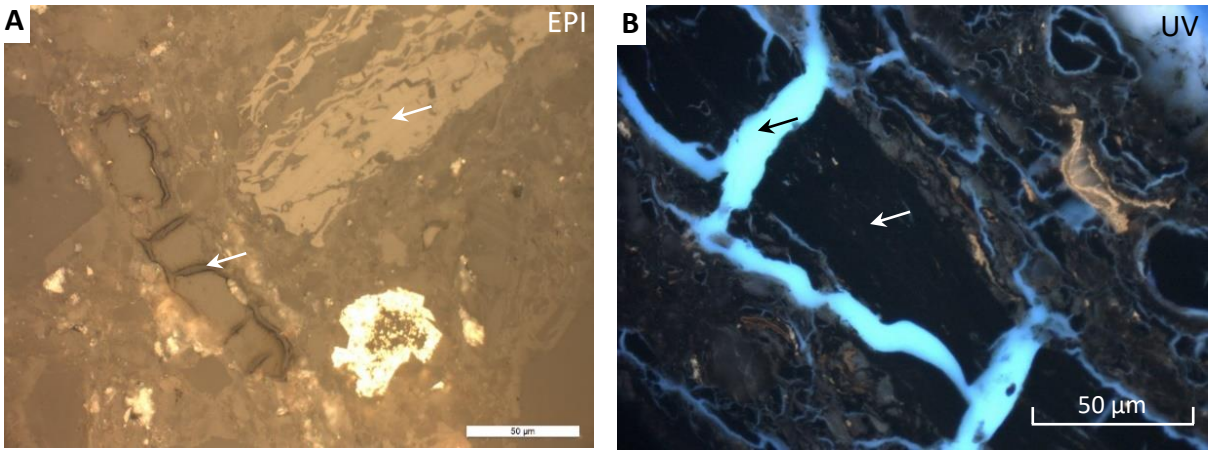


Figure 33 Sample HW19-39d **A)** Left arrow shows a blocky organic carbon particle with shrinkage cracks. Right arrow shows an organic carbon particle with higher reflectance indicated by its brighter colour under reflected light **B)** Close-up under ultra violet light of an organic particle from the low-Ro population. Black arrow shows presumed crack with epoxy. White arrow shows native carbon.

Braadbaart and Poole (2008) performed charcoalification experiments in order to calibrate Ro of wood subjected to domestic and industrial fires. Compared to these experiments, the Ro values of the organic carbon in HW19-32a and HW19-39d are relatively low, considering that the organic carbon is closely associated with shock-melted glass in HW19-32a and melted carbonate in HW19-39d. However, Braadbaart and Poole (2008) also showed that Ro is not only dependent on the temperature of the heating process, but also to the taxonomic identity of the wood and to the length of time of exposure to the heat source. For instance, pine that was heated up to 1200 °C in 60 minutes, had the Ro of ~6.5%.

The relatively low Ro shown by the organic carbon in HW19-32a and HW19-39d, could arguably have been produced by a non-impact process, such as a natural wildfire. The Ro values of HW19-32a and HW19-39d are within the range of the Ro of charcoal produced from four modern natural wildfires (McParland et al., 2009). However, HW19-32a could not have been formed by any other known process other than a hypervelocity impact, which is proven by the definite evidence for shock-metamorphism. It would be physically impossible for the organic carbon particles to be incorporated into the shock-melted glass after the hypervelocity impact. In HW19-39d, the Ca-rich matrix has replaced cellular voids in between the remaining cell walls, which shows that the organic particles could not have been incorporated into the microbreccia at a later point than the lithification of the matrix. To the best of the authors knowledge, no other process than a hypervelocity impact could have formed the microbreccia.

The variating Ro values of organic particles within the same sample, could arguable be explained by different taxonomic identities of the particles. Braadbaart and Poole (2008), showed that relatively greater energy input is required to increase Ro in conifer wood relative to less dense angiosperm wood, because the mass loss by expelled volatiles during breakdown, will be more constrained in conifer wood relative to the more open-structured angiosperm wood. However, the difference of Ro values between the angiosperm and conifer wood in Braadbaart and Poole (2008) were minor after the charcoalification experiments which lasted 15, 60 or 1440 min. Thus, the taxonomical identity of the organic matter which experienced the Hiawatha impact is not likely the cause of the Ro differences in the HW19 samples. Furthermore, the organic particles in the HW19 samples only show cellular texture typical for conifer species. The fact that the Ro values of the organic carbon particles in the two HW19 samples are relatively low compared to the experiments in Braadbaart and Poole (2008), together with the fact that organic matter with different Ro values are present in the same sample suggests two likely causes:

(i) Different Ro values between organic particles within the same sample indicate that the particles had different impact histories, and thus experienced different temperatures prior to settling and solidifying to a rock.

(ii) The high temperature excursion of the shocked organic carbon particles did not last long enough to reorganize into a graphite-like structure and the particles remained poorly ordered (A. Garde, personal communication).

Regarding (i): Garde et al (2020) collected lignite and charcoal at the tip of the Hiawatha Glacier and used this organic matter together with carbonaceous impactite grains from sample HW21-2016, to interpret the thermal degradation of the organic matter. Garde et al (2020) suggested that sand- and gravel-sized pieces of charcoal (Ro ≤ 3.5%) from sample HW21-2016, presumably document impact-induced incineration of surficial and/or originally shallowly buried plant material, whereas the lignite (Ro ~0.2%–0.5%), presumably from the same hypervelocity impact, indicates a distinct heating episode but not by direct incineration. Moreover, Garde et al (2020) suggested that a possible explanation for this could be that the lower Ro particles were protected by the GrIS with associated permafrost in the target rocks during the hypervelocity impact. The same scenario is suggested in this study, which is supported by the two Ro-populations of organic carbon particles in HW19-39d.

Regarding (ii): This seems likely considering the nature of the huge and instantaneous energy input from the hypervelocity impact, which left behind a 31-km-wide impact crater. The instantaneous thermally degraded organic carbon probably lost most volatiles and where and was fixed in place as native carbon during subsequent cooling. Lindgren et al (2006), ascribed the survival of biological signatures in carbonate melt breccias, despite high temperatures of 600 °C or more, to a relatively short period of time for which the clasts were exposed to high temperatures 600 °C or more. Moreover, Losiak et al (2016, 2019) reported low-reflecting charcoal intermixed with ejecta from the Kaali crater in Estonia but did not make conclusions from this observation.

The most influential factors for the Ro values of the organic carbon in the HW19-impactites are likely the temperature that the organic carbon experienced, along with the assumed short duration of the high-temperature excursion. The plotted Ro measurements in figure 34 shows that the difference of the Ro values between the HW19 samples of different shock level is relatively low. The relatively low Ro values of the organic carbon particles in HW19-32a and HW19-39d, considering the nature of a high-temperature hypervelocity impact event, are probably due a short duration of the high-temperature excursion.

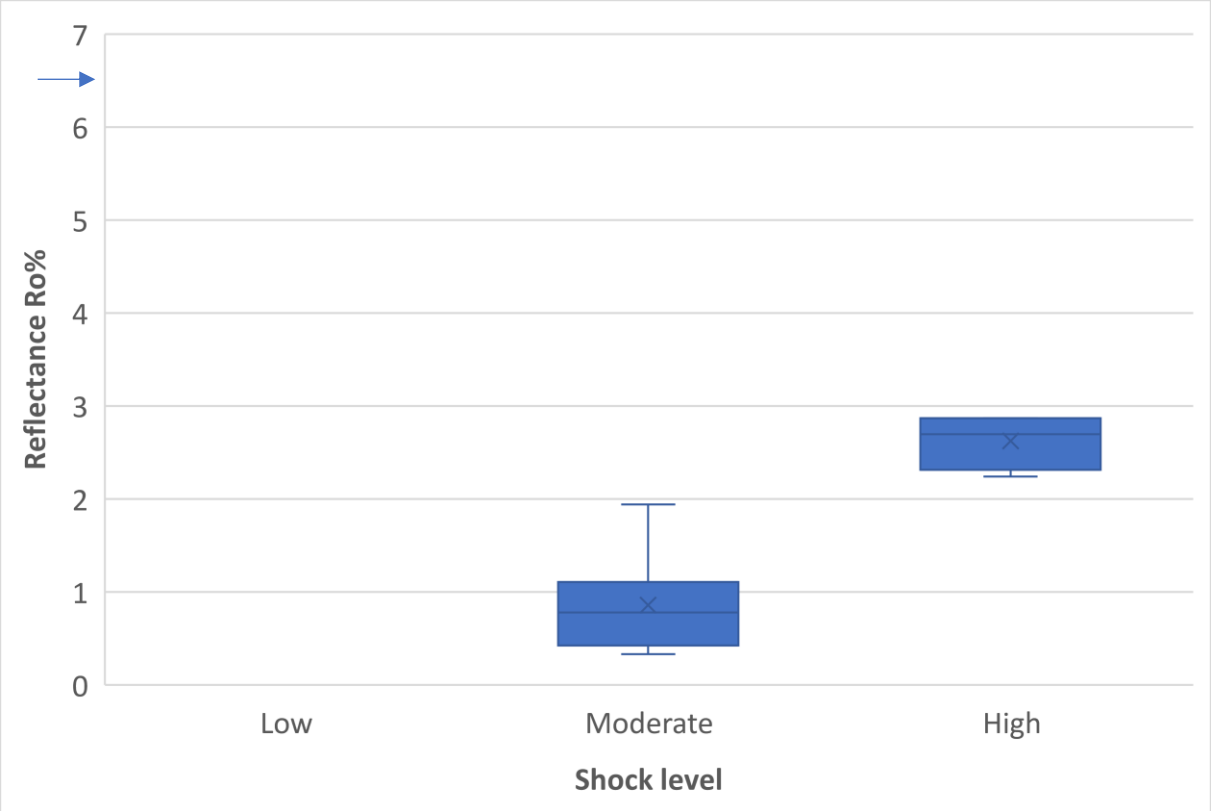


Figure 34. Box plot of the Ro measurements of organic particles in the samples HW19-32a (high shock level) and HW19-39d (moderate shock level) relative to the estimated shock level of these impactites. The data for HW19-32a (right box) is the same data as in the histogram in figure 26C. The data for HW19-39d (left box) is the same data as in the histogram in figure 22A. Arrow pointing at Ro 6.5% indicate the Ro of unshocked pine heated up to 1200 °C in 60 minutes during the charcoalification experiments reported in Braadbaart and Poole (2008).

6.3.3 Source of the organic carbon

Organic carbon is known to be strongly disordered in impactites from hypervelocity impact events (Garde et al, 2020; Parnell and Lindgren, 2006). By Raman spectroscopy, Garde et al (2020) showed that the organic carbon in the impactite grains from HW21-2016 is poorly ordered, and thus could not have been derived from well-crystallized metamorphic graphite in the crystalline bedrock in the target area. Such measurements could also be performed in the HW19-impactites in this study. However, the organic carbon pieces in the HW19-impactites with cellular textures, are obviously not derived from graphite.

Garde et al (2020) showed that carbon modified from the Hiawatha impact come from conifer trees. This is consistent with the organic carbon particles with cellular texture HW19-39d and possibly in HW19-32a. The previously described particle in HW19-32a (figure 30A) have indistinct regular rows of former cells and could therefore be conifer wood. Figure 35 A shows a transverse cross-sectioned particle from HW19-39d. In the upper part of the rows of cell walls are regular and have largely even-sized box-shapes, which is diagnostic for coniferous wood (Hoadley, 1990). A more compact section of the particle is shown in figure 35A, which could testify to a seasonal growth change of the wood. In figure 35B a longitudinal section of a similar particle from HW19-39d is shown. The arrow in figure 35B show what is interpreted to be a uniseriate ray structure, which is characteristic for coniferous wood (Hoadley, 1990).

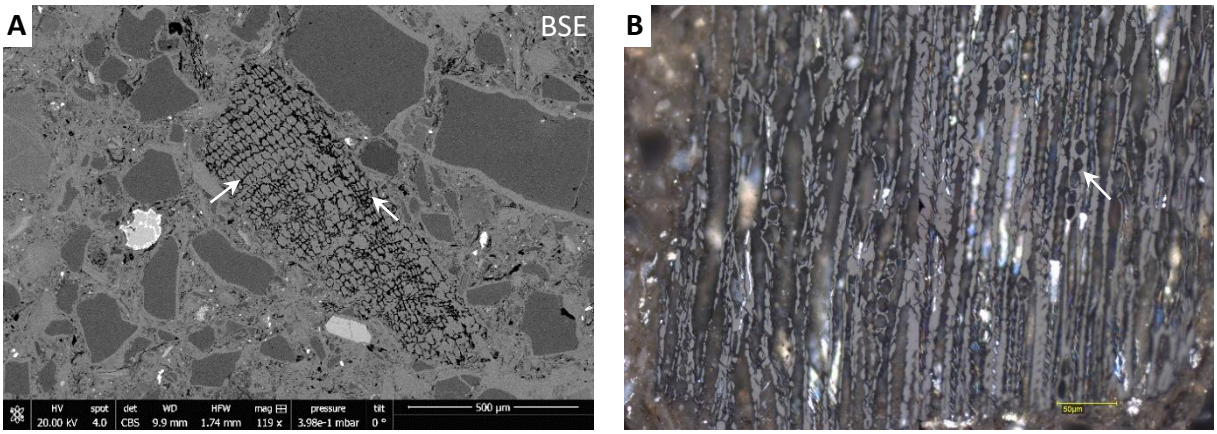


Figure 35. A. Sample HW19-39d. Transverse cross-sectioned particle from HW19-39d**.** Left arrow shows a regular row of largely even-sized box-shaped former cells. Right arrow points at a more compact section of the particle. **B.** Sample HW19-39d. Arrow shows possible uniseriate ray structure.

Some of the particles in carbon group 2 (table 6), is interpreted as devolatilized and shrunken. In figure 36A, a soft and unshocked sand-sized grain is shown from sample HW21-2016. The grain consists of layered fine-grained clay and organic matter and could stem from the potential source of the transformed carbonaceous particles (A. Garde, personal communication). In figure 36B, a close-up of the particle in figure 28A is shown. The particle seems to have layer-texture in a N-S direction. The black surrounding material is fractures filled with epoxy.

In summary, the findings in this investigation support the conclusion in Garde et al (2020) that the organic carbon which was modified from the Hiawatha impact, stems from local, conifer trees with a probable late Pliocene to early Pleistocene age of ca. 3–2.4 Ma. The source was likely an unmetamorphosed surficial deposit, which contained dead conifer tree trunks. It might also have contained fine-grained layered clay and organic matter, similar to material in the grain in figure 36A. There could also have been multiple unrelated deposits affected by the Hiawatha impact. The grain in figure 36A indicate that there are still local unmetamorphosed surficial deposits beneath the GrIS. Perhaps this gives us a clue as to what is buried under more of the GrIS?

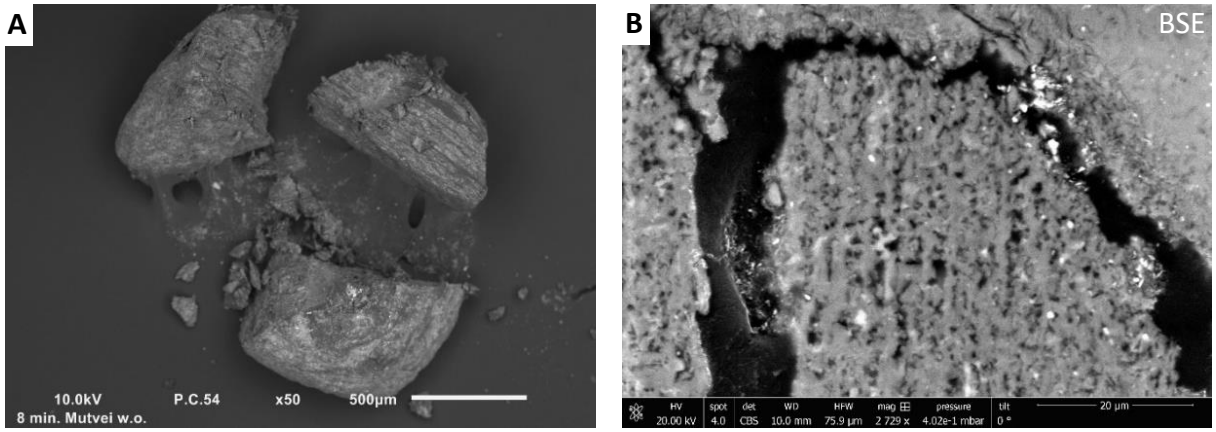


Figure 36. A) Raman photo of an unmetamorphosed sand grain from HW21-2016 (courtesy of Adam Garde). **B)** Carbonaceous particle from sample HW19-02a (appendix B5).

7. Conclusions

The first objective in this thesis was to investigate the possible link between the Cape York meteorites and the Hiawatha impact crater. By various heavy mineral separation techniques and a subsequent AQM analysis, it was shown that none of the 123 separated heavy mineral grains from the glaciofluvial sand sample HW21-2016 were chromite. Since no chromite grains were found, the possible link between the Cape York meteorites and the Hiawatha impact crater could not be tested by comparing chromium isotope ratios. Based upon the apparent absence of chromite in the examined HW21-2016 subsample, the chromium and siderophile anomalies in HW21-2016, which were reported by Kjær et al (2018), are now very unlikely to stem from a hidden terrestrial chromitite deposit. The apparent absence of chromite in the HW21-2016 subsample in this study corroborates the significance of the PGE spectra in Kjær et al (2018), which points to a strongly fractionated iron meteorite.

The second objective was to investigate a possible Younger Dryas age for the Hiawatha impact crater. The petrographic examination of 389 marine sand-sized grains, which were deposited in the northernmost Baffin Bay around the Younger Dryas, revealed that none of these grains show any evidence of being related to the Hiawatha impact. With the absence of ejecta and impactite grains in the investigated marine sediment, a Younger Dryas age for the Hiawatha impact crater is now less likely. However, based upon the very diluted HW21-2016 sample with respect to impactites, potential Hiawatha grains in the investigated marine sediment would also most likely be very diluted by other matter. Even though no ejecta or impactites grains were found, the possibility of a Younger Dryas age of the Hiawatha impact crater remains open.

The third objective was to contribute to an ongoing assessment of the origin and nature of the highly unusual carbon component in the Hiawatha impact crater. The petrological examination of six impactite samples from the Hiawatha impact crater showed that five of these samples contain carbonaceous matter. Some of the carbonaceous material is clearly organic carbon which experienced the hypervelocity impact. The organic carbon particles in the impactites with definite evidence for meteorite impact origin, exclude the possibility that the thermal degradation of the organic carbon in these impactites was caused by any other process than a hypervelocity impact event. At least one of the impactites, possibly two, contain organic carbon particles with conifer cellular textures. By the close association with diagnostic shock metamorphism, these particles corroborate the conclusion by Garde et al (2020) that organic carbon that experienced the Hiawatha impact stems from local, thermally degraded conifer trees with a probable age of ca. 3–2.4 Ma. Vitrinite reflectance measurements of organic carbon particles in two of the examined impactites showed relatively low Ro values compared to Ro values from charcoalification experiments of wood. These relatively low Ro values seem to be related to the short duration of the high-temperature excursion during the hypervelocity impact event. The Ro values seem to increase with higher degree of shock metamorphism, which probably is related to higher post-shock temperature. Different Ro values between organic particles within the same sample indicate that the particles had different impact histories prior to settling and solidifying to a rock.

Acknowledgements

I would like to thank my MSc Project supervisor Prof. Kurt Kjær of the Globe Institute at the University of Copenhagen for giving me the opportunity to work with the Hiawatha research and for his guidance and support during the project. I would like to thank my MSc Project supervisor Dr Joakim Mansfeld of the Department of Geological Sciences at Stockholm University for his expertise and feedback during the project and during courses at Stockholm University. I would also like to thank: Prof. Nicolaj Larsen of the Globe Institute at the University of Copenhagen for his guidance, feedback and for helping me structure the thesis work; Dr Adam Garde of the Geological Survey of Denmark and Greenland. Adam's expertise and guidance has been absolutely essential for me throughout the entire MSc project; Dr Henning Haack for introducing me to the Hiawatha research by a presentation at a conference in Estonia 2017; Peter Ilsøe for helping me in the rock cutting lab and for our numerous interesting discussions during the project; Numerous personnel in various labs at Aarhus University, the Centre for Star and Planet Formation, the Department of Geosciences at Swedish Museum of Natural History, the Geological Survey of Denmark and Greenland, the Globe Institute and Stockholm University; All personnel at Stockholm University and the University of Copenhagen who made this MSc Project possible via an Erasmus+ Traineeship; The Quarternary Group and all other people at the Globe Institute who made me feel very welcome. Finally, I would like to thank family and friends for all your support.

References

Appelt, M., Jensen, J. F., Mikkel, M., Henning, H., Mikkel, S., and Taube, M. (2015). THE CULTURAL HISTORY OF THE INNAANGANEQ/CAPE YORK METEORITE: TECHNICAL REPORT 2015. In Cultural History of the Innaanganeq/Cape York Meteorite, Technical Report 2015.

Bennike, O. (2000). Notes on the late Cenozoic history of the Washington Land area, western North Greenland. GEUS Bulletin, 29-34.

Blake, W., Jr. Jackson, H. R. & Currie, C. G. (1996). Seafloor evidence for glaciation, northernmost Baffin Bay. Bulletin of the Geological Society of Denmark, Vol. 43, pp. 157-168.

Braadbaart, F., & Poole, I. (2008). Morphological, chemical and physical changes during charcoalification of wood and its relevance to archaeological contexts. Journal of archaeological science, 35(9), 2434-2445.

Brantley, S. L. (1992). The effect of fluid chemistry on quartz microcrack lifetimes. Earth and Planetary Science Letters, 113(1-2), 145-156.

Buchwald, V. F. (1975). Handbook of iron meteorites. Their history, distribution, composition and structure. himt.

Buchwald, V. F. (1985). Meteoritic iron, telluric iron and wrought iron in Greenland (Vol. 9). Museum Tusculanum Press.

Burnham, A. K., & Sweeney, J. J. (1989). A chemical kinetic model of vitrinite maturation and reflectance. Geochimica et Cosmochimica Acta, 53(10), 2649-2657.

Cavosie, A. J., Timms, N. E., Erickson, T. M., Hagerty, J. J., & Hörz, F. (2016). Transformations to granular zircon revealed: Twinning, reidite, and ZrO2 in shocked zircon from Meteor Crater (Arizona, USA). Geology, 44(9), 703-706.

Dawes, P. R. (2004). Explanatory notes to the geological map of Greenland, 1: 500 000, Humboldt Gletscher, Sheet 6. Geological Survey of Denmark and Greenland (GEUS) Bulletin, 1-48.

England, J., Atkinson, N., Bednarski, J., Dyke, A. S., Hodgson, D. A., & Cofaigh, C. Ó. (2006). The Innuitian Ice Sheet: configuration, dynamics and chronology. Quaternary Science Reviews, 25(7-8), 689-703.

Esbensen, K. H., & Buchwald, V. F. (1982). Planet (oid) core crystallisation and fractionation—evidence from the Agpalilik mass of the Cape York iron meteorite shower. Physics of the Earth and Planetary Interiors, 29(3-4), 218-232.

Esbensen, K. H., Buchwald, V. F., Malvin, D. J., & Wasson, J. T. (1982). Systematic compositional variations in the Cape York iron meteorite. *Geochimica et Cosmochimica Acta*, *46*(10), 1913-1920.

French, B. M. (1998). Traces of catastrophe: A handbook of shock-metamorphic effects in terrestrial meteorite impact structures. Lunar and Planetary Institute.

French, B. M., & Koeberl, C. (2010). The convincing identification of terrestrial meteorite impact structures: What works, what doesn't, and why. Earth-Science Reviews, 98(1-2), 123-170.

Funder, S, Bennike, O., Böcher, J., Israelson, C., Petersen, K.S. & Símonarson, L. A. 2001–11–24: Late Pliocene Greenland – The Kap København Formation in North Greenland. Bulletin of the Geological Society of Denmark, Vol. 48, pp. 117–134.

Fyles, J. G., Marincovich Jr, L., Matthews Jr, J. V., & Barendregt, R. (1991). Unique mollusc find in the beaufort formation (Pliocene) on Meighen Island, Arctic Canada. Current Research, Part B, Geological Survey of Canada, Paper, 91, 105-112.

Garde, A. A., McDonald, I., Dyck, B., & Keulen, N. (2012). Searching for giant, ancient impact structures on Earth: the Mesoarchaean Maniitsoq structure, West Greenland. Earth and Planetary Science Letters, 337, 197-210.

Garde, A. A., Søndergaard, A. S., Guvad, C., Dahl-Møller, J., Nehrke, G., Sanei, H., ... & Larsen, N. K. (2020). Pleistocene organic matter modified by the Hiawatha impact, northwest Greenland. Geology.

Gilmour, I., French, B. M., Franchi, I. A., Abbott, J. I., Hough, R. M., Newton, J., & Koeberl, C. (2003). Geochemistry of carbonaceous impactites from the Gardnos impact structure, Norway. Geochimica et Cosmochimica Acta, 67(20), 3889-3903.

Gulick, S. P., Bralower, T. J., Ormö, J., Hall, B., Grice, K., Schaefer, B., ... & Kaskes, P. (2019). The first day of the Cenozoic. Proceedings of the National Academy of Sciences, 116(39), 19342-19351.

Haack, H., Jørgensen, U. G., Andersen, A., Bizzarro, M., & Buchwald, V. F. (2006). Solsystemet-fra altings oprindelse til livets opståen. Geoviden, (3), 2-19.

Hoadley, R.B., 1990, Identifying Wood: Accurate Results with Simple Tools: Newton, Connecticut, Taunton Press, Inc., 223 p.

Howard, K. T., Bailey, M. J., Berhanu, D., Bland, P. A., Cressey, G., Howard, L. E., ... & Stolojan, V. (2013). Biomass preservation in impact melt ejecta. Nature Geoscience, 6(12), 1018-1022.

Kelly, M., Funder, S., Houmark-Nielsen, M., Knudsen, K. L., Kronborg, C., Landvik, J., & Sorby, L. (1999). Quaternary glacial and marine environmental history of northwest Greenland: a review and reappraisal. Quaternary Science Reviews, 18(3), 373-392.

Keulen, N., Malkki, S. N., & Graham, S. (2020). Automated Quantitative Mineralogy Applied to Metamorphic Rocks. Minerals, 10(1), 47.

Kjær, K. H., Larsen, N. K., Binder, T., Bjørk, A. A., Eisen, O., Fahnestock, M. A., ... and Houmark-Nielsen, M. (2018). A large impact crater beneath Hiawatha Glacier in northwest Greenland. Science advances, 4(11), eaar8173.

Knudsen, K. L., Stabell, B., SEIDENKRANTZ, M. S., Eiriksson, J., & Blake Jr, W. (2008). Deglacial and Holocene conditions in northernmost Baffin Bay: sediments, foraminifera, diatoms and stable isotopes. Boreas, 37(3), 346-376.

Koeberl, C., Shukolyukov, A., & Lugmair, G. W. (2007). Chromium isotopic studies of terrestrial impact craters: Identification of meteoritic components at Bosumtwi, Clearwater East, Lappajärvi, and Rochechouart. Earth and Planetary Science Letters, 256(3-4), 534-546.

Lindgren, P., Parnell, J., Bowden, S., Taylor, C., Osinski, G. R., & Lee, P. (2006). PRESERVATION OF BIOLOGICAL SIGNATURE WITHIN IMPACT MELT BRECCIAS: HAUGHTON IMPACT STRUCTURE. In 37th Lunar and Planetary Science Conference (Vol. 1028).

Losiak, A., Wild, E. M., Geppert, W. D., Huber, M. S., Jõeleht, A., Kriiska, A., ... & Steier, P. (2016). Dating a small impact crater: An age of Kaali crater (Estonia) based on charcoal emplaced within proximal ejecta. Meteoritics & Planetary Science, 51(4), 681-695.

Losiak, A., Belcher, C., Jõeleht, A., Plado, J., & Szyszko, M. (2019). Death from Space: Origin of Charcoal Found in Proximal Ejecta Blanket of Kaali Craters (Is NOT What We Think). LPI, (2132), 2406.

Lugmair, G. W., & Shukolyukov, A. (1998). Early solar system timescales according to 53Mn-53Cr systematics. Geochimica et Cosmochimica Acta, 62(16), 2863-2886.

MacGregor, J. A., Bottke Jr, W. F., Fahnestock, M. A., Harbeck, J. P., Kjær, K. H., Paden, J. D., ... & Studinger, M. (2019). A possible second large subglacial impact crater in northwest Greenland. Geophysical Research Letters, 46(3), 1496-1504.

McParland, L. C., Collinson, M. E., Scott, A. C., & Campbell, G. (2009). The use of reflectance values for the interpretation of natural and anthropogenic charcoal assemblages. Archaeological and Anthropological Sciences, 1(4), 249.

Moore, A. M., Kennett, J. P., Napier, W. M., Bunch, T. E., Weaver, J. C., LeCompte, M., ... & Wittke, J. H. (2020). evidence of cosmic impact at Abu Hureyra, Syria at the YD Onset (~ 12.8 ka): High-temperature melting at> 2200 C. Scientific reports, 10(1), 1-22.

Ormö, J., Rossi, A. P., & Housen, K. R. (2013). A new method to determine the direction of impact: Asymmetry of concentric impact craters as observed in the field (Lockne), on Mars, in experiments, and simulations. Meteoritics & Planetary Science, 48(3), 403-419.

Osinski, G. R., & Spray, J. G. (2001). Impact-generated carbonate melts: evidence from the Haughton structure, Canada. Earth and Planetary Science Letters, 194(1-2), 17-29.

Osinski, G. R. (2003). Impact glasses in fallout suevites from the Ries impact structure, Germany: An analytical SEM study. Meteoritics & Planetary Science, 38(11), 1641-1667.

Parnell, J., & Lindgren, P. (2006). The processing of organic matter in impact craters: implications for the exploration for life. 40th ESLAB Proceedings, Noordwijk, The Netherlands: European Space Agency, 147-152.

Parnell, J., Bowden, S. A., Osinski, G. R., Lee, P., Green, P., Taylor, C., & Baron, M. (2007). Organic geochemistry of impactites from the Haughton impact structure, Devon Island, Nunavut, Canada. Geochimica et Cosmochimica Acta, 71(7), 1800-1819.

Senft, L. E., & Stewart, S. T. (2008). Impact crater formation in icy layered terrains on Mars. Meteoritics & Planetary Science, 43(12), 1993-2013.

Short, N. M. (1970). Progressive shock metamorphism of quartzite ejecta from the Sedan nuclear explosion crater. The Journal of Geology, 78(6), 705-732.

Schultz, P. H., Harris, R. S., Clemett, S. J., Thomas-Keprta, K. L., & Zárate, M. (2014). Preserved flora and organics in impact melt breccias. Geology, 42(6), 515-518.

Shuvalov, V. (2011). Ejecta deposition after oblique impacts: An influence of impact scale. Meteoritics & Planetary Science, 46(11), 1713-1718.

Stöffler, D., & Langenhorst, F. (1994). Shock metamorphism of quartz in nature and experiment: I. Basic observation and theory. Meteoritics, 29(2), 155-181.

Stöffler, D., Hamann, C., & Metzler, K. (2018). Shock metamorphism of planetary silicate rocks and sediments: Proposal for an updated classification system. Meteoritics & Planetary Science, 53(1), 5-49.

Wittmann, A., Kenkmann, T., Schmitt, R. T., & Stöffler, D. (2006). Shock-metamorphosed zircon in terrestrial impact craters. Meteoritics & Planetary Science, 41(3), 433-454.

Appendix A. Macroscopic impactite data

Appendix A1. HW19 impactites

Table 7. Coordinates of sample sites and tentative sample groups based upon shock-level.

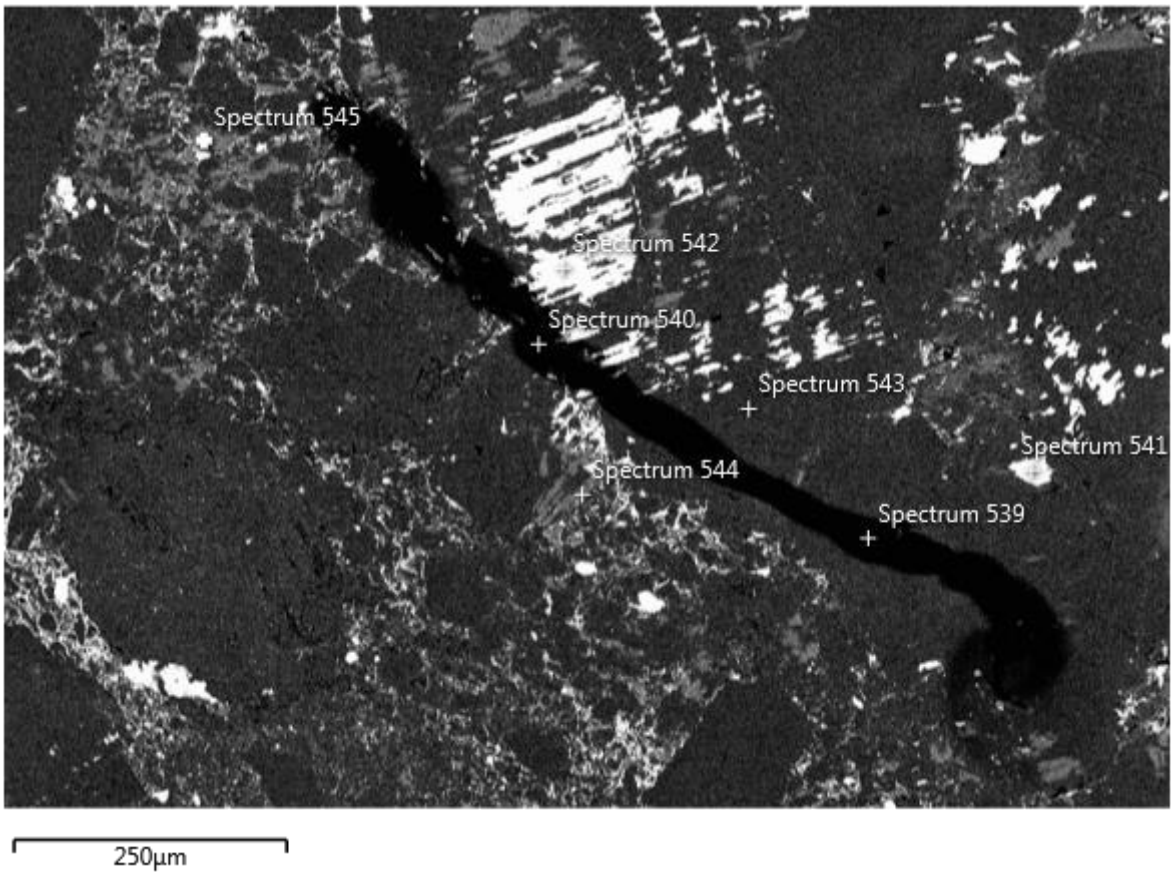
Sample	Site	coor_y	coor_x
LOW SHOCK-LEVEL			
HW19-07	HW19-C	78,5892	-66,8157
HW19-14	HW19-C	78,5892	-66,8157
HW19-16	HW19-C	78,5892	-66,8157
HW19-19	HW19-C	78,5892	-66,8157
HW19-22	HW19-C	78,5892	-66,8157
HW19-35	HW19-B	78,6671	-66,9799
HW19-40	HW19-B	78,6671	-66,9799
MODERATE SHOCK-LEVEL			
HW19-23	HW19-C	78,5892	-66,8157
HW19-24	HW19-C	78,5892	-66,8157
HW19-39	HW19-B	78,6671	-66,9799
HIGH SHOCK-LEVEL			
HW19-02	HW19-A	78,8417	-67,2941
HW19-03	HW19-A	78,8417	-67,2941
HW19-06	HW19-A	78,8417	-67,2941
HW19-17	HW19-C	78,5892	-66,8157
HW19-32	HW19-B	78,6671	-66,9799



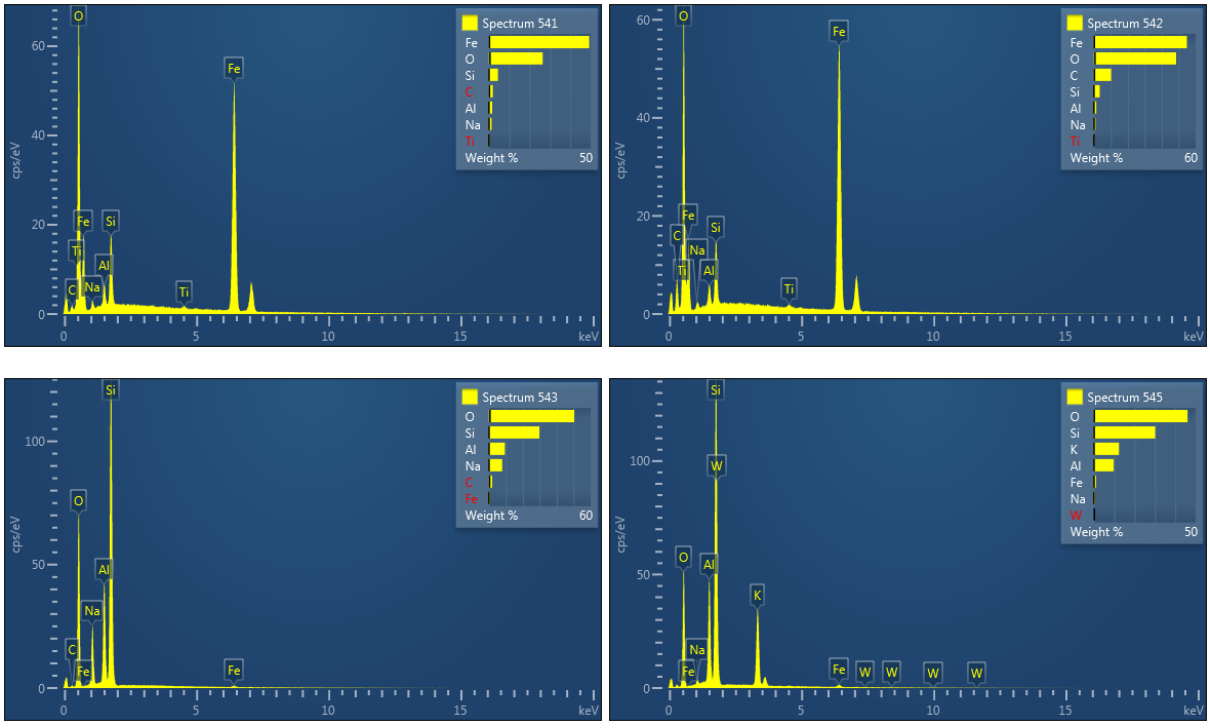
15 rock chips divided into tentative groups based upon their shock-level. The uppermost two rows are interpreted as low shock-level impactites, The third row as medium shock-level impactites and the lowermost row as high shock-level impactites.

Appendix B. Microscopic impactite data

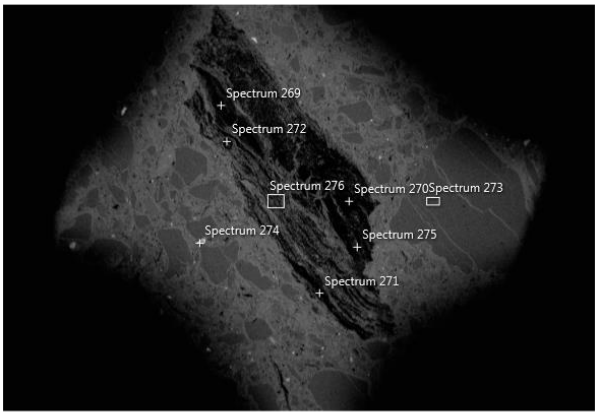
B1. HW19-07a.

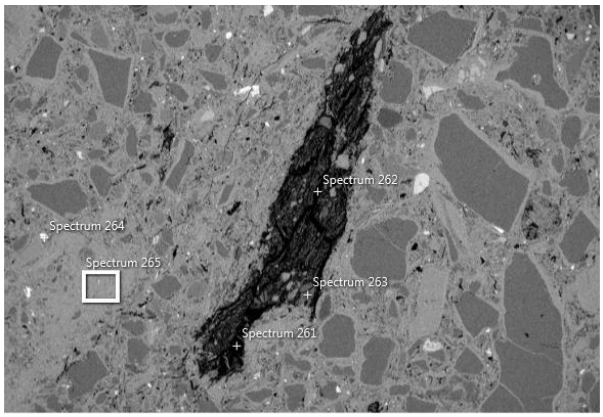


Spectrum 542 shows that carbon and Fe along the cleavage plain of felspar. The black material is a fibre.



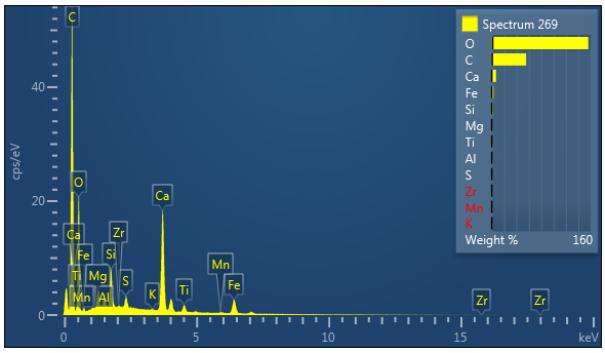
B2. HW19-39d

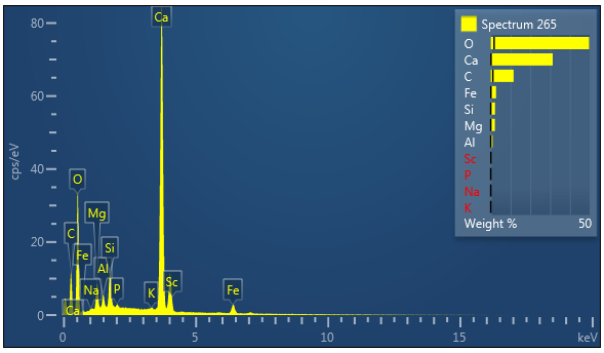


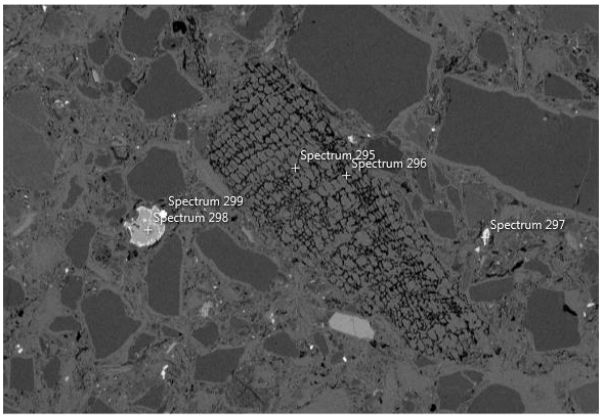


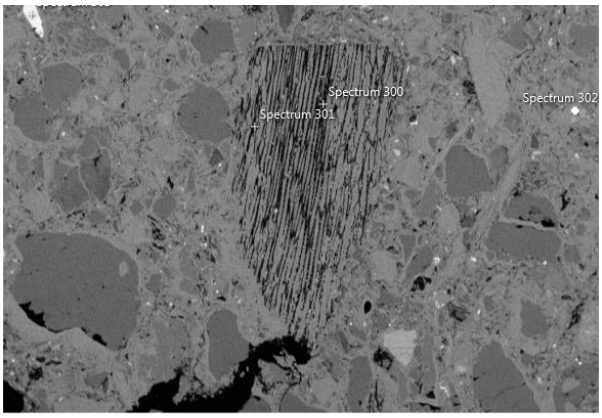
2.5mm

1mm



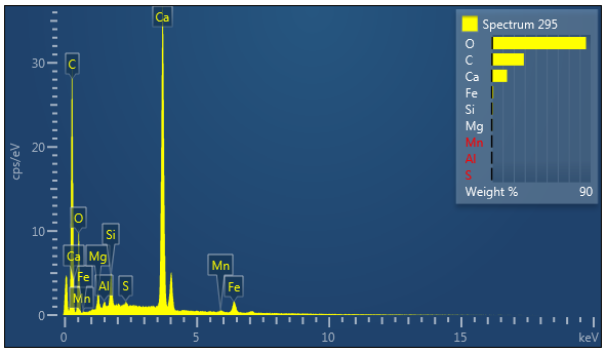


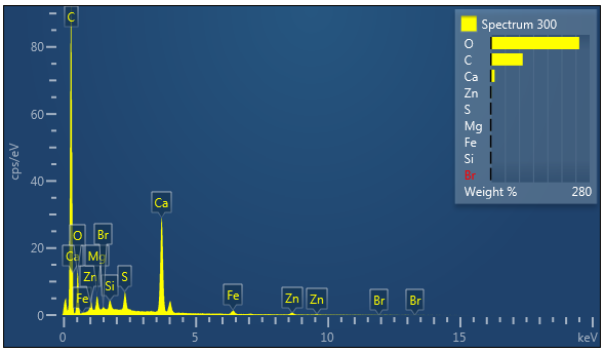




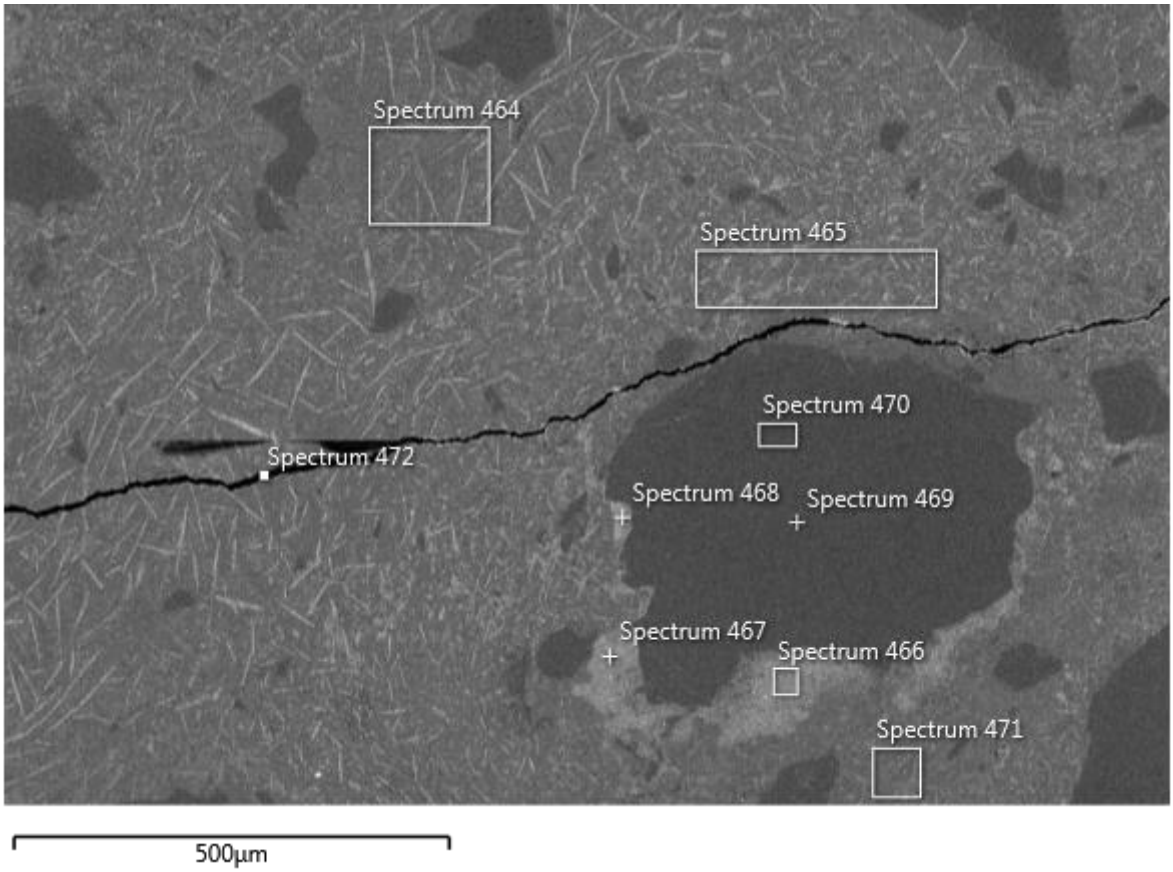
500µm

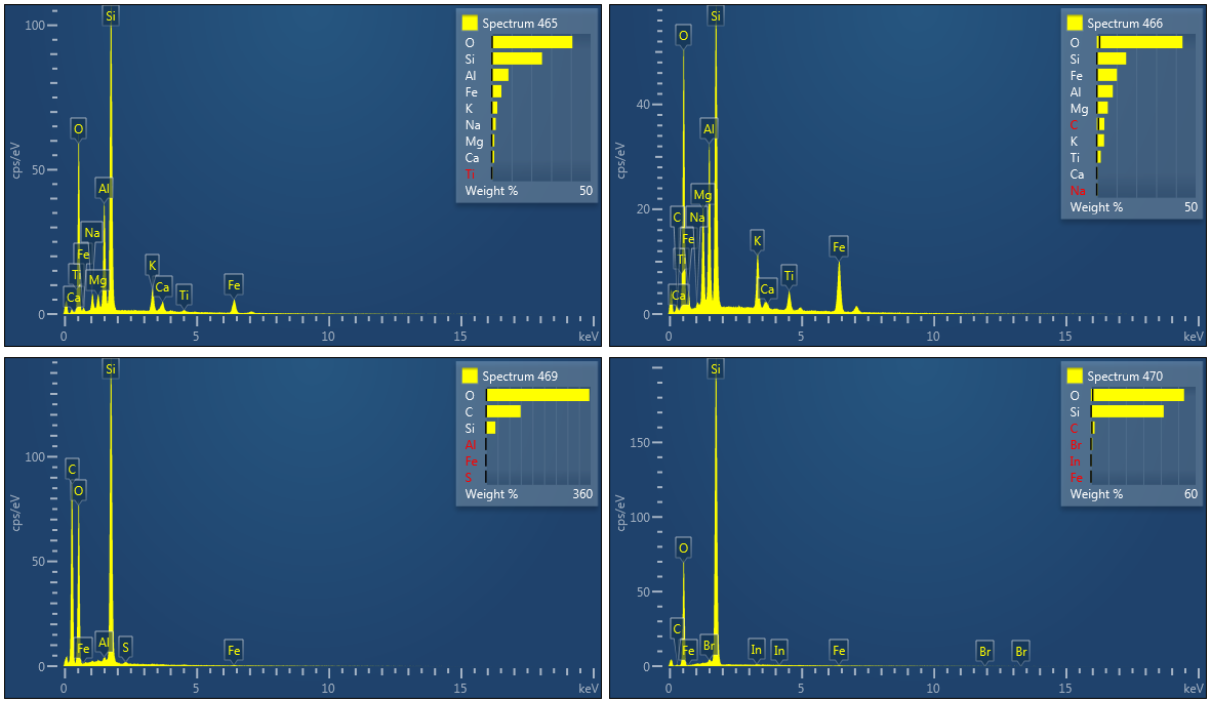
500µm



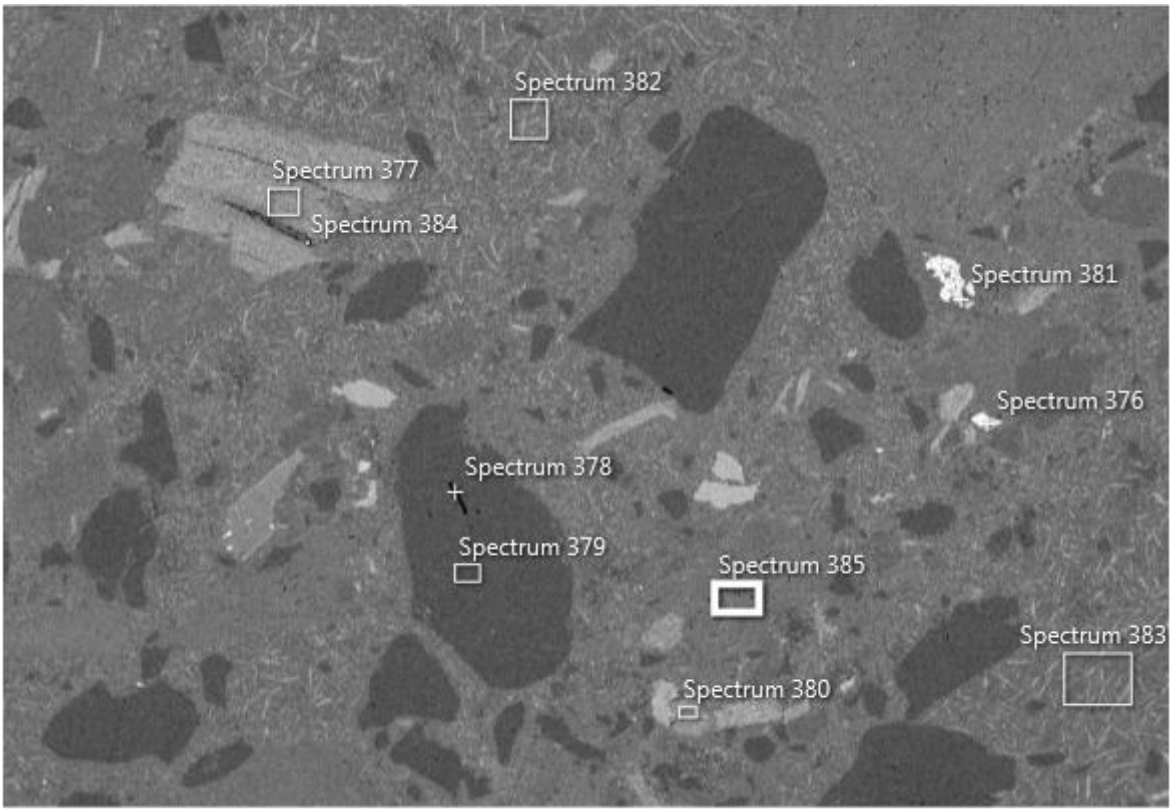


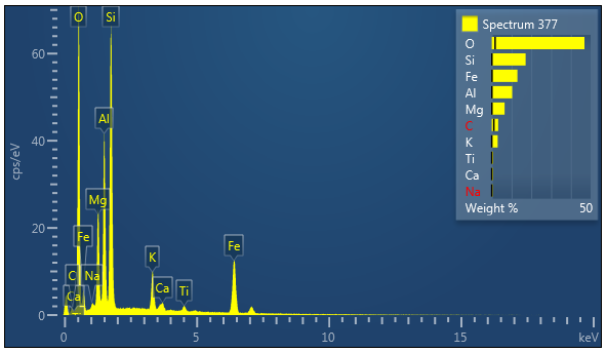
B3. HW19-02a

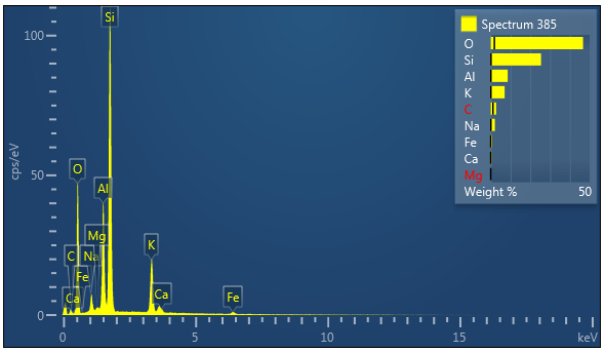

Spectrum 464
Spectrum 465
Spectrum 470
Spectrum 472
Spectrum 468
Spectrum 469
Spectrum 467
Spectrum 466
Spectrum 471
500µm


Spectrum 465
Spectrum 466
Spectrum 469
Spectrum 470
cps/eV
keV
Weight %

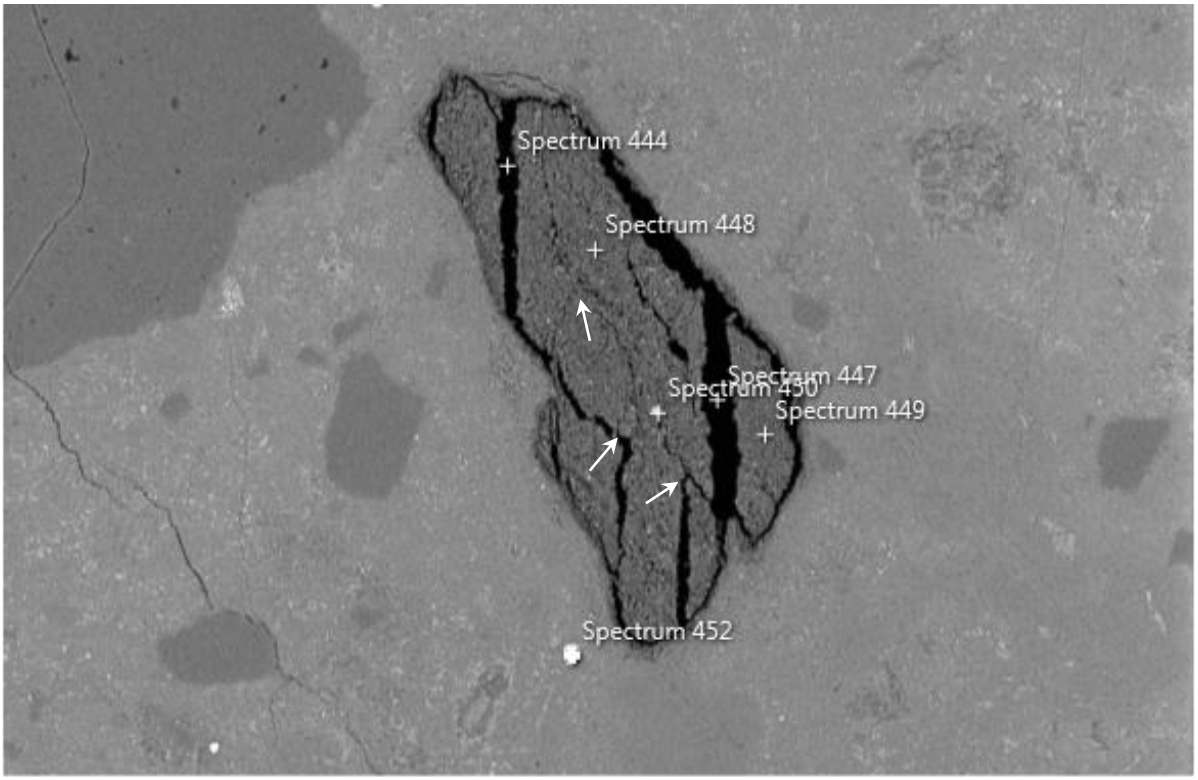
B4. HW19-02a

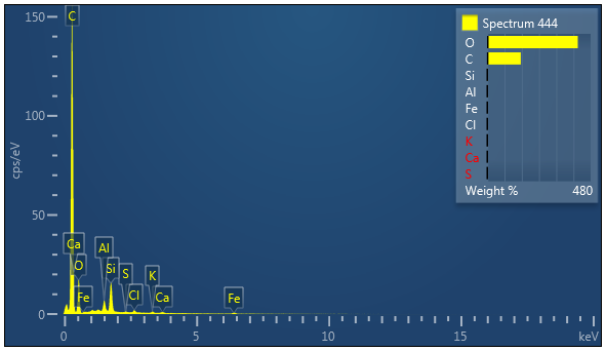

Spectrum 382
Spectrum 377
Spectrum 384
Spectrum 381
Spectrum 376
Spectrum 378
Spectrum 379
Spectrum 385
Spectrum 383
Spectrum 380
500µm

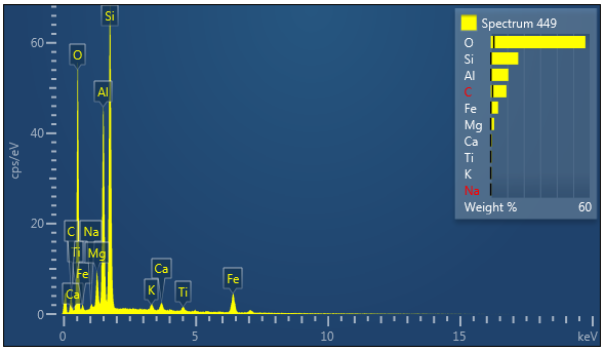

Spectrum 377
O
Si
Fe
Al
Mg
C
K
Ti
Ca
Na
Weight %
50
cps/eV
keV

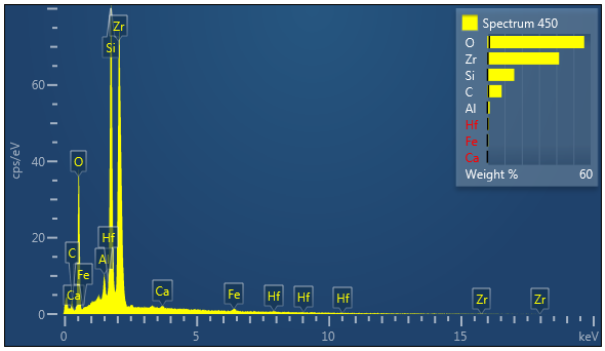

Spectrum 385
O
Si
Al
K
C
Na
Fe
Ca
Mg
Weight %
50
cps/eV
keV

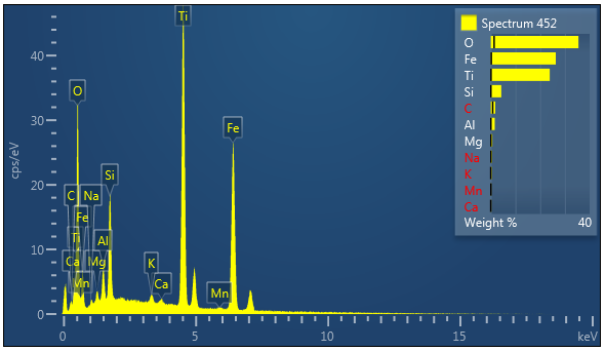
B5. HW19-02a


Spectrum 444
Spectrum 448
Spectrum 447
Spectrum 450
Spectrum 449
Spectrum 452
250µm

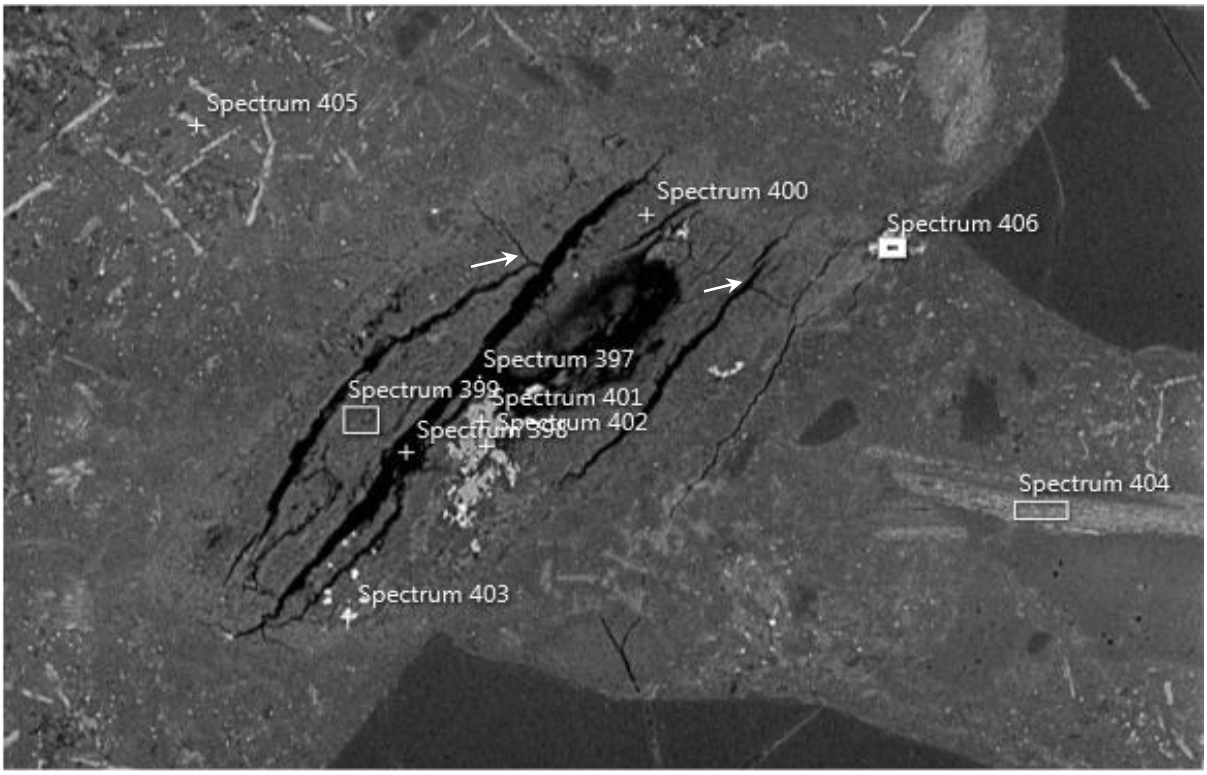

Spectrum 444
O
C
Si
Al
Fe
Cl
K
Ca
S
Weight %
480
cps/eV
keV

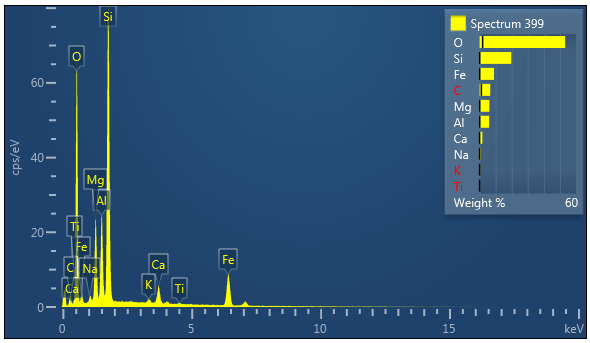

Spectrum 449
O
Si
Al
C
Fe
Mg
Ca
Ti
K
Na
Weight %
60
cps/eV
keV

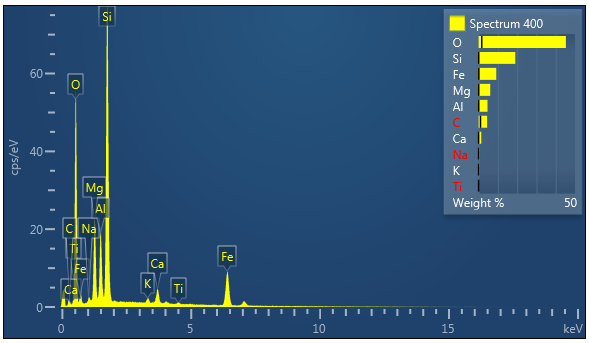

Spectrum 450
O
Zr
Si
C
Al
Hf
Fe
Ca
Weight %
60
cps/eV
keV


Spectrum 452
O
Fe
Ti
Si
C
Al
Mg
Na
K
Mn
Ca
Weight %
40
cps/eV
keV

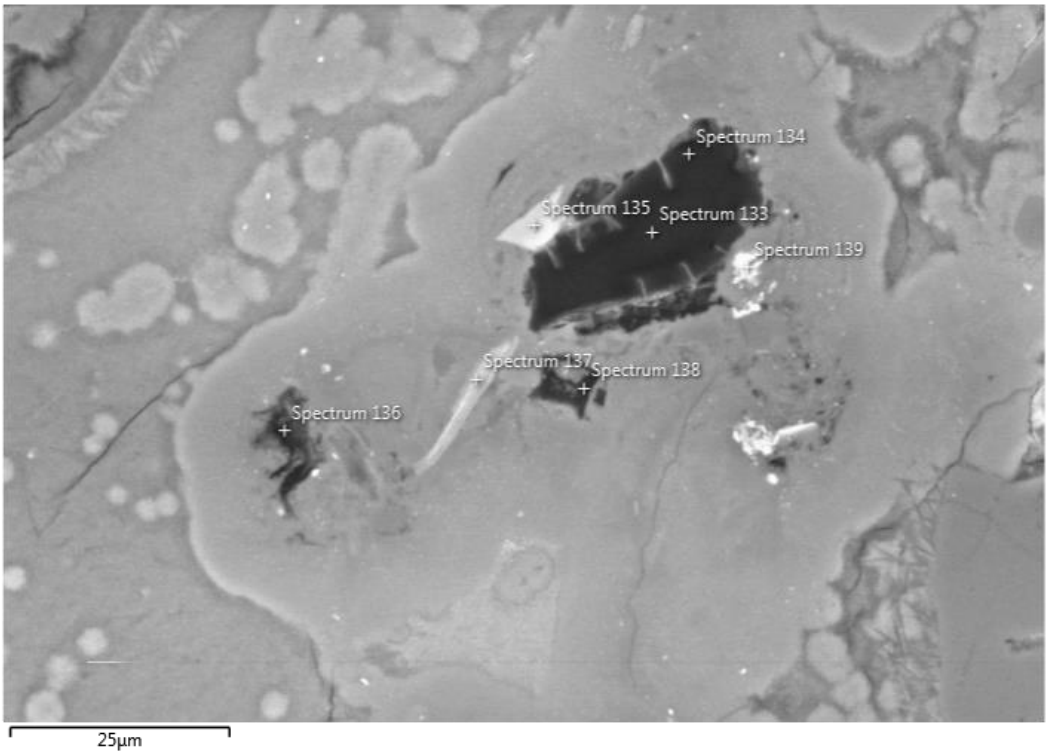
B6. HW19-02a

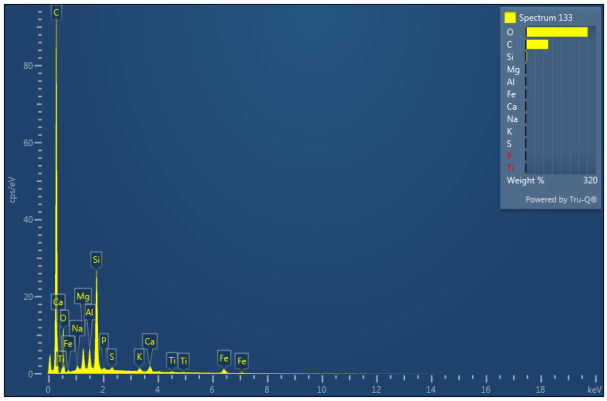

Spectrum 405
Spectrum 400
Spectrum 406
Spectrum 397
Spectrum 399
Spectrum 401
Spectrum 402
Spectrum 404
Spectrum 403
100µm

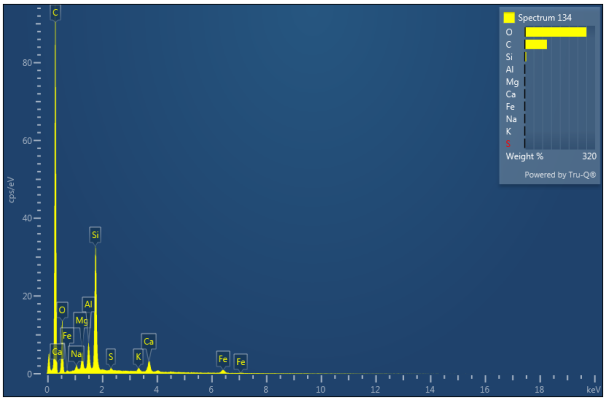

Spectrum 399
O
Si
Fe
C
Mg
Al
Ca
Na
K
Ti
Weight %
60
cps/eV
keV

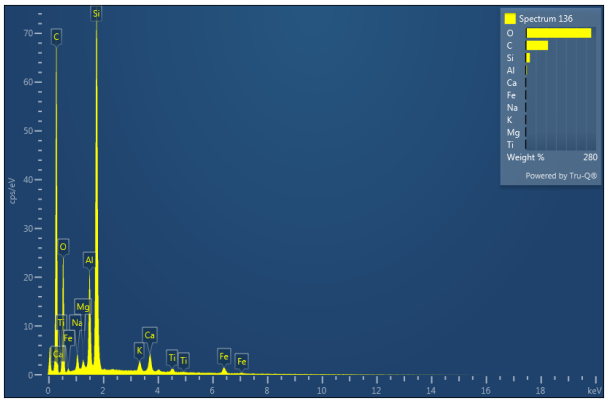

Spectrum 400
O
Si
Fe
Mg
Al
C
Ca
Na
K
Ti
Weight %
50
cps/eV
keV

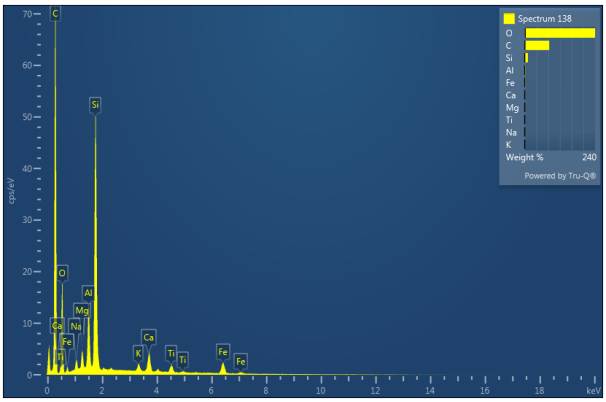
B7. HW19-32a


Spectrum 134
Spectrum 135
Spectrum 133
Spectrum 139
Spectrum 137
Spectrum 138
Spectrum 136
25µm


Spectrum 133
Weight % 320
Powered by Tru-Q®
cps/eV
kev

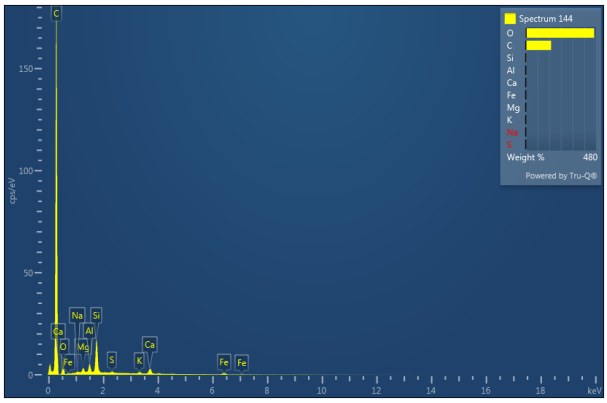

Spectrum 134
Weight % 320
Powered by Tru-Q®
cps/eV
kev

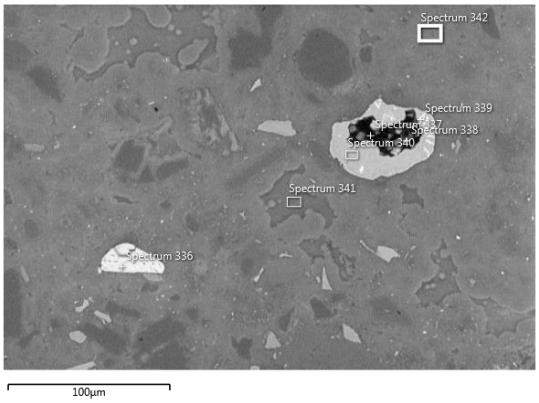

Spectrum 136
Weight % 280
Powered by Tru-Q®
cps/eV
kev

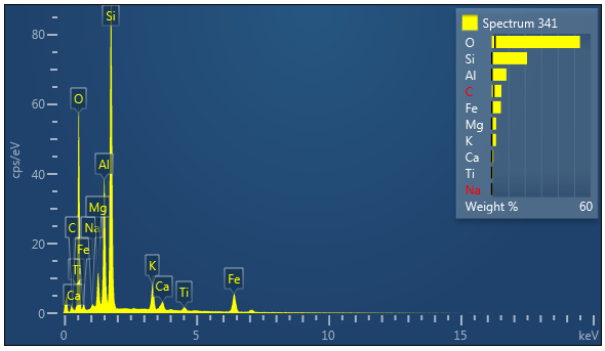

Spectrum 138
Weight % 240
Powered by Tru-Q®
cps/eV
kev

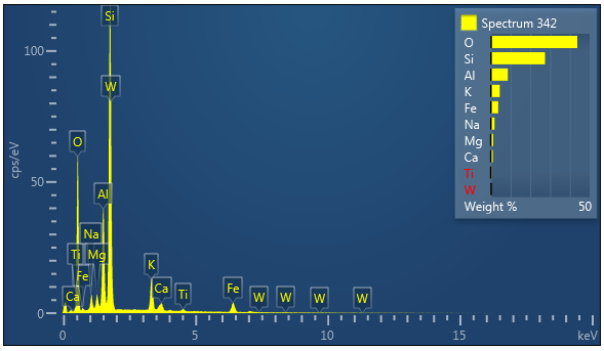
B8. HW19-32a


Spectrum 146
Spectrum 142
Spectrum 145
Spectrum 147
Spectrum 140
Spectrum 141
Spectrum 143
Spectrum 144
100µm

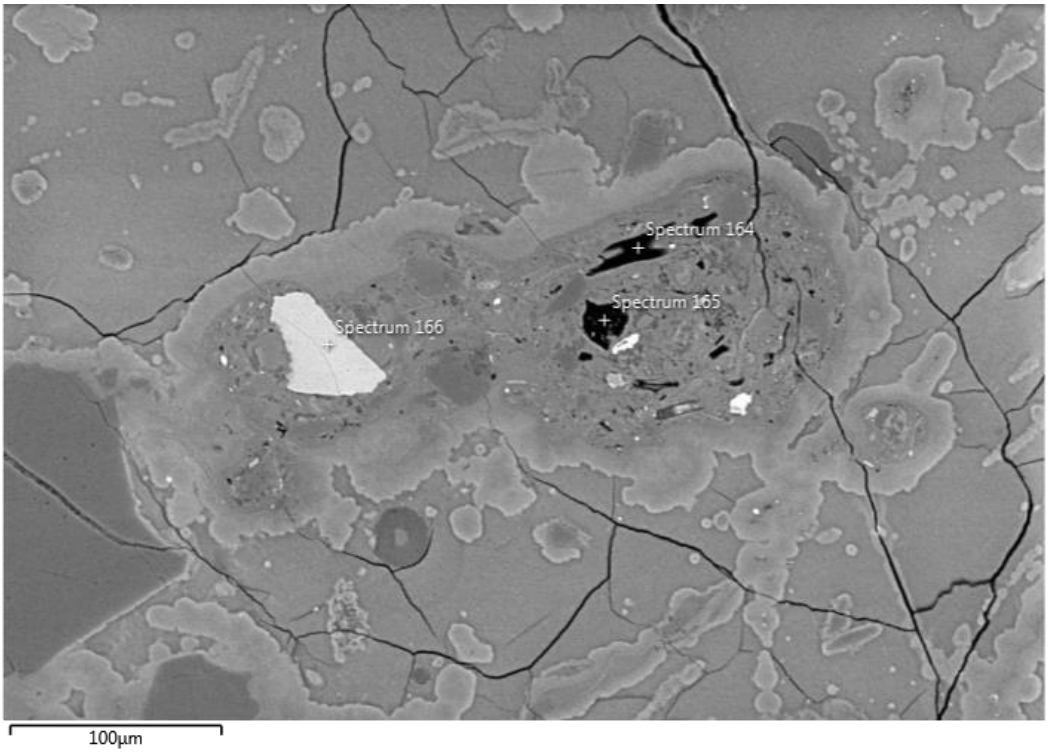

Spectrum 144
Weight %
480
Powered by Tru-Q®
cps/eV
keV

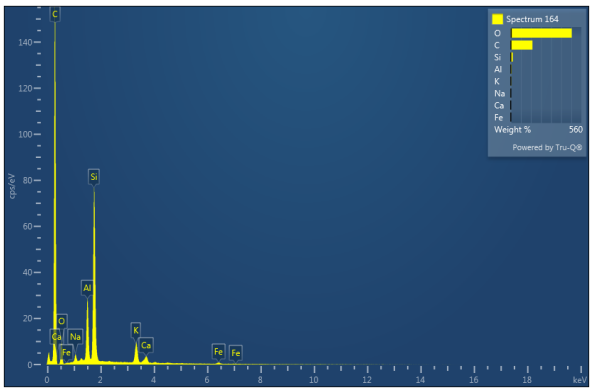

Spectrum 342
Spectrum 339
Spectrum 338
Spectrum 340
Spectrum 341
Spectrum 336
100µm

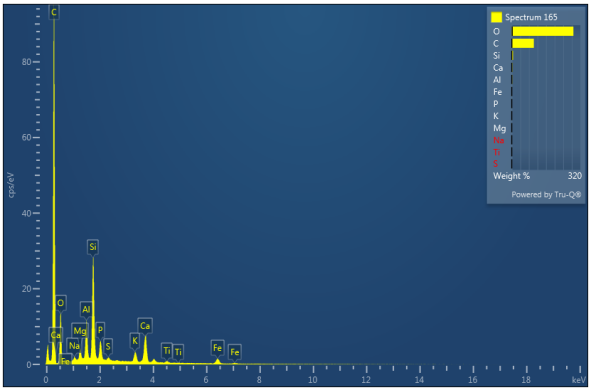

Spectrum 341
O
Si
Al
C
Fe
Mg
K
Ca
Ti
Na
Weight %
60
cps/eV
keV


Spectrum 342
O
Si
Al
K
Fe
Na
Mg
Ca
Ti
W
Weight %
50
cps/eV
keV

B9. HW19-32a


Spectrum 164
Spectrum 165
Spectrum 166
100µm


Spectrum 164
Weight % 560
Powered by Tru-Q®
cps/eV
keV


Spectrum 165
Weight % 320
Powered by Tru-Q®
cps/eV
keV